La investigación reportada en esta tesis es parte de los programas de investigación del CICESE (Centro de Investigación Científica y de Educación Superior de Ensenada, Baja California).
La investigación fue financiada por SECIHTI (Secretaría de Ciencia, Humanidades, Tecnología e Innovación).

Centro de Investigación Científica y de Educación Superior de Ensenada, Baja California

Doctor of Science
in Physical Oceanography

Submesoscale vertical heat flux in the mixed layer

A dissertation

submitted in partial satisfaction of the requirements for the degree

Doctor of Science

By:

Jonathan Aparco Lara

Ensenada, Baja California, Mexico

2025

A Dissertation Presented by

Jonathan Aparco Lara

and approved by the following Committee

Dr. José Gómez Valdés
Thesis co-director

Dr. Héctor Salvador Torres Gutiérrez
Thesis co-director

Dr. Enric Pallàs Sanz

Dr. Julio Sheinbaum Pardo

Dr. Jean Patrice Klein

Dra. María Tereza Cavazos Pérez
Coordinadora del Posgrado en Oceanografía Física

Dra. Ana Denise Re Araujo
Directora de Estudios de Posgrado

Resumen de la tesis que presenta Jonathan Aparco Lara como requisito parcial para la obtención del grado de Doctor en Ciencias en Oceanografía Física.

Submesoscale vertical heat flux in the mixed layer

Resumen aprobado por:

Dr. José Gómez Valdés
Thesis co-director

Dr. Héctor Salvador Torres Gutiérrez
Thesis co-director

Simulaciones numéricas recientes y observaciones con flotadores lagrangianos, derivadores y radares de dispersión Doppler (observación aérea) han mostrado que, en la capa de mezcla, se producen movimientos horizontales del orden de kilómetros y con duraciones de horas a 2-3 días. Estos movimientos, caracterizados por una vorticidad y deformación de orden del parámetro de Coriolis, tienden a romper el balance geostrófico e inducen intensos desplazamientos verticales (aproximadamente 100 m/día). En covarianza con la anomalía de temperatura en un sistema frontal, estos desplazamientos generan flujos verticales ascendentes de calor con frecuencias superiores a un ciclo por día (alta frecuencia). Estos flujos son clave para el balance energético y la redistribución de calor en el océano, regulando la dinámica submesoescalar y modulando indirectamente la interacción entre procesos de mesoescala y turbulentos, impactando por ello la estructura térmica del océano y el clima global. La dinámica submesoescalar es modulada por forzantes atmosféricos, como el intercambio de calor en la interfaz océano-atmósfera y el esfuerzo del viento, los cuales pueden impactar simultáneamente la dinámica submesoescalar en una región oceánica. Esta simultaneidad dificulta la identificación precisa del mecanismo responsable de los flujos de calor de alta frecuencia. En esta tesis, se aborda la hipótesis de que el enfriamiento diurno superficial neto (proceso térmico) y el esfuerzo del viento (proceso mecánico) impactan la dinámica submesoescalar, generando flujos verticales de calor de alta frecuencia. Para probar esta hipótesis, se realizaron simulaciones numéricas bajo condiciones idealizadas para replicar la evolución frontal submesoescalar en un canal periódico, comparando experimentos con y sin forzantes. Los resultados mostraron que, en la evolución libre, los flujos de calor de alta frecuencia alcanzaron un máximo de 1 ciclo cada 10 horas, mientras que, en los experimentos forzados, la inestabilidad baroclínica se intensificó, aumentando el crecimiento de los meandros, promoviendo una mayor transferencia de energía a escalas más pequeñas y reforzando la circulación secundaria del frente. Esto generó una tendencia hacia frecuencias más altas y mayores flujos de calor. Aunque los mecanismos de los forzantes son diferentes, ambos impulsaron frecuencias de hasta un ciclo cada 6 horas. Es importante señalar que los flujos verticales en la submesoescala pueden ser hasta 10 veces mayores que en la mesoescala, lo que subraya su impacto en el balance de calor global. Estos hallazgos ayudan a explicar las altas frecuencias observadas en simulaciones con condiciones más realistas, donde los flujos alcanzan frecuencias cercanas a 1 ciclo por hora.

Palabras clave: Flujos verticales de calor, alta frecuencia, capa de mezcla, inestabilidad baroclínica, submesoescala.

Abstract of the thesis presented by Jonathan Aparco Lara as a partial requirement to obtain the Doctor of Science degree in Physical Oceanography.

Submesoscale vertical heat flux in the mixed layer

Abstract approved by:

PhD José Gómez Valdés
Thesis Co-Director

PhD Héctor Salvador Torres Gutiérrez
Thesis Co-Director

Recent numerical simulations and observations with Lagrangian floats, drifters, and airborne Doppler radar have shown that, in the mixed layer, horizontal movements on the order of kilometers occur, with durations ranging from hours to 2-3 days. These movements, characterized by vorticity and deformation on the order of the Coriolis parameter, tend to disrupt the geostrophic balance and induce strong vertical motions (approximately 100 m/day). In covariance with the temperature anomaly in a frontal system, these motions generate upward heat fluxes with frequencies greater than one cycle per day (high frequency). These fluxes are key to the energy balance and heat redistribution in the ocean, regulating submesoscale dynamics and indirectly modulating the interaction between mesoscale and turbulent processes, impacting the thermal structure of the ocean and global climate. Submesoscale dynamics are influenced by atmospheric forcing, such as heat exchange at the ocean-atmosphere interface and wind stress, which can simultaneously impact submesoscale dynamics in an oceanic region. This simultaneity complicates the precise identification of the mechanism responsible for the high-frequency heat fluxes. In this thesis, the hypothesis is addressed that net diurnal surface cooling (thermal process) and wind stress (mechanical process) impact submesoscale dynamics, generating high-frequency vertical heat fluxes. To test this hypothesis, numerical simulations are performed under idealized conditions to replicate submesoscale frontal evolution in a periodic channel, comparing experiments with and without forcing. The results show that, in the free evolution, high-frequency heat fluxes reached a maximum of one cycle every 10 hours, while in the forced experiments, baroclinic instability intensified, increasing the growth of meanders, promoting greater energy transfer to smaller scales, and reinforcing the secondary circulation of the front. This led to a tendency toward higher frequencies and larger heat fluxes. Although the mechanisms of the forcings are different, both drive frequencies up to one cycle every 6 hours. It is important to note that vertical fluxes in the submesoscale can be up to 10 times greater than those in the mesoscale, highlighting their impact on the global heat balance. These findings help explain the high frequencies observed in simulations with more realistic conditions, where fluxes reach frequencies close to one cycle per hour.

Keywords: Vertical heat fluxes, high frequency, mixed layer, baroclinic instability, submesoscale.

Dedication

To my inner child, the one who first discovered the ocean through photographs, igniting a lifelong curiosity for the unknown. This thesis is dedicated to him, for never ceasing to learn, dream, and marvel at the wonders of the world.

A mi niño interior, aquel que descubrió el océano a través de fotografías, despertando una curiosidad eterna por lo desconocido. Esta tesis está dedicada a él, por nunca dejar de aprender, soñar y maravillarse ante las maravillas del mundo.

Acknowledgments

Este trabajo no habría sido posible sin el apoyo de diversas instituciones y personas. Agradezco profundamente al CICESE y al SECIHTI por el financiamiento proporcionado (CVU: 764766), que permitió llevar a cabo esta investigación. A mis mentores y colaboradores, gracias por su experiencia, guía y dedicación, que fueron fundamentales en mi formación académica y personal. Su apoyo fue esencial para superar los retos de este proyecto.

A mi mentor José, por su constante apoyo académico, su guía y su sabiduría. Gracias por compartir tus conocimientos y experiencia. También quiero expresar mi agradecimiento a su esposa, la señora Christina, por preocuparse por mi bienestar y asegurarse de que mantuviera una buena salud. En ustedes encontré un apoyo familiar invaluable que me acompañó lejos de casa.

A mi mentor Héctor, quien, además de brindarme conocimientos y orientación académica, estuvo presente como un hermano mayor. Agradezco profundamente las discusiones académicas y su dedicación, las cuales fueron clave para mi aprendizaje.

A mis sinodales académicos Julio, Enric y Patrice, por sus valiosos comentarios y recomendaciones, que enriquecieron significativamente el desarrollo de esta tesis. A Julio, por compartir generosamente su conocimiento durante las clases del programa doctoral en el CICESE. A Enric, por las estimulantes conversaciones que profundizaron mi comprensión de temas clave. Y a Patrice, por sus clases en Caltech durante mi estancia en el JPL-NASA, las cuales ampliaron mi visión de la investigación.

A mi mentor en el JPL-NASA, Ian, quien, junto a Héctor y José, me brindó la oportunidad de realizar una estancia académica en el JPL-NASA. Esta experiencia fue fundamental para el desarrollo de esta tesis y enriqueció tanto mi formación profesional como personal.

A mis padres, Teófilo y Sonia, y a mis hermanos, Warner, Kevin y Tony, por su apoyo incondicional y su amor constante, que me dieron la fuerza para seguir adelante. Y a mis amigos del fútbol, quienes, entre jugadas y risas, me ayudaron a liberar el estrés académico y encontrar momentos de distracción en medio del doctorado.

Table of contents

Page

List of figures

Figura Página

Figura Página

Figura Página

Figura Página

Chapter 1. Introduction

This dissertation focuses on vertical heat flux (VHF) induced by submesoscale vertical motion within the ocean's mixed layer. Over the past decade, global realistic numerical simulations with sufficient horizontal resolution to resolve the submesoscale regime have allowed for the estimation of the dominant global contributions of submesoscale VHF (Klein & Lapeyre, 2009). In terms of frequency, submesoscale VHF higher than 1 cycle per day (high frequency) accounts for more than fifty percent of this global estimate (Su et al., 2020). The physical mechanisms that explain this strong high-frequency submesoscale VHF remain unclear, as many atmospheric and oceanic interactions can simultaneously modulate submesoscale dynamics and, consequently, VHF. To address this complexity, we use idealized numerical simulations to generate submesoscale motions modulated by controlled forcing, examining the potential reinforcement of these flows on submesoscale VHF. The atmospheric forcings analyzed here include surface heat flux and wind stress.

1.1 Submesoscale regimen

The submesoscale motions is characterized a by Rossby number (R_o) on the order of $O(1)$. These motions occur within a flow that has weak stratification, typical of the mixed layer, leading to a Richardson number (R_i) also in the order of $O(1)$. The interaction between dynamic and state features in the upper ocean is governed by thermal wind balance, which represents the relationship between vertical shear in geostrophic flow and horizontal density gradients. This balance establishes conditions conducive to the development of baroclinic instability, particularly in areas with intensified horizontal density gradients. As this instability develops, it generates small-scale structures such as fronts, filaments, and coherent vortices (Thomas et al., 2008; McWilliams, 2016; Klein et al., 2019).

Moreover, the high curvature and weak stratification associated with these upper ocean motions allow them to escape geostrophic balance, leading to the emergence of ageostrophic motions. Unlike geostrophic flows, which are governed solely by the balance between pressure gradients and the Coriolis force, ageostrophic motions are driven by local instabilities, external forcing, and nonlinear processes. In the submesoscale regime, baroclinic instabilities and frontal advection can generate intense vertical motions and dynamic features that disrupt the geostrophic balance, resulting in faster currents and complex circulation patterns, such as vortices and filaments (Capet et al., 2008; McWilliams, 2016).

1.2 Modulators of submesoscale motions in the mixed layer

Studies based on numerical modeling that resolve submesoscale dynamics, such as those by Boccaletti et al. (2007) and Sullivan & McWilliams (2018), indicate that the generation, evolution, and decay of submesoscale ageostrophic motions are regulated by mixing production, process parameterized in numerical models. This mixing production in the upper ocean is primarily driven by atmospheric forcing at the surface boundary, which can contribute to frontogenesis (Thomas et al., 2008). Additional, the presence of the large-scale motions, such as mesoscale structures, also contribute to frontogenesis through to deformation field (Hoskins, 1982).

Submesoscale motions are further enhanced by negative heat flux (surface cooling) (Haine & Marshall, 1998) and down-front wind stress (Thomas & Lee, 2005), both of which create unstable fluid conditions in the upper ocean that tends to reduce the stratification in the mixed layer (Thomas et al., 2008).

1.3 Advective vertical heat flux

Using outputs from a numerical model with sufficient horizontal resolution to resolve submesoscale motions (Menemenlis et al., 2021), Figure 1 shows the VHF associated with various dynamic regimes in the frequency-wavenumber domain, including the submesoscale, mesoscale, and inertial-gravitational internal waves. Notably, the VHF within the submesoscale regime dominates with a positive heat flux, making significant contributions to the global heat balance, as reported by Klein et al. (2019) and Su et al. (2018). Specifically, Su et al. (2018) concluded that the VHF in the submesoscale can be up to five times greater than that in the mesoscale.

Furthermore, the submesoscale VHF spans an extended frequency range, encompassing both low-frequency (less than 1/day) and high-frequency (greater than 1/day) components, as illustrated in Figure 1. Su et al. (2020) indicated that the high-frequency component can be up to twice as large as the low-frequency component.

In contrast, the variability of internal waves is limited to mode 10, as shown by the black dashed line in Figure 1. Beyond mode 10, higher modes and high-frequency submesoscale motions coexist both temporally and spatially. This co-occurrence suggests potential interactions between these dynamics that may influence submesoscale motions (Thomas, 2017), introducing the hypothesis that these interactions

could reinforce the high-frequency VHF. However, this hypothesis is not addressed in the current analysis.

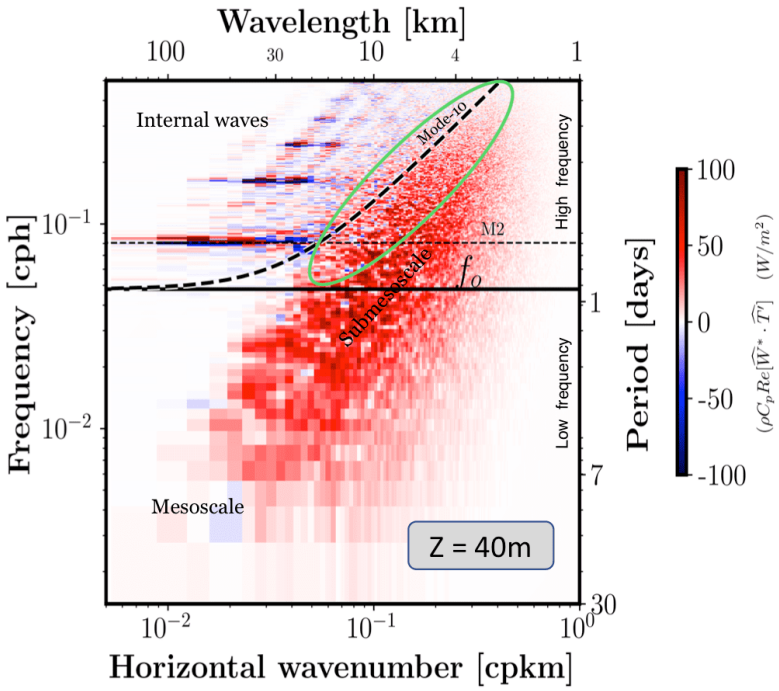

Figure 1. Frequency-wavenumber co-spectrum of vertical heat fluxes over a highly energetic region of the ocean. The spectrum is estimated from hourly outputs of a high-resolution ($1/48°$) realistic simulation using the MITgcm (for more details about the model, refer to Torres et al. (2018)). The spectral space displays multiple dynamic regimes (mesoscale, submesoscale, and different modes of variability of inertia-gravity internal waves limited by mode 10, indicated by the dashed line). The inertial frequency (f_o) and the semidiurnal frequency (M_2) are marked. Vertical fluxes in red (positive values) represent fluxes from the interior of the ocean toward the surface, while fluxes in blue (negative values) represent opposite-direction fluxes. High-frequency and low-frequency submesoscale fluxes are limited by f_o. The region of frequency-wavenumber coexistence between submesoscale (high frequency) and inertia-gravity internal waves (modes beyond mode 10) is indicated by the green circle.

1.4 Research proposal: Submesoscale high-frequency vertical heat flux

This research proposal aims to advance understanding of the high-frequency ($> 1\text{day}^{-1}$) variability of VHF driven by the vertical motions in the mixed layer in the submesoscale regime.

Given that these vertical motions are linked to submesoscale ageostrophic secondary circulations at fronts and convective processes driven by vertical buoyancy instability, both of which can be modulated by atmospheric forcing (i.e., ocean-atmosphere heat flux and wind stress), we propose the following hypothesis: Atmospheric forcing triggers high-frequency VHF through the reinforcement of submesoscale secondary circulation and the intensification of convective motions.

To test this hypothesis, we conducted idealized numerical simulations of a submesoscale front in free evolution, as well as simulations forced by surface heat flux and wind stress. These simulations provide valuable insights into how different atmospheric forcing mechanisms can enhance high-frequency VHF in the upper ocean.

1.5 Comprehensive overview of thesis scope

In Chapter 2, we explore the features of the MITgcm model's numerical setup, which serves as the tool of our study. This chapter presents a detailed examination of the initial conditions employed in our numerical experiments, with a particular focus on the density field characterized by a submesoscale front and the associated jet. These initial conditions provide the necessary framework for understanding the evolution of the system under different forcing mechanisms, which are further explored in the subsequent chapters.

Chapter 3 is dedicated to a comprehensive analysis of the physical parameters used in this study, with special emphasis on understanding their role in the dynamics of the submesoscale front. This chapter highlights the implications of these parameters for VHF, specifically within the context of submesoscale processes. By examining how different parameters govern the system's behavior, we set the stage for understanding their influence on the temporal and spatial evolution of the system under the two main forcing scenarios discussed in the following chapters.

In Chapter 4, we present the development and analysis of a numerical experiment designed to investigate the dynamics of the submesoscale system under the influence of surface cooling. This chapter includes the complete content of a published article (`https://doi.org/10.1029/2023JC020029`). It provides an in-depth description and discussion of the temporal evolution of key parameters, such as the Okubo-Weiss criterion, frontogenesis tendency, and VHF, across two scenarios: free evolution and the influence of surface cooling. The analysis of the VHF co-spectra reveals high-frequency variability in VHF driven by surface cooling. This chapter concludes by summarizing the key findings derived from these analyses.

Chapter 5 presents the development and analysis of another numerical experiment focused on investigating submesoscale system dynamics under wind stress forcing. This chapter provides a detailed examination of both the temporal and spatial evolution of several key parameters, including the Rossby number, frontogenesis tendency, potential vorticity, and VHF, under two distinct scenarios: free evolution

and wind stress forcing. The VHF co-spectra analysis in this chapter reveals high-frequency variability in VHF driven by wind stress. The chapter concludes by synthesizing the main conclusions derived from these analyses.

Finally, Chapter 6 provides a comprehensive conclusion that integrates the findings from both surface cooling and wind stress forcing experiments. This chapter synthesizes the key insights gained from each of the previous chapters, drawing connections between the different forcing mechanisms and their collective impact on submesoscale dynamics and VHF.

Chapter 2. Numerical configuration and initial condition

2.1 Numerical configuration

The Massachusetts Institute of Technology General Circulation Model (MITgcm) was configured to simulate a periodic channel over the X axis with a solid lateral boundary in the Y axis. MITgcm solves the primitive equations of fluid motion, it include: the balance between inertial forces, pressure forces, and viscous forces, the conservation of mass within a fluid. It describes how mass is conserved within a given volume as fluid flows in and out or changes density; the movement of passive tracers (such as temperature, salinity, or chemical constituents) within the fluid. They account for the advection, diffusion, and sources/sinks of these tracers Fox-Kemper et al. (2008).

MITgcm employs numerical methods to discretize these continuous equations into a form suitable for computation on a discrete grid (Figure 2). It then solves these discretized equations iteratively to simulate the evolution of fluid motion and the associated tracers over time.

The reentrant channel has the horizontal resolution of 200 m (Figure 2.a) and a variable vertical resolution, $\sim$ 3.5 m into the mixed layer (ML) and from 4 below ML to 12 m at the bottom (Figure 2.b).

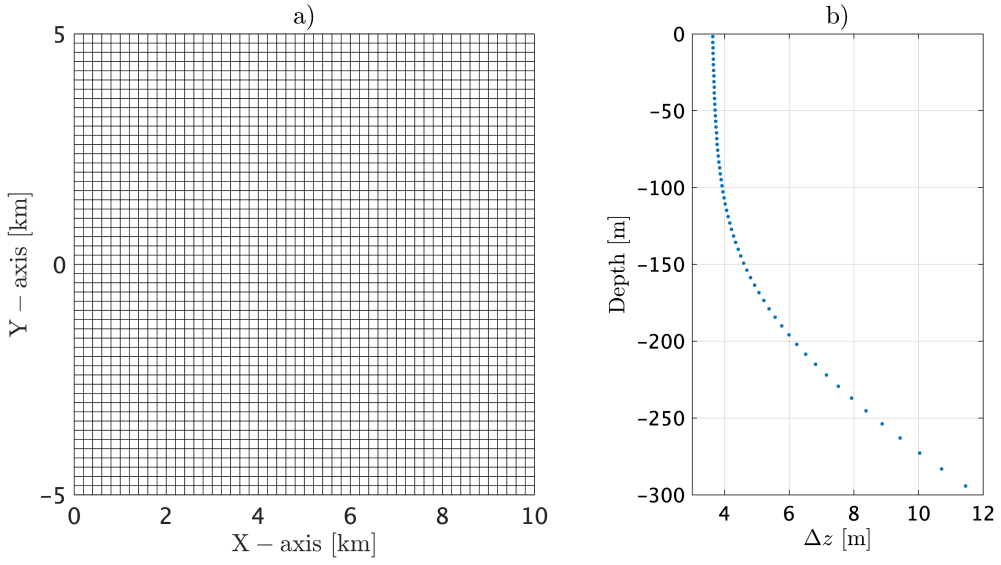

Figure 2. Regular horizontal grid with a resolution of 0.2 x 0.2 km (a). Irregular vertical grid spanning approximately 3 m within the mixed layer and extending from approximately 3 m to 10 m below the mixed layer (b).

The model allows for various parameterizations and boundary conditions to represent complex physical processes, such as radiative transfer, turbulence, mixing, air-sea interactions, and thermodynamics. Its modular design enables researchers to incorporate additional equations or modify existing parameterizations to suit specific research questions or modeling objectives.

2.2 Submesoscale front in Rossby adjustment

An idealized submesoscale front, which is in thermal wind balance within the mixed layer, is used as the initial condition for the numerical experiments. The system is characterized as an unstable, three-dimensional fluid evolving under the influence of thermal wind balance along the front. The Rossby adjustment, which is reached in this configuration, leads to the elimination of the divergent field and the absence of inertial waves in the initial condition (Gill, 2016). Additionally, this adjustment results in the formation of a narrow, high-velocity jet along the front (vertical section in Figure 10.b).

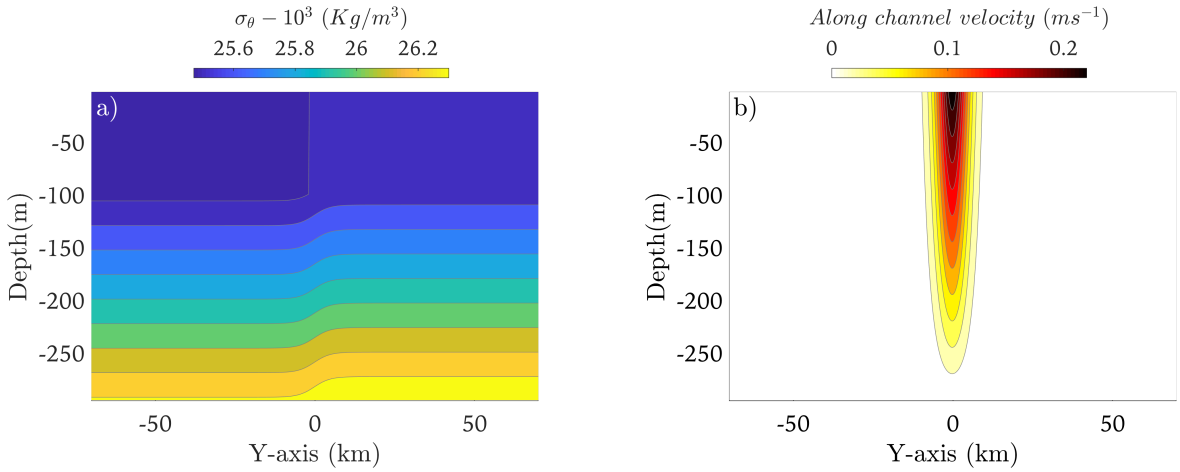

Figure 3. Vertical sections of the density field (a) and the corresponding along-channel velocity (b) for the initial conditions.

The vertical cross-sectional density profile, which includes both depth and cross-channel dimensions (Figure 3.a), was obtained using the buoyancy expression proposed by Fox-Kemper et al. (2008). Details of this mathematical formulation are provided in Section 4.2.1.

Chapter 3. Submesoscale front physics

3.1 Frontogenesis

The mathematical theory of frontogenesis, as detailed by Hoskins (1982), elucidates the rate of change of the buoyancy gradient as it moves with the fluid. It is defined by the frontogenesis function:

$$F_s = \frac{D}{Dt} |\nabla b|^2 , \tag{1}$$

where $\frac{D}{Dt}$ denotes the material derivative, and $b = -\frac{g\rho}{\rho_0}$ represents the buoyancy, with g being the gravitational acceleration, ρ the density and ρ_0 the reference density. This formulation offers a framework to understand the evolution of buoyancy gradients, highlighting the dynamic processes that contribute to the intensification of oceanic fronts.

Considering the total velocity field $\mathbf{u} = (u, v, w)$ and the definition of $\nabla = (\partial_x, \partial_y, \partial_z)$, we express the material derivative as follows:

$$\frac{D}{Dt} = \frac{\partial}{\partial t} + \mathbf{u} \cdot \nabla, \tag{2}$$

as $|\nabla b|^2 = |\nabla b||\nabla b| = \nabla b \cdot \nabla b$, and by applying the product rule for the dot product to the material derivative ($D(\nabla b \cdot \nabla b) = 2\nabla b \cdot D(\nabla b)$), Equation 1 takes the following form:

$$F_s = \frac{D}{Dt} |\nabla b|^2 = 2\nabla b \cdot \left(\frac{D}{Dt} \nabla b \right) = 2 \left(\nabla b \cdot \frac{\partial(\nabla b)}{\partial t} + \nabla b \cdot (\mathbf{u} \cdot \nabla)(\nabla b) \right), \tag{3}$$

where we will call at $\nabla b \cdot \frac{\partial(\nabla b)}{\partial t}$ as local frontogenesis, and at $\nabla b \cdot (\mathbf{u} \cdot \nabla)(\nabla b)$ as advective frontogenesis.

As the ∇ and $\mathbf{u}$ can be separate in horizontal and vertical components, where $\nabla_h = (\partial_x, \partial_y)$ is the horizontal buoyancy gradient, the $\mathbf{u}_h = (u, v)$ is the horizontal current, ∂_z is the vertical buoyancy gradient and w is the vertical velocity. We can separate the local and the advection frontogenesis in horizontal and vertical components.

Horizontal component of the local frontogenesis:

$$\nabla_h b \cdot \frac{\partial(\nabla_h b)}{\partial t}, \tag{4}$$

Vertical component of the local frontogenesis:

$$\partial_z b \cdot \frac{\partial(\partial_z b)}{\partial t}, \tag{5}$$

the advection frontogenesis can be rewrite as follow:

$$\nabla b \cdot (\mathbf{u} \cdot \nabla)(\nabla b) = \nabla b \cdot (\nabla(\mathbf{u} \cdot \nabla b)) - \nabla b \cdot ((\nabla \mathbf{u}) \cdot (\nabla b)), \tag{6}$$

then,

Horizontal component of the advection frontogenesis:

$$\nabla_h b \cdot (\mathbf{u}_h \cdot \nabla_h)(\nabla_h b) = \nabla_h b \cdot (\nabla_h(\mathbf{u}_h \cdot \nabla_h b)) - \nabla_h b \cdot ((\nabla_h \mathbf{u}_h) \cdot (\nabla_h b)). \tag{7}$$

Vertical component of the advection frontogenesis:

$$\partial_z b \cdot (w\partial_z)(\partial_z b) = \partial_z b \cdot (\partial_z(w\partial_z b)) - \partial_z b \cdot ((\partial_z w) \cdot (\partial_z b)). \tag{8}$$

From the equations 4 and 7, the horizontal frontogenesis (F_s^h) take the form:

$$F_s^h = 2(\nabla_h b \cdot \frac{\partial(\nabla_h b)}{\partial t} + \nabla_h b \cdot (\nabla_h(\mathbf{u}_h \cdot \nabla_h b)) - \nabla_h b \cdot ((\nabla_h \mathbf{u}_h) \cdot (\nabla_h b))), \tag{9}$$

from the equations 5 and 8, the vertical frontogenesis (F_s^v) take the form:

$$F_s^v = 2(\partial_z b \cdot \frac{\partial(\partial_z b)}{\partial t} + \partial_z b \cdot (\partial_z(w\partial_z b)) - \partial_z b \cdot ((\partial_z w) \cdot (\partial_z b))), \tag{10}$$

where $F_s = F_s^h + F_s^v$.

3.1.1 Physical interpretation

The sign of the scalar value of F_s indicates a crucial feature in the flow. A positive value corresponds to frontogenesis, which is the convergence of the isolines of buoyancy, while a negative value corresponds to frontolysis, which is the divergence of the isolines of buoyancy. Another interpretation is that positive values indicate stratification, whereas negative values indicate mixing.

Hoskins (1982) presents an interpretation of the horizontal component of the frontogenesis function (F_s^h) under conditions where the horizontal current is non-divergent and the flow is primarily in geostrophic balance ($R_o \ll 1$). Under these conditions, the local term contribution becomes negligible, and $\mathbf{u}_h \cdot \nabla_h b$ tends to zero due to the nearly orthogonal arrangement between the current and the buoyancy gradients. Hence, the (F_s^h) is driven solely by second term of the advection frontogenesis, where : $-\nabla_h \mathbf{u}_h \cdot \nabla_h b$ is the $\mathbf{Q} - vector$ defined by Hoskins (1982).

$$F_s^h = 2\nabla_h b \cdot \mathbf{Q}. \tag{11}$$

This expression can be rewritten in terms of the divergence (δ), Stretching (α), and shearing (γ) deformation, defined as follows:

Divergence is a measure of the rate of change of the flux density of a fluid element. In a multidimensional flow, divergence can indicate areas where water is converging (flowing towards a point) or diverging (flowing outward from a point). In unidirectional flows (1D), divergence or convergence occurs when the flow accelerates or decelerates, leading to changes in the flux density, even without outward or inward movement relative to a point.

$$\delta = \frac{\partial u}{\partial x} + \frac{\partial v}{\partial y}. \tag{12}$$

Stretching deformation describes how a portion of water stretches or compresses along the principal axes. In the oceanic context, this deformation influences the distribution of water masses and the mixing of properties such as temperature and salinity.

$$\alpha = \frac{\partial u}{\partial x} - \frac{\partial v}{\partial y}. \tag{13}$$

Shearing deformation describes how a portion of water undergoes deformation in perpendicular directions along the principal axes. In the ocean, this type of deformation plays a key role in the formation of mesoscale and submesoscale structures such as fronts and eddies.

$$\gamma = \frac{\partial u}{\partial y} + \frac{\partial v}{\partial x}. \tag{14}$$

The $\mathbf{Q} - vector$ is the minus of the product of the velocity gradient tensor ($\nabla_h \mathbf{u_h}$) and the buoyancy gradients ($\nabla_h b$):

$$\mathbf{Q} = -(\nabla_h \mathbf{u_h}) \cdot (\nabla_h b) = - \begin{pmatrix} \frac{\partial u}{\partial x} & \frac{\partial v}{\partial x} \\ \frac{\partial u}{\partial y} & \frac{\partial v}{\partial y} \end{pmatrix} \cdot \begin{pmatrix} \frac{\partial b}{\partial x} \\ \frac{\partial b}{\partial y} \end{pmatrix}, \tag{15}$$

$$\mathbf{Q} = - \left((\frac{\partial u}{\partial x}\frac{\partial b}{\partial x} + \frac{\partial v}{\partial x}\frac{\partial b}{\partial y}), (\frac{\partial u}{\partial y}\frac{\partial b}{\partial x} + \frac{\partial v}{\partial y}\frac{\partial b}{\partial y}) \right), \tag{16}$$

then

$$F_s^h = -2(\frac{\partial b}{\partial x}, \frac{\partial b}{\partial y}) \cdot \left((\frac{\partial u}{\partial x}\frac{\partial b}{\partial x} + \frac{\partial v}{\partial x}\frac{\partial b}{\partial y}), (\frac{\partial u}{\partial y}\frac{\partial b}{\partial x} + \frac{\partial v}{\partial y}\frac{\partial b}{\partial y}) \right), \tag{17}$$

operating and conveniently factoring the terms, we get:

$$F_s^h = -2 \left(\left(\frac{\partial b}{\partial x} \right)^2 \frac{\partial u}{\partial x} + \left(\frac{\partial b}{\partial y} \right)^2 \frac{\partial v}{\partial y} + \frac{\partial b}{\partial x}\frac{\partial b}{\partial y} \left(\frac{\partial u}{\partial y} + \frac{\partial v}{\partial x} \right) \right). \tag{18}$$

Combining the definitions of divergence (equation 12) and normal strain (equation 13), we have:

$$\frac{\partial \mathrm{u}}{\partial \mathrm{x}} = \frac{\delta + \alpha}{2}, \tag{19}$$

$$\frac{\partial \mathrm{v}}{\partial \mathrm{y}} = \frac{\delta - \alpha}{2}. \tag{20}$$

Replacing these, and the definition of the tangential strain (equation 14) into equation 18, we obtain:

$$F_s^h = -2\left(\frac{\delta}{2}\left(\left(\frac{\partial b}{\partial x}\right)^2 + \left(\frac{\partial b}{\partial y}\right)^2\right) + \frac{\alpha}{2}\left(\left(\frac{\partial b}{\partial x}\right)^2 - \left(\frac{\partial b}{\partial y}\right)^2\right) + \gamma\frac{\partial b}{\partial x}\frac{\partial b}{\partial y}\right). \tag{21}$$

This shows that the advection part of frontogenesis is related to divergence (a proxy for vertical movements) and the deformation field (which describes the interaction between structures that stretch or compress the flow).

Continuing with the conditions outlined by Hoskins (1982) as an example of large-scale flow helps to better understand the mechanics of frontogenesis illustrated in Hoskins (1982) and Siegelman et al. (2020). The horizontal velocity field is given by $u = -\alpha x$ and $v = \alpha y$, which implies that the contributions driven by divergence and shear deformation (also known as tangential strain) are zero.

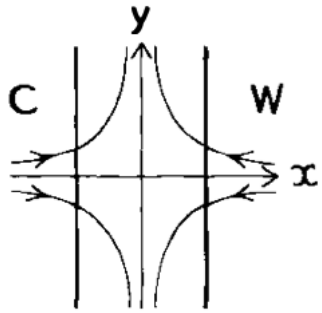

Figure 4. Mechanism of frontogenesis along the x-axis driven by normal strain. The streamlines correspond to the velocity field $(u = -\alpha x, v = \alpha y)$, as described in Hoskins (1982). **C** indicates cold (heavy buoyancy contour) fluid and **W** indicates warm (light buoyancy contour) fluid.

Figure 4 illustrates the mechanisms responsible for generating horizontal gradients in buoyancy within a thermal front along the y-axis, as outlined by Hoskins (1982). The streamlines corresponding to the velocity field compress the buoyancy gradient along the x-axis. According to this model, frontogenesis is primarily driven by normal strain, which is a reasonable approximation for ocean dynamics governed by mesoscale structures.

Figure 5 shows a simplified scheme, similar to Figure 4 but focuses on the convergence of tracers, that shows the dynamic parameters associated with developing the submesoscale front (Siegelman et al., 2020). The strain field (S) that elongates and compresses any tracer along the front is driven by the presence of cyclonic (C) and anticyclonic structures (A) that interact with the front (Figure 5.a). Although the scheme was thought to be in the mesoscale eddies field, this scheme can be applied to submesoscale eddies or any small structures with C and A structures.

However, in the presence of submesoscale processes, the assumption of non-divergence breaks down. Contrary to mesoscale structures, submesoscale features exhibit faster evolution due to their inherent characteristics. This distinction complicates the understanding of frontogenesis, as it introduces variability driven by multiple factors (see equation 21). These factors challenge our comprehension of the mechanisms underlying the formation of strong buoyancy gradients in the ocean.

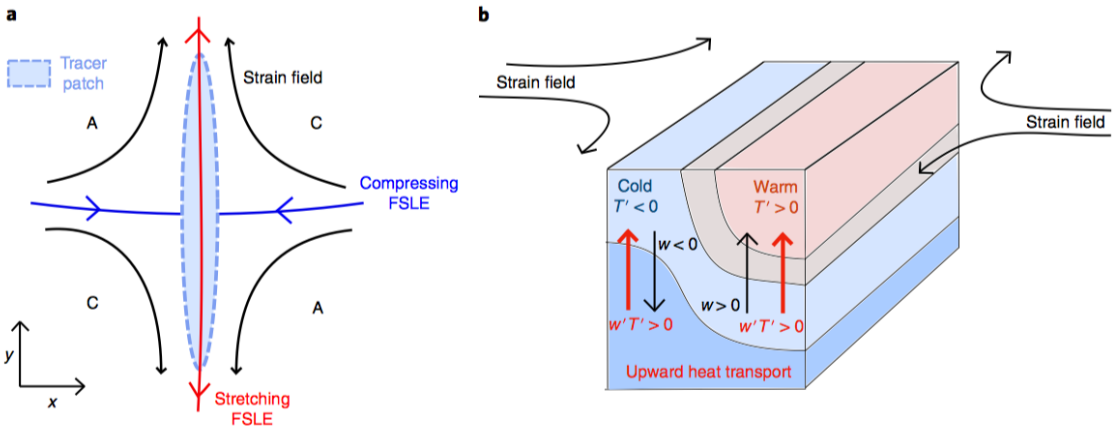

Figure 5. Strain field, frontogenesis, and vertical heat transport. a) A horizontal slice (x, y) of a tracer patch (light blue) in a strain field (black arrows). The strain elongates (compresses) the tracer in the y (x) direction. Red and blue Finite-Size Lyapunov Exponent (FSLE), proxy of strain, arrows identify horizontal stretching and compressing directions. The fronts are aligned with the stretching FSLE. b) A 3D slice of the strain-induced submesoscale front. The thin black lines are isotherms. Vertical velocities (w, straight black arrows) develop in response to the front intensification. The temperature and w anomalies are positively correlated, so frontogenesis-induced vertical heat transport is upward. Figure from Siegelman et al. (2020).

3.2 Ageostrophic secondary circulation

The vertical ageostrophic secondary circulation in the submesoscale front during frontogenesis is illustrated in Figure 5.b. This circulation is characterized by upward motion in positive temperature anomalies and downward motion in negative temperature anomalies. The covariance between this vertical velocity and the temperature anomalies results in an overall upward heat transport. As indicated by Thomas et al. (2008), the semi-geostrophic (SG) theory accurately describes submesoscale dynamics, particularly in relatively straight flows like fronts. This theory offers straightforward insight into the intense fronts and vertical circulations typical of submesoscale features.

Figure 6 illustrates the solution of the SG theory for a collapsed submesoscale front presented by Thomas et al. (2008). The vertical section in Figure 6.c shows the ageostrophic secondary circulation in frontogenetical conditions. The corresponding near-surface vertical velocity is depicted in Figure 6.a, and the

zonal velocity, which relates to the zonal jet as a consequence of the thermal wind balance, is shown in Figure 6.b. The vertical velocity is upward over the less dense part and downward over the denser part, similar to the schematic in Figure 5.b. The frontogenesis section correlates with the maximum zonal jet and the intense downward vertical velocity.

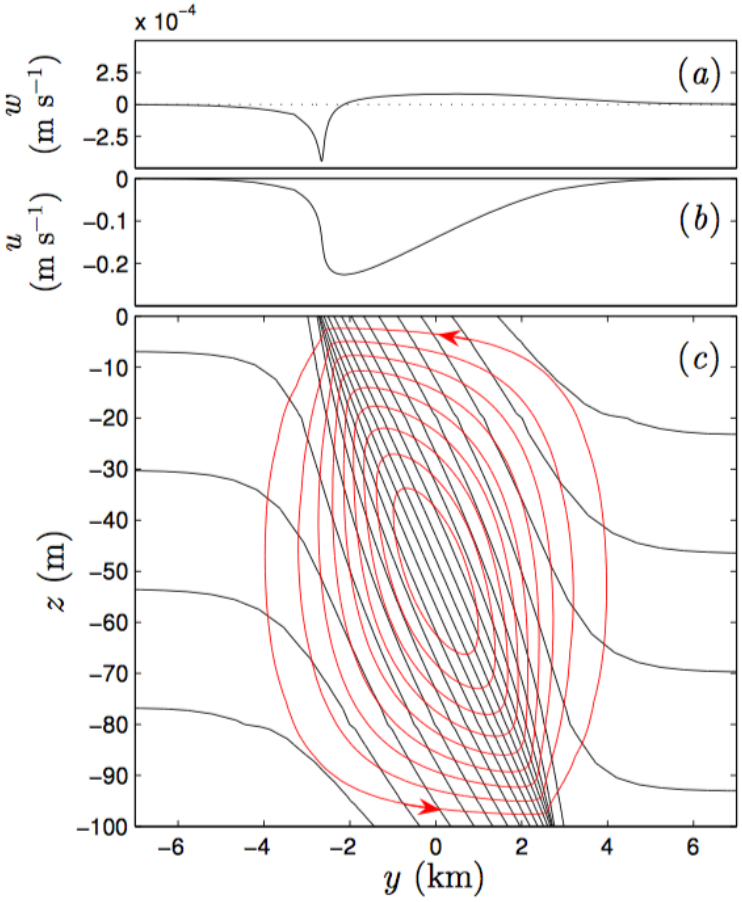

Figure 6. For an initial buoyancy field $B = \frac{\Delta b}{2} \tanh\left(\frac{y}{L}\right)$: (a) Vertical velocity w (red contours) and buoyancy b (black contours) at $t = 1.5$ inertial periods, showing frontal collapse. (b) Horizontal velocity u at $z = -2.5$ m. (c) Overturning streamfunction (red contours) and buoyancy b (black contours) at $t = 1.5$ inertial periods when frontal collapse at the boundaries is about to occur. Figure from Thomas et al. (2008).

To understand the ageostrophic secondary circulation in the submesoscale front, we need to disentangle mathematics approximations that the SG takes into account. For this, we consider a fluid in the ocean, where the velocity field has two terms: $\mathbf{u_g}$ (geostrophic velocity) and $\mathbf{u_{ag}}$ (ageostrophic velocity).

$$\mathbf{u} = \mathbf{u_g} + \mathbf{u_{ag}} \tag{22}$$

The separate of the velocity field can be understand across the Rossby number (Ro), which is defined as:

$$Ro = \frac{U}{fL}, \tag{23}$$

where U is the characteristic velocity of the flow, and L is the characteristic length scale.

In a geostrophic flow, the Rossby number ($Ro \ll 1$) is small, indicating that the Coriolis acceleration is balanced by the pressure gradient. However, when Ro is not small, ageostrophic contributions become significant and play a critical role in the dynamics, especially in the submesoscale regime ($Ro \sim 1$) (Thomas et al., 2008; Klein et al., 2011; McWilliams, 2016).

To analyze this behavior, the total velocity ($\mathbf{u}$) can be expressed as an asymptotic expansion in powers of the Rossby number (Ro):

$$\mathbf{u} = \mathbf{u_g} + Ro\mathbf{u_{ag_1}} + Ro^2\mathbf{u_{ag_2}} + \ldots, \tag{24}$$

where $\mathbf{u_{ag_1}}, \mathbf{u_{ag_2}}, \ldots$ represent the first-order and second-order ageostrophic corrections, respectively.

When the dynamic regimen is controlled by motion with $Ro \ll 1$, the dominant term is $\mathbf{u_g}$, which satisfies the geostrophic approximation, where the Coriolis acceleration ($f\mathbf{k} \times \mathbf{u_g}$) is balanced by the pressure gradient(∇p):

$$f\mathbf{k} \times \mathbf{u_g} = -\frac{1}{\rho_0}\nabla p, \tag{25}$$

where $\mathbf{k}$ is vertical unit vector. The ageostrophic terms ($\mathbf{u_{ag_1}}, \mathbf{u_{ag_2}}$) are negligible, and the dynamics are primarily determined by $\mathbf{u_g}$, which aligns with the isobars.

When the dynamic regimen is controlled by motion with $Ro \sim 1$, the ageostrophic terms ($\mathbf{u_{ag}}$) can no longer be neglected, where only the first ageostrophic correction in the asymptotic expansion is permitted due to it only has a physical interpretation, it is a mathematical restriction of the asymptotic expansion for $Ro \sim 1$. Substituting this asymptotic expansion into the equations of motion and balancing terms of equal order in Ro, we obtain that zeroth order (Ro^0) represent the geostrophic flow, and the first order (Ro^1) represent the first ageostrophic corrections ($\mathbf{u_{ag_1}}$).

then we obtain:

$$\mathbf{u} \approx Ro^0 \mathbf{u_g} + Ro^1 \mathbf{u_{ag_1}}. \tag{26}$$

This approach allows us to analyze the contribution of the ageostrophic components of the velocity as a function of the Rossby number, providing a better understanding of the dynamics of ocean flows, especially in situations where the geostrophic approximation is not sufficient, such as in the submesoscale regimen.

If we take similar conditions as in Thomas et al. (2008) for the velocity field, the velocity vector $\mathbf{u} = (u, v, w)$, where u, v, and w represent the zonal, meridional, and vertical velocities, respectively, can be decomposed into its geostrophic and ageostrophic parts. Assuming the geostrophic meridional velocity v_g is zero and only the zonal geostrophic velocity u_g exists, corresponding to the zonal jet, we have:

$$\mathbf{u} = \mathbf{u_g} + \mathbf{u_{ag}} = (u_g + u_{ag}, v_{ag}, w_{ag}), \tag{27}$$

where: $\mathbf{u_g} = (u_g, 0, 0)$ is the geostrophic velocity and $\mathbf{u_{ag}} = (u_{ag}, v_{ag}, w_{ag})$ is the ageostrophic velocity when $Ro \approx 1$.

The material derivative of a scalar quantity C, which can be a dynamic variable ($\mathbf{u}$) or a tracer, is given by:

$$\frac{DC}{Dt} = \frac{\partial C}{\partial t} + \mathbf{u} \cdot \nabla C, \tag{28}$$

substituting $\mathbf{u}$ with its geostrophic and ageostrophic components, we get:

$$\frac{DC}{Dt} = \frac{\partial C}{\partial t} + \left((u_g + u_{ag}) \frac{\partial C}{\partial x} + v_{ag} \frac{\partial C}{\partial y} + w_{ag} \frac{\partial C}{\partial z} \right). \tag{29}$$

The meridional (v_{ag}) and vertical (w_{ag}) components of the ageostrophic velocity represent the ageostrophic secondary circulation, as indicated by the red contours in Figure 6.c. This vertical circulation advects tracers, connecting the surface ocean with the interior. This mechanism is critical in transporting heat, nutrients, and other properties, influencing various oceanic processes and contributing to the vertical

exchange in submesoscale dynamics (Klein et al., 2019).

3.3 Okubo-Weiss parameter

The Okubo-Weiss parameter is defined as:

$$OW = \alpha^2 + \gamma^2 - \zeta^2, \tag{30}$$

,

where α and γ represent the stretching and shearing deformations, as previously defined, and ζ denotes the relative vorticity, given by

$$\zeta = \frac{\partial v}{\partial x} - \frac{\partial u}{\partial y}. \tag{31}$$

The sign of the OW parameters indicates whether the flow is strain-dominated ($OW > 0$, such as in frontogenetical regions), vorticity-dominated ($OW < 0$, inside coherent vortices), or neutral with respect to strain and vorticity ($OW \approx 0$).

The interpretation of OW offers valuable insights into the interactions between structures within the flow. The OW criterion is particularly useful for understanding two-dimensional turbulence. To examine the connection between OW and advective acceleration, we begin with the two-dimensional momentum equation.

$$\frac{\partial u}{\partial t} + u\frac{\partial u}{\partial x} + v\frac{\partial u}{\partial y} - (f_0 + \beta y)v = -\frac{1}{\rho_o}\frac{\partial p}{\partial x} + \nu\left(\frac{\partial^2 u}{\partial x^2} + \frac{\partial^2 u}{\partial y^2}\right), \tag{32}$$

$$\frac{\partial v}{\partial t} + u\frac{\partial v}{\partial x} + v\frac{\partial v}{\partial y} + (f_0 + \beta y)u = -\frac{1}{\rho_o}\frac{\partial p}{\partial y} + \nu\left(\frac{\partial^2 v}{\partial x^2} + \frac{\partial^2 v}{\partial y^2}\right), \tag{33}$$

where u and v denote the zonal and meridional velocity components, respectively, f_0 represents the Coriolis frequency at a given latitude, $\beta = \frac{\partial f}{\partial y}$ is the meridional gradient of the Coriolis frequency, ρ_0 is the reference density, p denotes the pressure, and ν is the kinematic viscosity.

Using the velocity vector $\mathbf{u} = (u, v)$, we rewrite the two-dimensional momentum equation in vector form as:

$$\frac{\partial \mathbf{u}}{\partial t} + \mathbf{u} \cdot \nabla \mathbf{u} + (f_0 + \beta y)\mathbf{k} \times \mathbf{u} = -\frac{1}{\rho_0}\nabla p + \text{dissipation}. \tag{34}$$

A stream function for the velocity field is defined in the two-dimensional flow as ψ, such that $u = -\psi_y$ and $v = \psi_x$. Additionally, the pressure can be expressed as: $\widetilde{p} = \frac{p}{\rho_o} - (f_o + \beta y)\psi$, where $\widetilde{p}$ is the ageostrophic component of the pressure. Such that:

$$\nabla \widetilde{p} = \left(\frac{1}{\rho_o}\frac{\partial p}{\partial x} - (f_o + \beta y)\psi_x, \frac{1}{\rho_o}\frac{\partial p}{\partial y} - (f_o + \beta y)\psi_y - \beta\psi \right). \tag{35}$$

This expression can be rewritten as:

$$-(\nabla \widetilde{p} + \beta\psi \mathbf{j}) = -\left(\frac{1}{\rho_o}\nabla p + (f_o + \beta y)\mathbf{k} \times (-\psi_y, \psi_x) \right), \tag{36}$$

replacing this in equation 34 we have:

$$\frac{\partial \mathbf{u}}{\partial t} + \mathbf{u} \cdot \nabla \mathbf{u} = -\frac{1}{\rho_0}\nabla \widetilde{p} - \beta\psi \mathbf{j} + \text{dissipation}, \tag{37}$$

applying the operator ∇ to this equation, assuming the system is conservative in mechanical energy (i.e., the dissipation term is negligible), and considering that in submesoscale dynamics the spatial scales of motion are much smaller than those associated with the β-effect, the expression becomes:

$$\frac{\partial \nabla \cdot \mathbf{u}}{\partial t} + \nabla \cdot (\mathbf{u} \cdot \nabla \mathbf{u}) = -\frac{1}{\rho_0}\nabla^2 \widetilde{p}, \tag{38}$$

where $\nabla \cdot \mathbf{u} = 0$. The divergence of the advective acceleration can be expressed in terms of the ψ:

$$\nabla \cdot ((\mathbf{u} \cdot \nabla)\mathbf{u}) = \frac{1}{2}\left(\left(2\frac{\partial^2 \psi}{\partial x \partial y} \right)^2 - 4\frac{\partial^2 \psi}{\partial x^2}\frac{\partial^2 \psi}{\partial y^2} \right). \tag{39}$$

The quantities α, γ, and ζ, as previously defined, can be also expressed in terms of ψ and substituted

into equation 39:

$$\nabla \cdot ((\mathbf{u} \cdot \nabla)\mathbf{u}) = \frac{1}{2}\left(\overbrace{\left(\underbrace{-2\frac{\partial^2\psi}{\partial \mathrm{x}\partial \mathrm{y}}}_{\alpha}\right)^2 + \left(\underbrace{\frac{\partial^2\psi}{\partial \mathrm{x}^2} - \frac{\partial^2\psi}{\partial \mathrm{y}^2}}_{\gamma}\right)^2}^{\text{Hyperbolic}} - \overbrace{\left(\underbrace{\frac{\partial^2\psi}{\partial \mathrm{x}^2} + \frac{\partial^2\psi}{\partial \mathrm{y}^2}}_{\zeta}\right)^2}^{\text{Elliptic}}}_{\text{Okubo}-\text{Weiss}(OW)}\right). \tag{40}$$

As shown, the equation consists of both hyperbolic and elliptic terms. In the hyperbolic domain ($OW > 0$), the flow is primarily influenced by stretching and shearing deformations. In the elliptic domain ($OW < 0$), relative vorticity dominates the flow. At the transition between the elliptic and hyperbolic domains ($OW = 0$), deformation and vorticity forces are in balance.

The divergence of the advective force (i.e., the Okubo-Weiss parameter), which is a function of deformation and vorticity, tells us how the internal forces drive the evolution of flow dynamics. Equation 38 indicates how the effect of the these internal forces are compensated by $-\frac{1}{\rho_0}\nabla^2\widetilde{p}$, which stems from the geostrophic imbalance. This process is essential for maintaining dynamic equilibrium and plays a key role in the formation and evolution of submesoscale structures, such as eddies and frontal filaments, within the oceanic context.

3.3.1 Interpretation for fluid interaction

The Okubo-Weiss criterion helps to interpret fluid interactions by distinguishing between regions where the flow is dominated by deformation (strain) and regions dominated by rotational motion (vorticity). Here's a detailed interpretation in the context of fluid interaction:

3.3.2 Strain-dominated regions

- **Frontogenesis**: In regions where $OW > 0$, the deformation rate is greater than the vorticity. This indicates that fluid deformation dominates, leading to the stretching and folding of fluid elements. This is typically associated with frontogenesis, where sharp gradients in fluid properties (such as

temperature or density) develop.

- **Instability**: Deformation-dominated regions are often sites of instability and can lead to enhanced mixing and stirring of the fluid. The stretching and folding mechanisms increase the surface area for diffusion, promoting more efficient mixing.
- **Fluid Interaction**: These regions are crucial for the interaction between different fluid masses. For instance, in the ocean, deformation-dominated regions can lead to the mixing of warm and cold water masses, significantly affecting local and global circulation patterns.

3.3.3 Vorticity-dominated regions

- **Eddy Structures**: In regions where $OW < 0$, the vorticity (ζ) is greater than the deformation rate (α and γ). This indicates that the rotational motion of the fluid dominates.
- **Stability**: These vorticity-dominated regions tend to be more stable and can trap fluid particles, forming isolated pockets of fluid that rotate together. This is common in oceanic and atmospheric flows where eddies persist for long periods.
- **Mixing**: Vorticity-dominated regions are less efficient at mixing fluid than deformation-dominated regions. The fluid within these regions tends to circulate within the eddy, maintaining distinct properties (such as temperature, salinity, or pollutant concentration) from the surrounding fluid.

3.3.4 Neutral regions

- **Balance Point**: When OW is close to zero, it suggests a balance between vorticity and deformation. These regions can act as transition zones where the nature of the flow changes from being dominated by rotation to being dominated by strain or vice versa. The line of $OW = 0$ that surrounds an eddy can be used as a proxy of the eddy edge.
- **Dynamic Equilibrium**: Such regions might exhibit complex fluid dynamics where neither rotation nor deformation dominates, leading to intricate flow patterns.

3.4 Potential vorticity

Potential vorticity (q) in a rotating and stratified fluid is a conserved quantity in the absence of dissipation and under adiabatic conditions, defined as:

$$q = \boldsymbol{\omega}_a \cdot \nabla b, \tag{41}$$

where $\boldsymbol{\omega}_a = f\hat{k} + \nabla \times \mathbf{u}$ denotes the absolute vorticity, and ∇b represents the buoyancy gradient. Conservation of q is consistent with the principles of energy and momentum conservation (Gill, 2016; Vallis, 2017), ensuring alignment between rotational dynamics and density gradients within the ocean.

In the ocean, q is influenced by external forcings, such as wind stress and surface cooling, which alter the distribution of relative vorticity and local buoyancy, thereby driving frontogenesis (Thomas et al., 2008). Additionally, baroclinic and symmetric instabilities redistribute vorticity within the mixed layer, leading to variations in q. This redistribution, along with horizontal and vertical transport, modifies the vorticity and local buoyancy balance, influencing the structure of q (Cushman-Roisin & Beckers, 2011).

At submesoscales, localized adjustments between buoyancy and vorticity that often occur near ocean fronts and filaments. These adjustments can reveal regions of enhanced vertical transport, where q anomalies highlight areas of increased vertical heat flux and nutrient exchange. Examining q distributions provides a framework to diagnose the effects of wind forcing, stratification, and instabilities on submesoscale mixing and energy dissipation, offering a comprehensive approach to studying the fine-scale structure of oceanic fronts (McWilliams, 2016).

At submesoscales, localized imbalances between buoyancy and vorticity, typically occurring near ocean fronts and filaments. These imbalances reveal regions of enhanced vertical transport, where q anomalies highlight areas of increased vertical heat flux and nutrient exchange. Examining q distributions offers a framework for diagnosing the effects of wind forcing, stratification, and instabilities on submesoscale mixing and energy dissipation, providing a comprehensive approach to studying the fine-scale structure of oceanic fronts (McWilliams, 2016).

3.5 Vertical heat flux

The vertical heat flux in the ocean is driven by advection and diffusion processes, along with surface heat fluxes such as solar radiation, evaporation, and conduction with the atmosphere. This can be captured through the material derivative of the potential temperature (θ), considering heat diffusion (Alistair et al., 2018):

$$\frac{D\theta}{Dt} = \frac{\partial \theta}{\partial t} + \mathbf{u} \cdot \nabla \theta = k_\theta \nabla^2 \theta + Q_\theta, \tag{42}$$

where k_θ is the thermal diffusivity coefficient, characterizing the rate at which heat is diffused through the fluid, and Q_θ is the heat source or sink term, accounting for processes such as surface cooling, heating from below, or other external influences. Equation 42 represents the balance between the temporal change in temperature, the advection of heat by fluid motion, and the heat diffusion due to temperature gradients. The term $k_\theta \nabla^2 \theta$ describes heat diffusion.

Taking into account that the advective term is expressed as $\mathbf{u} \cdot \nabla \theta = \nabla \cdot (\mathbf{u}\theta) - \theta \nabla \cdot \mathbf{u}$, where θ is decomposed into a mean component ($\overline{\theta}$) and an anomaly (θ_a), and adopting Einstein summation convention with $\mathbf{u} = u_i$ and $\nabla = \partial_i$ (where $i = 1, 2, 3$), the equation 42 is rewritten as:

$$\frac{\partial(\overline{\theta} + \theta_a)}{\partial t} + \frac{\partial(u_i(\overline{\theta} + \theta_a))}{\partial x_i} - (\overline{\theta} + \theta_a)\frac{\partial u_i}{\partial x_i} = -\frac{\partial}{\partial x_i}\left(k_\theta \frac{\partial(\overline{\theta} + \theta_a)}{\partial x_i}\right) + Q_\theta. \tag{43}$$

Assuming incompressibility ($\frac{\partial u_i}{\partial x_i} = 0$), and reorganizing the terms into horizontal ($i = 1, 2$) and vertical components, while multiplying by the heat capacity (C_p) and reference density (ρ_0), we obtain the following expression:

$$C_p\rho_0 \frac{\partial(\overline{\theta} + \theta_a)}{\partial t} = -C_p\rho_0 \frac{\partial(...)}{\partial x_{i=1,2}} - \frac{\partial}{\partial z}\overbrace{C_p\rho_0\left(k_\theta \frac{\partial(\overline{\theta} + \theta_a)}{\partial z} + w(\overline{\theta} + \theta_a)\right)}^{\text{Total vertical heat flux}} + C_p\rho_0 Q_\theta, \tag{44}$$

where w denotes the vertical velocity, the total vertical heat flux is highlighted in Equation 44 (this term arises from both advection and diffusion processes). In the present study, we focus on the advection component, which we refer to as the vertical heat flux (VHF). The expression for the VHF is then given by:

$$\text{VHF} = C_p \rho_0 w\overline{\theta} + C_p \rho_0 w\theta_a, \tag{45}$$

where, on average, only the second term contributes to the net VHF. This is because the average covariance between the vertical velocity (w) and the potential temperature anomaly (θ_a) is non-zero, i.e., $\overline{w\theta_a} \neq 0$. Therefore, we simplify the VHF expression to:

$$\text{VHF} = \rho_0 C_p w\theta_a. \tag{46}$$

Chapter 4. Submesoscale vertical heat flux enhanced by surface cooling

4.1 Introduction

The ocean plays a crucial role in regulating the Earth's climate by storing and transporting heat; the rate of ocean heat uptake is governed by oceanic motions that transport heat vertically from the air-sea interface to the ocean interior (Klein et al., 2019). Studies of submesoscale processes have gained significant attention in recent years due to the key role of these processes in ocean dynamics and their contribution to the VHF (Taylor & Thompson, 2022).

Recent high-performance computational tools have enabled ocean dynamics to be simulated with global coverage and at high spatial resolutions. The highest spatial resolution currently available, $\sim$2 km, resolves the submesoscale regime (Su et al., 2018) involving structures with scales of O (2 km) and timescales spanning from hours to days, and Rossby numbers of O (1) (McWilliams, 2016; Thomas et al., 2008; Klein et al., 2011). The simulations of Menemenlis et al. (2008), also known as LLC4320 (`https://data.nas.nasa.gov/ecco/data.php?dir=/eccodata/llc_4320`), provided the opportunity to quantify the relative contribution of the VHF at either high or low frequencies relative to f (the Coriolis frequency). Su et al. (2018) and Su et al. (2020) found that the relative contribution ratio of the VHFs of the submesoscale and mesoscale regimes during the winter months in each hemisphere ranges on average from 5 to 1. Upward heat transport has been confirmed by observational studies (Siegelman et al., 2019; Yu et al., 2019). In particular, Su et al. (2020) reported that the amplitude of the high-frequency VHF component (greater than 1 day^{-1}) is 2 times larger than that of the low-frequency component (less than 1 day^{-1}), pointing to the need to understand the physical mechanisms that trigger this intense high-frequency variability.

Submesoscale motions within the ML can be affected by air-sea interactions and ocean-scale interactions, such as eddies, filaments, fronts, and internal waves (Taylor & Thompson, 2022). Therefore, these interactions impact the VHF. Idealized numerical simulations focusing on submesoscale processes have shown that the submesoscale activity intensifies when the ocean surface is cooled by the atmosphere, resulting in an increase in vertical motion and a major presence of fine-scale structures (Fox-Kemper et al., 2008; Thomas, 2012). Similarly, the submesoscale activity intensifies when wind acts along submesoscale fronts (Barkan et al., 2017; Thomas et al., 2016). Furthermore, the vertical ageostrophic

circulation associated with submesoscale fronts can be reduced or intensified as it interacts with internal waves (Thomas, 2017). Therefore, the high-frequency VHF variabilities quantified by Su et al. (2020) might be driven or affected by the above mentioned processes. The concurrent presence of these drivers complicates our understanding of the mechanisms behind the high-frequency VHF reported by Su et al. (2020). One approach to addressing this problem is through idealized and controlled numerical simulations.

In this study, we examine the impact of surface cooling on VHFs through idealized numerical simulations, intending to identify the main drivers of the high-frequency VHF component. The manuscript is structured as follows: Section 2 provides a comprehensive overview of the numerical model, the initial conditions of the simulations, and the experiments conducted. Section 3 presents the results and discussion. Finally, our conclusions are summarized in Section 4.

4.2 Numerical model

The MITgcm (Marshall et al., 1997; Alistair et al., 2018) is used to simulate a re-entrant channel with periodic lateral boundary conditions where a baroclinic unstable jet is related to a submesoscale thermal front sustained within the ML. The reentrant channel has a horizontal dimension of 60 km along the channel (x-axis) and 200 km across the channel (y-axis), with periodic lateral boundary conditions, in a plane with a constant f. To simulate the instabilities within the ML, the configuration of Fox-Kemper et al. (2008) is adapted with an isotropic horizontal resolution of 200 m and a vertical resolution of $\sim$5 m. The vertical resolution is increased progressively below the ML, from $\sim$5 m to $\sim$15 m, to reduce the computational time. The reentrant channel has a vertical dimension of 300 m (z-axis). The dynamics of the submesoscale thermal front are solved using the hydrostatic and incompressible primitive equations, with the potential density depending only on the potential temperature (θ).

4.2.1 Initial conditions

The initial configuration of the submesoscale thermal front in the thermal wind balance is presented in Figure 7; in the figure, the associated stratification and velocity profiles are also indicated. The initial stratification is constructed as follows:

$$b = N^2(z + H_0) + \frac{L_f M_f^2}{2} \tanh\left[\frac{2(y - y_0)}{L_f}\right] + b_0, \tag{47}$$

where N^2 is the front-averaged vertical buoyancy gradient ($N^2 = b_z$, where z is the vertical axis). $N^2 = N^2_{ml}$ for $z > -H_0$, and $N^2 = N^2_{int}$ for $z \leq -H_0$. With $N^2_{ml} = (4f)^2$ within the ML and $N^2_{int} = (64f)^2$ below the ML, $H_0 = 100$ m is the ML depth, $L_f = 10$ km is the submesoscale front width, $M_f^2 = -8f^2$ is the front-averaged horizontal buoyancy gradient, y is the cross-channel direction, y_0 is the cross-channel center, $f = 10^{-4}\ s^{-1}$ is the Coriolis parameter, and b_0 is a constant reference buoyancy value. This initial vertical stratification is depicted in Figure 7.d, where the stratification is strong below the ML and weak within the ML.

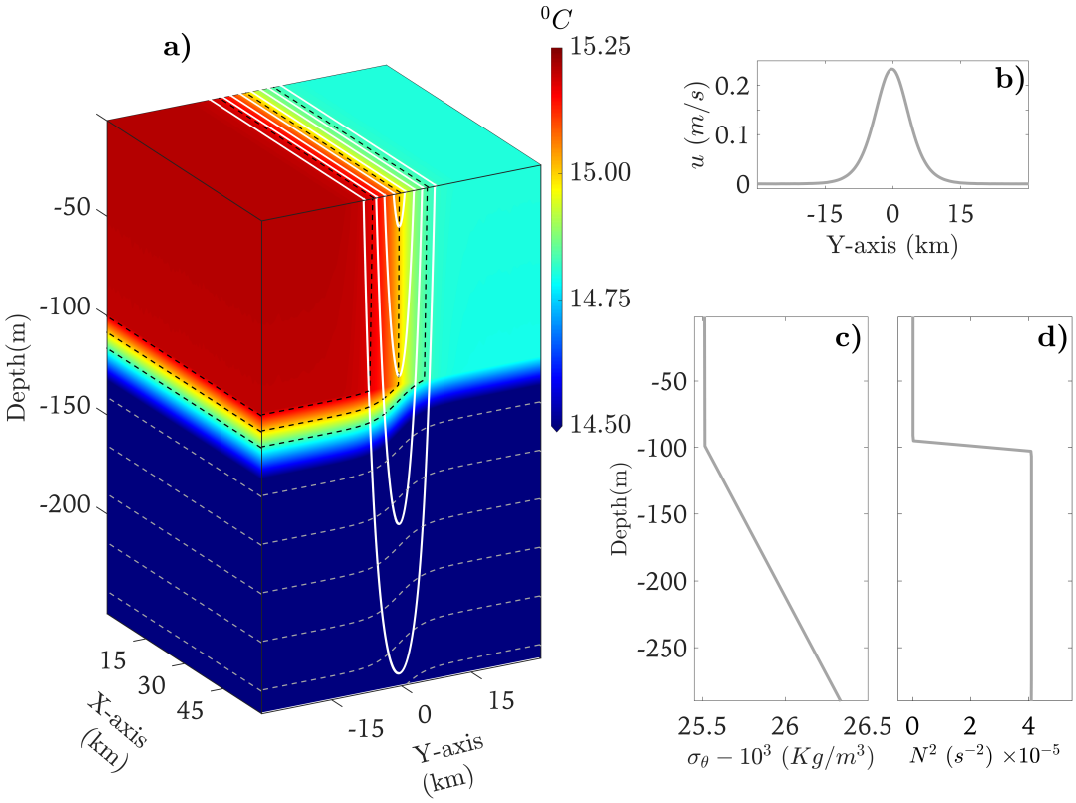

Figure 7. Initial conditions of the submesoscale thermal front in the thermal wind balance. (a) The white contours indicate the along-channel velocity, and the dashed contours indicate the buoyancy. The white contour interval is 0.05 ms^{-1}, the dashed contour interval within the ML is 0.003 ms^{-2}, and the dashed contour interval below the ML is 0.01 ms^{-2}. (b) Initial surface horizontal velocity. (c) Initial vertical profile of density. (d) Buoyancy frequency squared.

Consequently, the fastest-growing length scale (L_s) in our numerical experiment, as determined by linear theory (Eady, 1949; Stone, 1970), is 2.3 km. This scale corresponds to weak stratification in the ML, as indicated by a Richardson number of O(1) ($R_i = 1$ in our case) and an average velocity of 0.04 ms^{-1}.

Furthermore, the critical L_s value when $R_i = 0$ is 1.5 km. Using a horizontal resolution of 200 m, the experiments can capture ML instabilities.

The hydrostatic approximation remains valid in our numerical experiments because $\Gamma = f/N_{ml} = 0.25$ is less than 1 (Thomas et al., 2008). Fox-Kemper et al. (2008) conducted numerical simulations that were similar in setup to that described here, using a nonhydrostatic approach. They found no significant differences when the hydrostatic approximation was used. Vertical mixing was addressed using the nonlocal K-profile parameterization (KPP) turbulent mixing closure scheme (Large et al., 1997).

4.2.2 Numerical experiments

Four numerical experiments are conducted to understand the main drivers of high-frequency VHFs under surface cooling conditions. The first experiment, called the unforced experiment, establishes the free evolution of submesoscale ageostrophic dynamics. The second experiment, called the forced experiment, analyzes the impact of surface cooling on submesoscale ageostrophic dynamics. Two additional experiments, similar to the unforced and forced experiments but without the use of the KPP scheme, were also conducted. In this experiment, atmospheric forcing is represented by a net surface cooling flux with diurnal variability, reaching a maximum of -300 W/m^2 at midnight and zero at noon (Figure 8). This forcing is applied after the second day of free evolution.

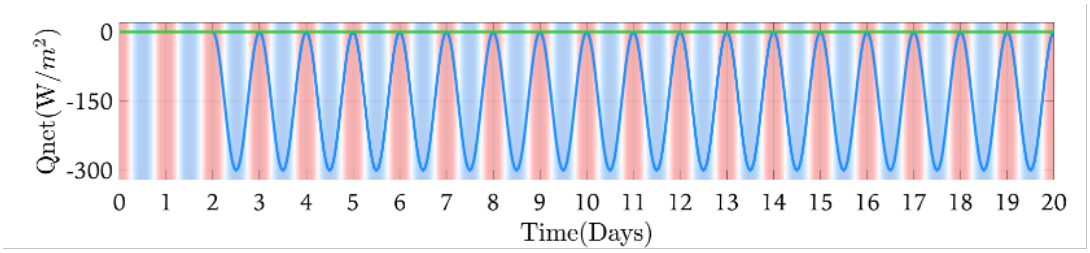

Figure 8. Qnet for the unforced simulation (green line) and the forced simulation (blue line), with the blue and red dashed lines indicating night and day, respectively.

In the simulations, we perturb the front by adding white noise to the density field, thereby activating instabilities within the ML and transferring mechanical energy from available potential energy (APE) to kinetic energy (KE) (Fox-Kemper et al., 2008; Thomas et al., 2008). All experiments, unforced and forced, are run for 20 days.

4.3 Physical parameters

The idealized submesoscale front in thermal wind balance is an unstable system (Figure 7). The KE, δ, S (strain, called also deformation), F_s, and q parameters are significantly impacted when the submesoscale front becomes unbalanced (Mahadevan & Tandon, 2006; Thomas et al., 2008; McWilliams, 2016). This imbalance leads to strong vertical motions that result in an upward VHF within the ML (Su et al., 2018).

The APE contained in the isopycnal slope of the initial front can be converted into KE through the activation of mixed-layer instabilities (Thomas et al., 2008; Mahadevan & Tandon, 2006; Fox-Kemper et al., 2008). The KE is defined as follows:

$$\mathrm{KE} = \frac{1}{2}(u^2 + v^2), \tag{48}$$

where u and v represent the velocity in the x-axis and y-axis directions, respectively. When the front is unbalanced, the KE tends to increase (Fox-Kemper et al., 2008). In the unbalanced submesoscale front, the relative vorticity (ζ), δ and S reach values of O (f) or even larger, as reported in observational studies (Siegelman, 2020; Thompson et al., 2016) and numerical studies (Thomas et al., 2008; Mahadevan & Tandon, 2006). The S is defined as:

$$\mathrm{S} = \sqrt{\sigma_s^2 + \sigma_n^2}, \tag{49}$$

where $\sigma_n = u_x - v_y$ is the normal strain rate (also called stretching deformation) and $\sigma_s = v_x + u_y$ is the shear strain rate (also called shearing deformation). The high δ values result in strong vertical motions, which play a crucial role in submesoscale frontogenesis (Barkan et al., 2019). The high S values drive intense frontogenetic activity (Mahadevan & Tandon, 2006). An additional quantity that is useful for characterizing submesoscale fronts is F_s. This term measures the rate at which fronts are created ($F_s > 0$, frontogenesis) or destroyed ($F_s < 0$, frontolysis):

In a submesoscale front, the presence of a strong gradient of the $\nabla_h b$ can cause the q to take on values with the opposite sign of as the Coriolis parameter (i.e., fq < 0), leading to ML instabilities, as noted in studies by Thomas (2012); Fox-Kemper et al. (2008).

If $fq < 0$, a series of overturning instabilities can occur in the ML. The parameter ϕ_{Ri_B}, defined as $\tan^{-1}\left(-\frac{|\nabla_h b|^2}{f^2 N^2}\right)$, can be used to distinguish among distinct types of instabilities, including gravitational instability (GI), symmetric instability (SI), hybrid instabilities (SI/inertial instability (II)), or stability

(Thomas, 2012). The definitions of these instabilities are provided as follows:

1. GI: if $-180° < \phi_{Ri_B} < -135°$.
2. SI: if $-90° < \phi_{Ri_B} < \phi_c$ when the fluid is cyclonic, and $-90° < \phi_{Ri_B} < -45°$ when the fluid is anticyclonic.
3. SI/Inertial instability (II): if $-45° < \phi_{Ri_B} < \phi_c$, only when the fluid is anticyclonic.
4. GI/SI: if $-135° < \phi_{Ri_B} < -90°$.
5. Stable: if $\phi_c < \phi_{Ri_B}$.

ϕ_c is defined as:

$$\phi_c = \tan^{-1}\left(-\frac{\zeta_g}{f}\right), \tag{50}$$

where $\zeta_g = f + \nabla \times \mathbf{u}_g.\hat{k}$ is the vertical component of the absolute vorticity of the geostrophic flow.

The total VHF is the result of the combination of both the diffusion and the advection processes (Alistair et al., 2018). Here, we focus on the advection component, which is defined as the covariance between the vertical motion (w) and the potential temperature anomaly (θ_a). The advection component of the VHF is defined the equation 46.

4.4 Results and discussion

4.4.1 Temporal variability

Figure 9 illustrates the temporal evolution of the volume-averaged $\overline{\text{KE}}$, $\overline{q}$, $\overline{F_s}$, and $\overline{\text{VHF}}$ parameters for the unforced and forced experiments, as well as the temporal evolution of the root mean square (RMS) of δ/f (δ_{rms}) and S/f (S_{rms}). All volume averages, except that of the KE, were calculated over the dynamically active volume (i.e., KE > 0). The time series cover 20 days of simulation, starting from the initial conditions. The volume average is integrated from a 100-m depth to the surface.

In the unforced case, the $\overline{\text{KE}}$ is constant for the first five days (Figure 9.a). However, after this period, the $\overline{\text{KE}}$ begins to increase, indicating that fine-scale features are enhanced. This positive $\overline{\text{KE}}$ trend suggests that ML instabilities persist throughout the simulation. In the forced case, the $\overline{\text{KE}}$ trend increases more rapidly than in the unforced case, indicating the vigorous production of fine-scale features.

The δ_{rms} and S_{rms} parameters increase after the second day (Figure 9.b and c), indicating a transition of the submesoscale front from a balanced system to an unbalanced system. In the unforced case, δ_{rms} remains quasi-constant at 0.2, suggesting that the vertical motion variabilities reach statistical equilibrium. In contrast, S_{rms} increases throughout the integration of the simulation. This increase is consistent with the positive F_s trend, indicating the sharpening of fronts by the strain field. In the forced case, both δ_{rms} and S_{rms} increase more rapidly than in the unforced case, with significantly higher positive trends, suggesting an enhancement of vertical motions.

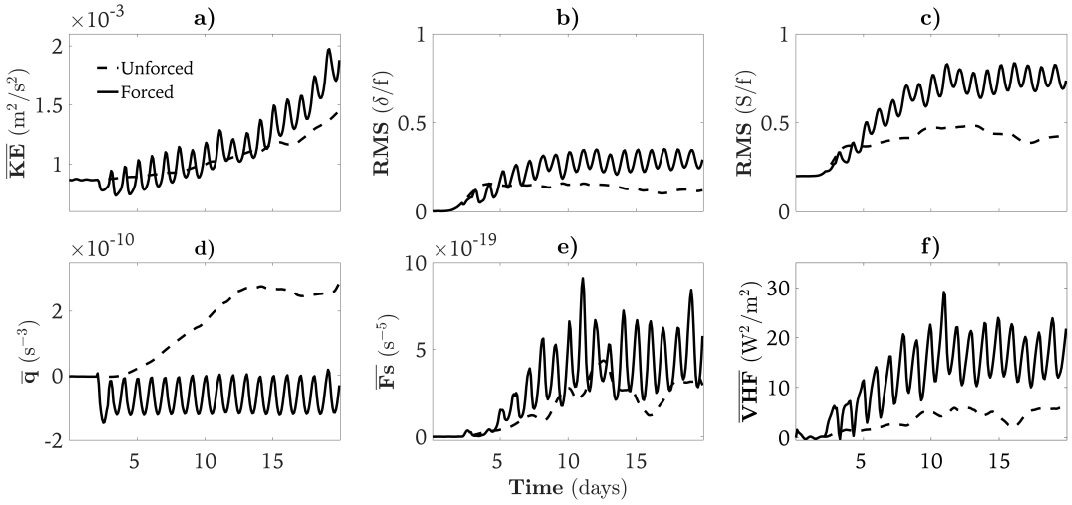

Figure 9. Temporal evolution of the physical parameters associated with the submesoscale front in both the unforced and forced simulations, starting from balanced initial thermal wind conditions (refer to Figure 21). The parameters are set as follows: a) the kinetic energy ($\overline{\text{KE}}$), b) root mean square (RMS) of the divergence normalized by f (δ_{rms}), c) RMS of the strain normalized by f (S_{rms}), d) potential vorticity ($\overline{q}$), e) frontogenesis function ($\overline{F_s}$), and f) vertical heat flux ($\overline{\text{VHF}}$). The overline denotes the volumetric average.

In the unforced case, the positive S_{rms} trend indicates the development of submesoscale baroclinic instability, which generates and expands meanders, leading to the restratification of the ML (Mahadevan & Tandon, 2006; Thomas et al., 2008). This is consistent with the positive $\overline{q}$ trend (Figure 9.d). In the forced case, the increase in the positive S_{rms} trend suggests more restratification and an increase in $\overline{q}$. However, $\overline{q}$ tends to negative values due to the negative q added by surface cooling (Thomas, 2012).

A positive $\overline{\text{VHF}}$ value indicates that the upward heat flux is dominant in the ML (Figure 9.f), as expected

from numerical (Su et al., 2020) and observational (Siegelman et al., 2019) studies. The $\overline{\text{VHF}}$ trend increases after the second day of the simulation, with this positive tendency continuing throughout the simulation. In the forced case, the positive tendency is higher than in the unforced case, tripling the upward flux.

Following Thomas (2012), we identify the types of submesoscale overturning instabilities in the ML. Figure 10 shows the temporal evolution of the probability density function (PDF) of each instability, calculated over the three-dimensional spatial domain from the surface to a depth of 100 m. The $\sum \text{PDF}_i$ equals 100 percent at each time step, where i represents the instability. In both the unforced and forced experiments, the instabilities remain invariant from IC to the 2^{nd} day of the simulation, when vertical motion occurs (as noted by $\overline{\delta_{rms}}$ in Figure 9). From the 2^{nd} day, the instability concentration differs significantly due to surface cooling.

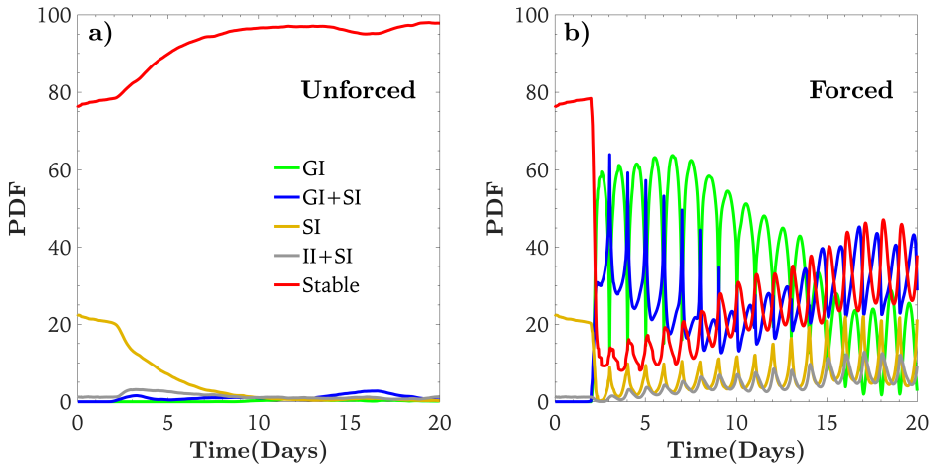

Figure 10. Temporal evolution of the probability density function (PDF) of the overturning instabilities that occur when $fq < 0$ in both the unforced (a) and forced (b) experiments. The instabilities are represented by different colored lines: the gravitational instability (GI) is shown in green, the hybrid GI and symmetric instability (SI) are shown in blue, the SI is shown in yellow, the hybrid inertial instability (II) and SI are shown in gray, and the stable flow is shown in red.

In the unforced experiment (Figure 10.a), the SI dominates the first 10 days. Meanwhile, the stable condition increases (red line), indicating that the ML is being restratified due to baroclinic instability, in agreement with Haine & Marshall (1998) and Boccaletti et al. (2007). In the forced experiment, all instabilities increase immediately after surface cooling is applied (Figure 10.b), during which time GI (green line) dominates, followed by SI. The responses of the GI and SI instabilities are faster than the BI response, which takes a couple of days to show up (as noted in the KE increase in Figure 9), in agreement with Fox-Kemper et al. (2008) and Thomas et al. (2016). A GI increase suggests enhanced mixing in the ML through convection, while an SI increase suggests enhanced mixing enhancing the

forward KE flux toward small scales and promoting the proliferation of small structures.

4.4.2 Spatial variability

Snapshots of the spatial variability of the physical parameters at a depth of 50 m are shown in Figure 11 for the unforced case and in Figure 12 for the forced case. The snapshots are taken on the 15^{th} day of the simulation when the meander behavior due to BI and the small structures induced by SI are observed.

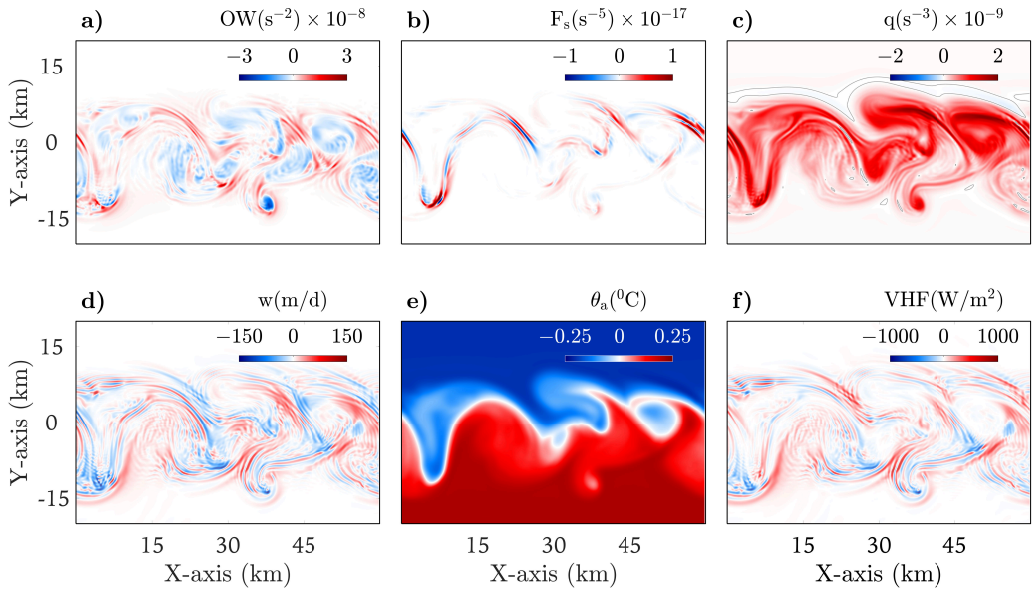

Figure 11. Snapshots of the horizontal sections of the physical parameters associated with the submesoscale front for the unforced case at a depth of 50 m on the 15^{th} day of the simulation. The parameters include a) the Okubo-Weiss quantity (OW), b) frontogenesis tendency (F_s), c) potential vorticity (q), d) vertical velocity (w), e) anomaly potential temperature (θ_a), and f) vertical heat flux (VHF). The gray contour in panel (c) denotes $q = 0$.

In Figure 11.a, the Okubo-Weiss quantity (OW), defined as OW $= \mathrm{S}^2 - \zeta^2$, shows the generation of small structures in areas where the strain is dominant (OW > 0) and the competition between frontogenesis and frontolysis is intense (Figure 11.b). High positive q values are observed over the meanders and eddies formed by submesoscale baroclinic instability, and these high q values are due to restratification. Vertical motions associated with frontal activity are observed along with intense w along fronts, displaying the dipole characteristic in frontal dynamics (Figure 11.d). Visually, the covariance between w and θ_a (Figure 11.f) in the physical space is consistent with the time series of VHF in Figure 9, depicting relatively large positive values along the frontal structures.

On the other hand, surface cooling produces an amplification of small-scale structures in all physical parameters (Figure 12). The proliferation of small structures is highlighted by the strong OW > 0 (Figure 12.a), consistent with the high SI activity. The F_s distribution is not restricted to the main frontal jet (Figure 12.b), and there are visible positive patches associated with fine-scale that are detached from the main anomaly temperature front (Figure 12.e). The negative q added by surface cooling counteracts the positive value production of q due to restratification over the meander and eddy structures (Figure 12.c). The positive q values observed in Figure 12.c suggest the dominant position of restratification leading to the vertical stability of the fluid; areas where frontogenesis activity occurs are strong (Figure 12.b), while the negative q values indicate unstable fluid with the potential for developing overturning motions leading to mixing Thomas (2012). The vertical velocity field also displays small-scale structures, as was observed in the OW field (Figure 12.d). These small-scale structures are not confined to the main front, as they are in the unforced case. Furthermore, these small-scale features correlate with the θ_a distribution in such a way that VHFs are produced at small scales (Figure 12.f).

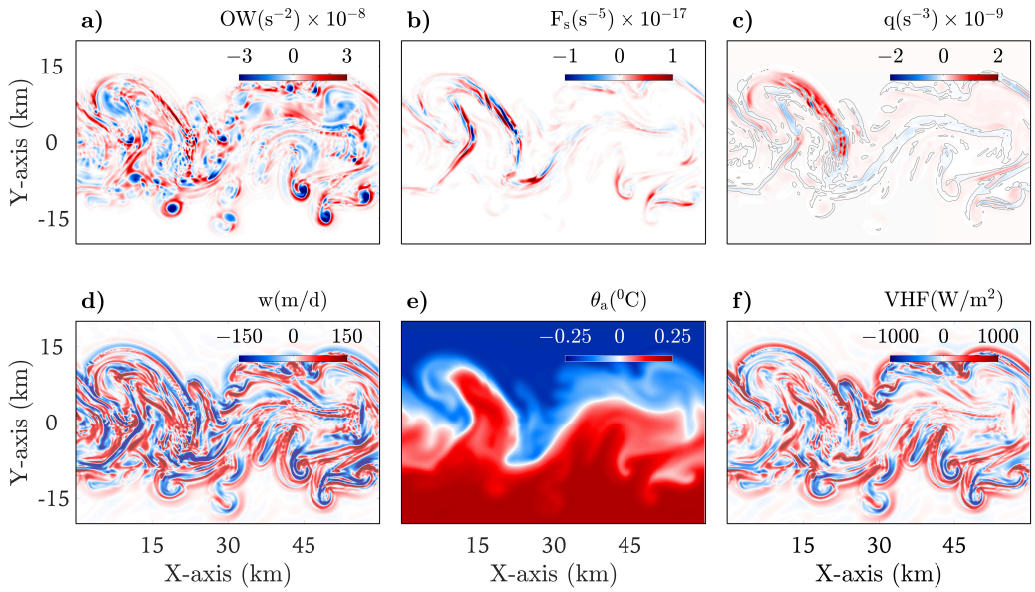

Figure 12. As in Figure 11, but for the forced case.

The main contrast between unforced and forced experiments is the proliferation of small-scale features, either along the main frontal structure or away from it. This small-scale variability is driven by a combination of gravitational and symmetric instabilities, according to Figure 10.

4.4.3 Small-scale ageostrophic motions

The KE distributions at different horizontal scales and frequencies are analyzed using spectral analysis in the frequency (ω) and wavenumber (κ) domains. The analysis is based on outputs every 30 minutes during a 14-day temporal window, allowing for the resolution of periods ranging from 1 hour to 7 days. The horizontal resolution of 200 m and the re-entrant channel size of 60 km enable the resolution of length scales from 400 m to 30 km.

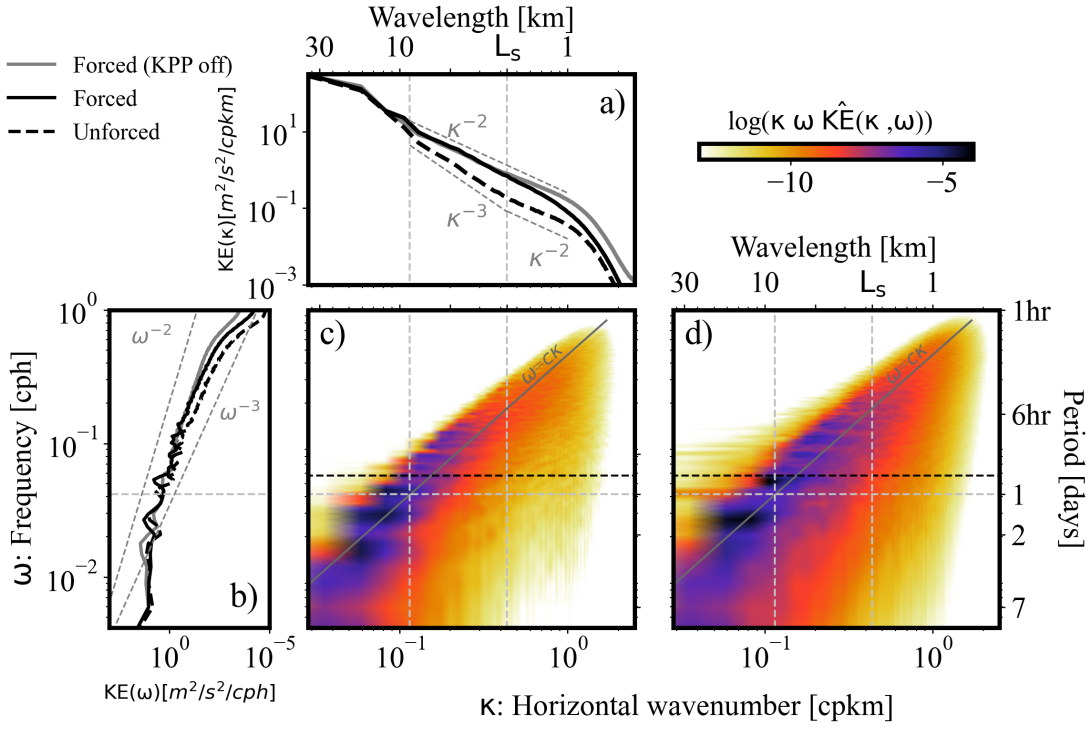

Figure 13. Frequency-wavenumber spectra of KE (KE, unit: $m^2\ s^{-2}$) for the unforced (c) and forced (d) experiments at a depth of 50 m. The spectral density is displayed in a variance-preserving form, where the values are multiplied by the wavenumber (κ) and frequency (ω) to compensate for logarithmic shrinking on both axes. In panels (c) and (d), the horizontal black dashed line represents the inertial frequency (f) and the vertical gray dashed line corresponds to the Stone fastest-growing length scale ($L_s = 2.3$ km) related to the initial conditions. The continued gray lines in both panels (c) and (d) represent the nondispersive line (ω - c$\kappa = 0$), where c corresponds to the horizontal average speed at a depth of 50 m (8.7 km/day). The frequency-wavenumber spectrum is shown in panel (b)/(a), where the black dashed line represents the unforced experiment, the black solid line represents the forced experiment, and the gray solid line represents the forced experiments without KPP. The gray dashed lines in panel (b)/(a) indicate the frequency-wavenumber slope tendency, corresponding to κ^{-3}, and κ^{-2}. The vertical gray dashed lines in panel (a) indicate the wavelength of 8.7 km and L_s, and the horizontal gray dashed line in panel (b) indicates the period of 1 day

The spectral methodology employed in this study is similar to that used in Torres et al. (2018), but in our case, there is no need to remove the spatiotemporal trend. The Hanning window is used over the cross-channel (y) and time (t) domains before applying the three-dimensional Fourier transform to the

KE (x, y, t). However, the Hanning method is not used in the x direction along the channel because this direction is periodic. To transform the simulation from an anisotropic to isotropic wavenumber spectrum, the approach described in Savage et al. (2017) is followed. To emphasize the spectral tendency and obtain a more robust analysis of the data, smoothing techniques are often employed. The Welch method is used in the spectral domain to smooth the data in terms of both the frequency and wavenumber, with a temporal window of 14 days and a time step of 1 day used to cover the entire 20-day simulation period. This approach provides a clearer picture of the overall nonlinear KE spectral distribution in the system. The frequency range is divided into two categories: the high-frequency (HF) range for frequencies greater than 1 day^{-1} and the low-frequency (LF) range for frequencies less than 1 day^{-1}. The wavenumber range is considered small-scale because it is O (1 km). Two representative scales are noteworthy, $L_s =$ 2.3 km (which is related to the initial conditions (Stone, 1970; Eady, 1949)) and the minimum structure scale solved (1 km = 5 dx), due to the spatial resolution used in the numerical simulations (dx = 0.2 km).

The frequency-wavenumber spectra of KE for both experiments are shown in Figure 13. The continued distribution of the spectral KE over the nondispersive line is the signature of the nonlinear interactions (Figures 13. c and d), where the distribution covers the high- and low-frequency ranges and the small-scale range. The extra KE in the forced case is concentrated in the high-frequency range with wavelengths smaller than 10 km, consistent with the proliferation of small features shown in Figure 12.

The integrated ω-κ spectrum of KE over the frequency range for both experiments is shown in Figure 13.a. The different spectral slopes observed in each experiment suggest changes in the dynamic regime.

In the unforced case (the black dashed line in Figure 13.a), the KE spectral slope tends toward κ^{-3} over wavelengths larger than L_s. This suggests that the quasigeostrophic (QG) theory could explain the dynamics at scales larger than L_s, where the inverse energy cascade is dominant Klein et al. (2019). The dominance of this inverse cascade is consistent with the high presence of structures larger than L_s, as noted in Figure 11.a. In the range between 1 km and L_s, a shallower spectral slope of $\kappa{-}2$ is observed, suggesting a different dynamic regime where the direct KE cascade is dominant. This implies that energy transfer occurs toward smaller scales. Finally, a steeper slope is observed at length scales of less than 1 km, which is attributed to numerical dissipation.

In the forced case (the black solid line in Figure 13.a), a steeper spectral slope is observed at wavelengths larger than 8.7 km, followed by a spectral slope with a tendency toward κ^{-2} over the 1-8.7-km wavelength scale range. The diurnal cycle lengthens the transition scale from L_s to 8.7 km. This means that

ageostrophic motions occupy a relatively broad range of scales. The κ^{-2} slope suggests that a dynamic regime could be explained by surface quasigeostrophic (SQG) theory (Klein & Lapeyre, 2009). Fox-Kemper et al. (2008) reported that nonlinear interactions across scales established a KE spectrum in κ^{-2} after day 6 of the simulation. On the one hand, frontogenesis leads to smaller scales, and on the other hand, the inverse cascade strengthens longer scales. This scenario fits in the unforced case. However, in the forced experiment, the diurnal cycle triggers the proliferation of small scales that, combined with frontogenesis, promote the flattening of the spectral slope from κ^{-3} to κ^{-2}.

The wavenumber spectrum of the KE for a situation similar to the forced experiment but without KPP is shown in Figure 13.a (gray solid line). The spectral slopes at wavelengths larger than L_s are κ^{-2}, similar to the experiment with KPP. The spectral slope at wavelengths less than L_s is $\kappa^{-5/3}$, different from the experiment with KPP. It is notable in Figure 13.a that over this range, the KE value is greater than that in the experiment with KPP. This result suggests that the KPP mixing scheme dampens the movements at scales smaller than L_s.

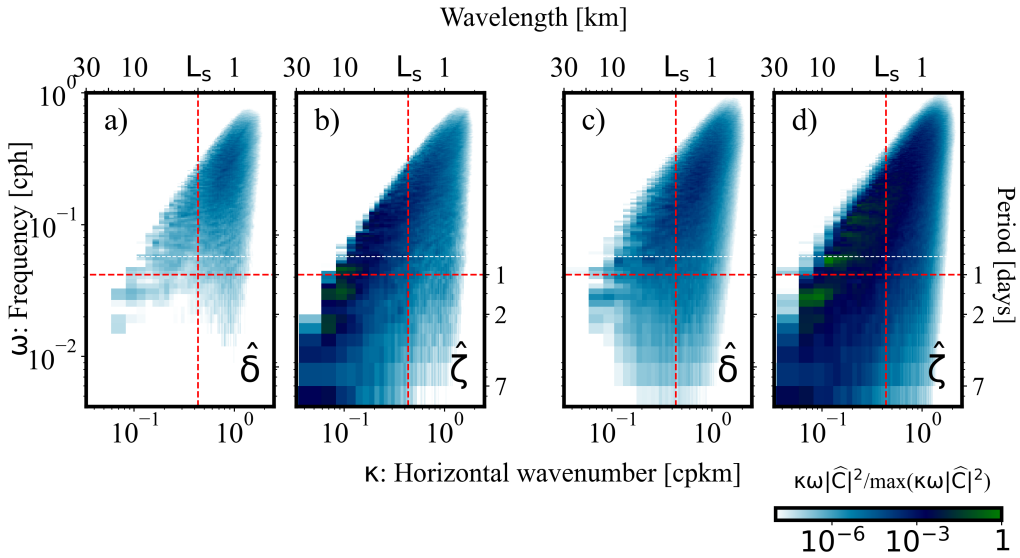

Figure 14. Frequency-wavenumber spectra of the divergence (δ) and relative vorticity (ζ) shown for the unforced experiment (a and b) and the forced experiment (c and d). The spectral energy for each parameter, denoted as C, is normalized by the maximum value between the corresponding unforced and forced spectral energies. In all boxes, the green dashed line indicates the low-frequency limit (> 1 day^{-1}) and high-frequency limit (< 1 day^{-1}), while the horizontal dashed red line corresponds to the inertial frequency f and the vertical dashed red line corresponds to the Stone fastest-growing length scale ($L_s = 2.3$ km); the Stone fastest-growing length scale is related to the initial conditions of the numerical simulation.

The Helmholtz decomposition of the spectral KE offers insight into the possible dynamics within the observed spectral range by looking at the partition between the rotational and divergent components.

Figure 14 presents the divergent ($\hat{\delta}$) and rotational ($\hat{\zeta}$) components. The length scale L_s is crucial for identifying the dominant KE component in both experiments.

In the unforced case (Figures 14.a and b), we observed that the spectral range with κ^{-3} (larger than L_s) (Figure 13.a) is dominated by the rotational component; this is characteristic of the QG regime. On the other hand, in the spectral range with κ^{-2} ($L_s - 1km$) (Figure 13.a), we found that the divergent component has a high magnitude and is close to the rotational component.

In the forced case (Figures 14.c and d), we observed that the spectral range with κ^{-2} over wavelengths larger than L_s (Figure 13.a) is dominated by the rotational component. While κ^{-2} over wavelengths smaller than L_s, the rotational and divergent components confer significant contributions with magnitudes higher than those obtained in the unforced case.

The spectral analysis confirms the impact of the diurnal cycle on the kinetic energy by triggering the generation of small-scale ageostrophic motions. According to Figure 12, these motions also have a signature on VHFs. In the next section, the net effect of VHFs associated with ageostrophy is addressed.

4.4.4 Vertical heat flux in the mixed layer

Figure 15 displays a snapshot of the three-dimensional VHF variabilities in the ML on the 15^{th} simulation day for the unforced and forced experiments. The VHF exhibits null horizontal variability in the surface boundary layer, as expected because the vertical velocity is zero at z = 0 m, while the VHF reaches a maximum around the middle of the ML at approximately a 50-m depth.

The vertical structures observed in the ML in the unforced case (Figure 15.a) primarily result from the development of submesoscale BI, as indicated by the few overturning instabilities in Figure 10.a. In contrast, in the forced case (Figure 15.b), the vertical structures in the ML are formed by the intensification of BI and the increased overturning instabilities (Figure 10.b). The vertical sections of Figures 15.a and b show that the VHF develops throughout the entire ML and beneath it. However, in the forced case, positive VHFs can extend even deeper. Figure 15.c depicts the vertical profiles of the horizontally averaged VHF corresponding to panels 15.a and 15.b. These profiles reveal that the net VHF is positive (upward) within the ML and weakly negative (downward) beneath the ML. The depth of the horizontal average of the vertical buoyancy gradient is noted (green lines in Figure 15.c). The ML depth is shallower from -100 m to approximately -90 m in the unforced case, while it is deeper

from -100 m to approximately -120 m in the forced case; the 100-m depth corresponds to the initial conditions (Figure 7.d). These results can be explained by the competition between restratification by BI and mixing induced by diurnal surface cooling (Mahadevan et al., 2010; Callies & Ferrari, 2018).

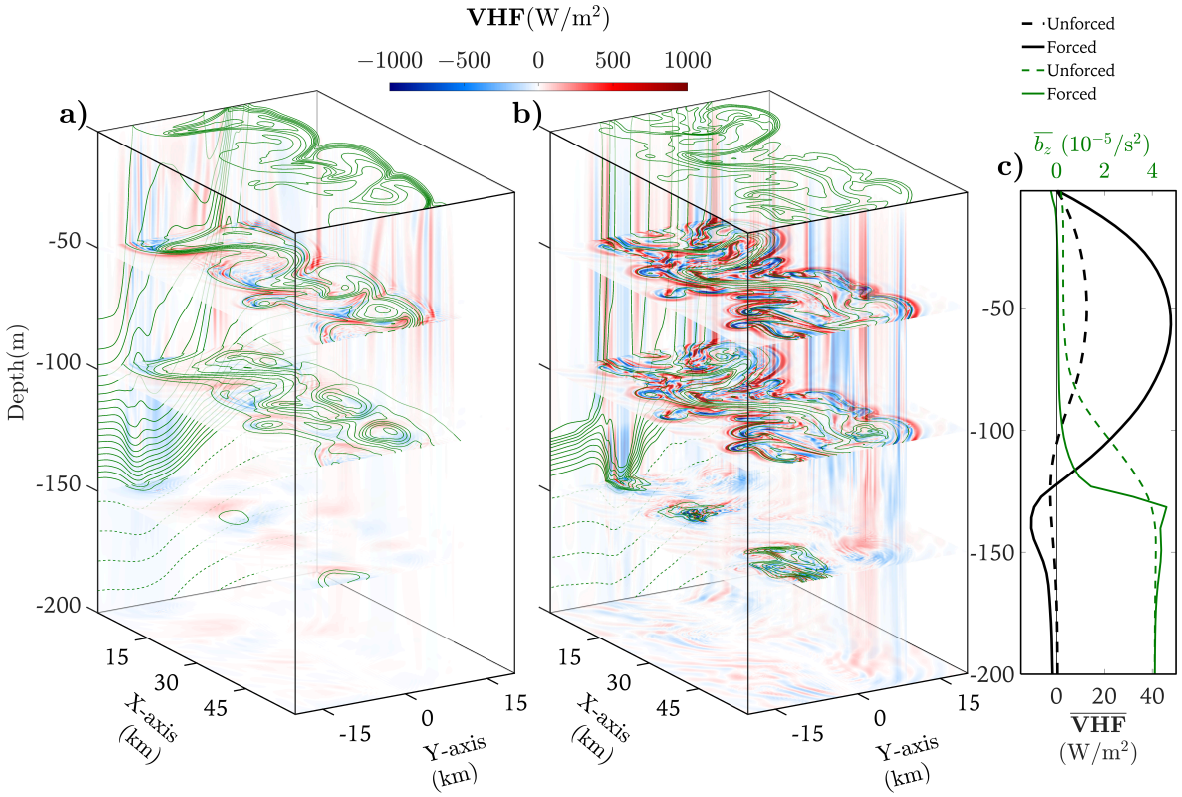

Figure 15. Three-dimensional snapshots of the VHF on the 15^{th} day of simulation in (a) the unforced case and (b) the forced case. The vertical profiles of the horizontal average VHF are shown in black lines, and the vertical profiles of the horizontal average of $N^2 = b_z$ are shown in green lines (c). The vertical profiles were obtained from panels (a) and (b). The green contours in panels (a) and (b) represent the buoyancy isolines with contour intervals of 1×10^{-4} ms^{-2} for continuous lines and 5×10^{-4} ms^{-2} for dashed lines.

As illustrated in Su et al. (2020), particularly in their Figure 3, strain-induced VHFs, arising via frontogenesis, are confined at the edges or in between co-interacting eddies, collocated with strong density gradients. They reported that these VHF components are associated with motions with frequencies $<$ f. In the context of our experiments, the low-frequency VHFs in Su et al. (2020) are consistent with our unforced experiment. VHFs are located along the main anomalous temperature front. The main driver mechanism is frontogenesis. On the other hand, the high-frequency VHFs in Su et al. (2020) are not only located along the main density gradients but also inside, at the periphery of, and between the mesoscale eddies. Such a distribution resembles Figure 12.f and Figure 12.b. The time series of the physical parameters and the time series of the mixed layer instabilities show clear diurnal cycles. However, the question of whether the VHFs spread out at frequencies higher than 1 day^{-1} arises, as shown

in Su et al. (2020). To answer this question, the co-spectrum of VHF in the frequency-wavenumber space is computed.

4.4.4.1 VHF co-spectrum

We used the methodology presented in Su et al. (2020) to calculate the VHF co-spectrum; this co-spectrum measures the relationship between the vertical velocity w and temperature anomalies (θ_a), a crucial aspect of understanding the VHF. We applied the smoothing Welch method to obtain a more robust data analysis, with a temporal window of 10 days and a time step of 1 day from the 5^{th} to the 20^{th} simulation day. By analyzing the VHF in the spectral domain, we can assess the impact of surface cooling on the VHF in both high-frequency (HF) and small-scale ranges.

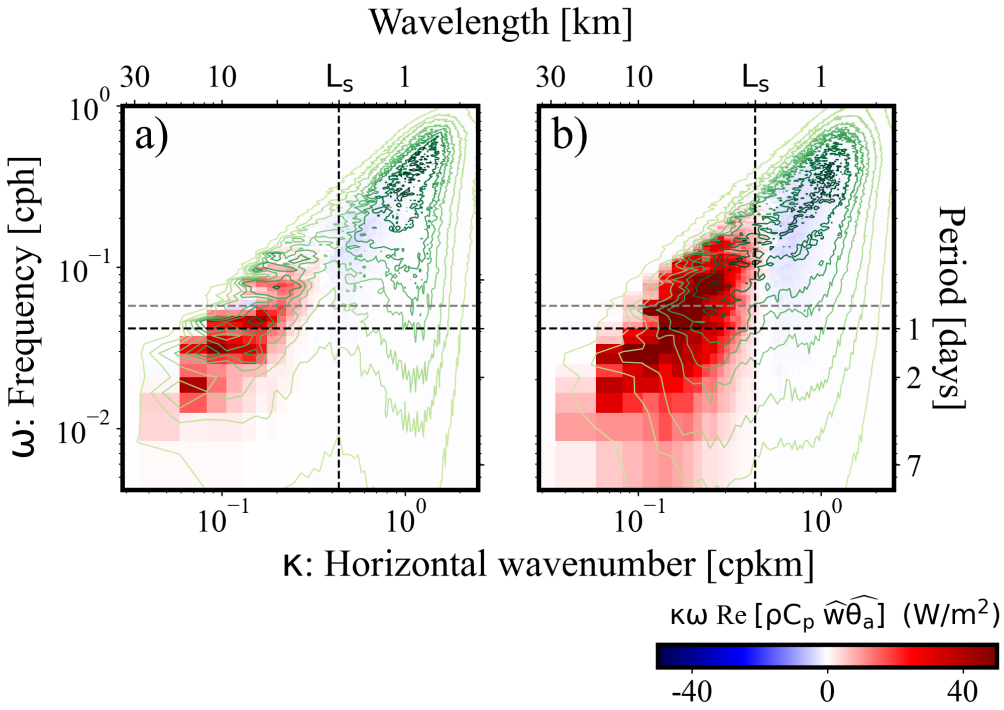

Figure 16. Vertical heat flux co-spectrum with the unforced (a) and forced (b) experiments of the vertical heat flux. The horizontal black dashed lines indicate the low-frequency limit ($>$ 1 day^{-1}) and high-frequency limit ($<$ 1 day^{-1}), and the dashed line indicates the inertial frequency (f). The vertical dashed black line indicates Stone's fastest-growing length scale (L_s = 2.3 km) relative to the initial conditions. The contours are the vertical velocity spectra, the dark colors represent high variability, and the light colors represent low variability. The co-spectra density (Re[$\rho C_p \widehat{w}\widehat{\theta_a}$], unit: Wm^{-2}cph^{-1}cpkm^{-1}) is shown in a variance-preserving form; that is, the spectra are multiplied by the wavenumber (κ) and frequency (ω) to compensate for logarithmic shrinking on both axes. The calculations are made at a depth of 50 m.

Figure 16 displays the co-spectrum obtained for both the unforced and forced experiments at a depth of 50 m, where the maximum VHF is located. The critical length scale L_s and 1 day^{-1} frequency that separate the HF and low-frequency (LF) regimes are also marked. The positive values in both experiments indicate that the heat transport in the vertical direction is upward. VHFs are continuously distributed across the 1 day^{-1} frequency, covering both the LF and HF ranges. In the unforced case, the upward flux reaches a frequency of (10 h)$^{-1}$, while in the forced case, it reaches a higher frequency close to (6 h)$^{-1}$. The LF VHFs are close to (7 day)$^{-1}$ in the unforced case, while the LF VHFs extended down to (7 day)$^{-1}$ in the forced case.

It is worth noting that the VHFs exhibit a sign change near L_s from positive to negative, resulting in positive VHFs at wavelengths larger than Ls and negative VHFs at wavelengths smaller than L_s. The contours of the vertical velocity spectrum revealed that the negative VHFs are associated with intense vertical motions, which in turn are associated with high divergence and relative vorticity values (Figure 14). At this spectral range, ageostrophic motions are dominant, characterized by a spectral slope of κ^{-2}. In these coupled experiments, the VHFs are limited by the L_s.

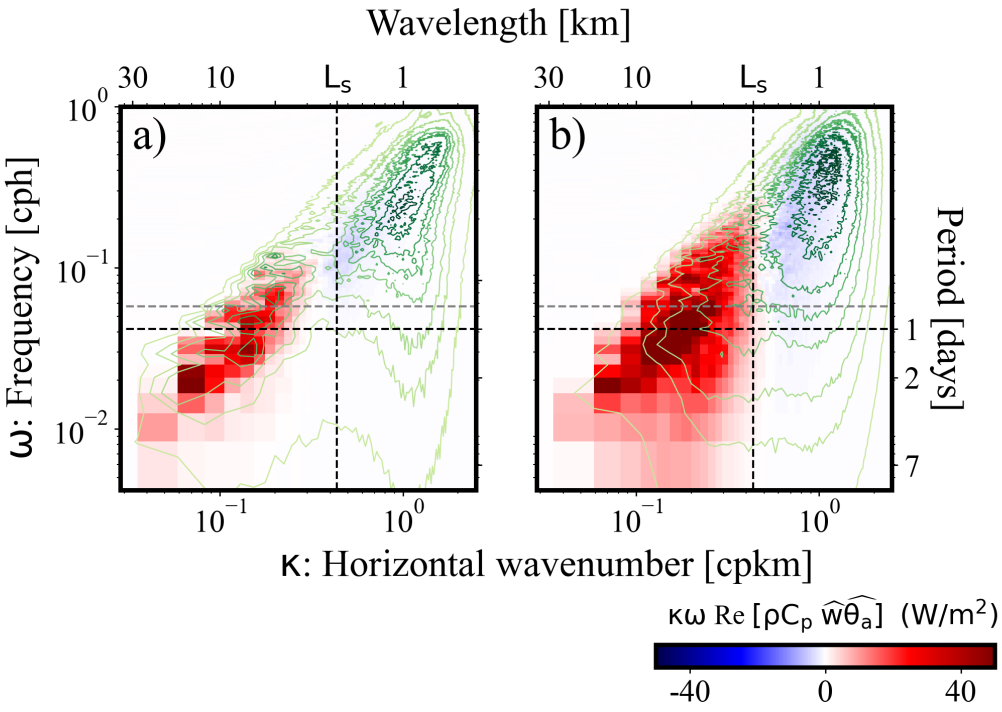

Figure 17. As in Figure 16, but the K-profile parameterization scheme is inactive.

The VHF co-spectrum was obtained for an additional set of experiments with similar configurations and initial conditions, except that the vertical mixing scheme KPP was turned off, as shown in Figure 17.

The experiment forced with KPP exhibited the closest configuration to the LLC4320 simulation that Su et al. (2018) and Su et al. (2020) used to compute their VHF co-spectra, especially in the winter season. Similar features of the VHF co-spectra with KPP are also observed in the VHF co-spectra without KPP, but a simple inspection of the positive VHF shows greater values when the KPP is active.

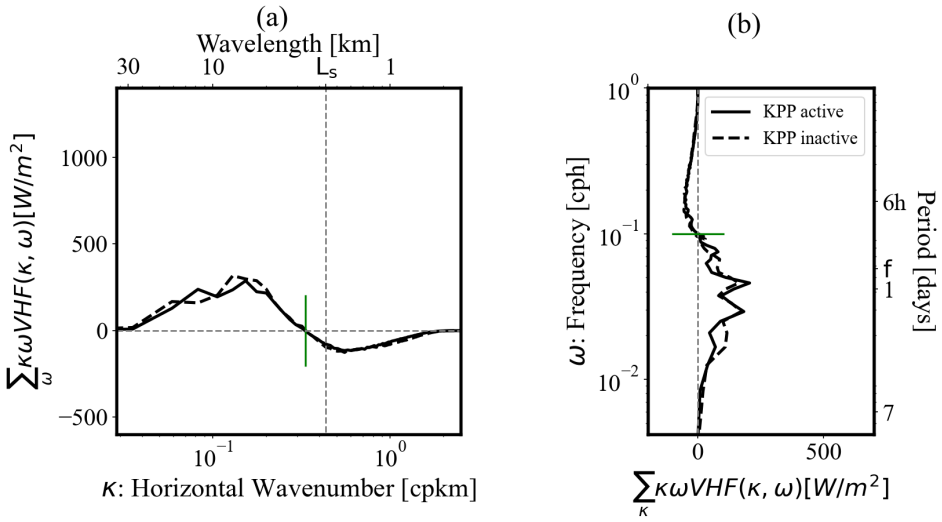

Figure 18. Results obtained for the unforced case. The wavenumber spectrum of the sum in the frequency of the vertical heat flux co-spectrum (a) and the frequency spectrum of the sum in wavelength of the vertical heat flux co-spectrum (b). In panel (a), the vertical dashed line corresponds to Stone's fastest-growing length scale ($L_s = 2.3$ km) related to the initial conditions, while the vertical green line indicates a wavelength of 3 km. In panel (b), the horizontal green line indicates the frequency of (10 h)$^{-1}$. In both panels (a) and (b), the black continuous line indicates the simulation with K-profile parameterization (KPP), and the dashed black line indicates the simulation without KPP.

To identify more differences and similarities between the experiments with and without KPP, we integrated the corresponding VHF co-spectra frequency and wavenumber values for both the unforced case (Figure 18) and forced case (Figure 19).

In the unforced case, over the wavenumber range where the VHF is positive, the VHFs did not show any significant differences. Both with and without KPP, the maximum VHF is approximately 7 km. Over the wavenumber range where the VHF is negative, the VHFs are similar (Figure 18.a). The wavelength where the sign of VHF changes from positive to negative values is 3 km; this value is greater than the L_s value. This critical wavelength increase is consistent with the tendency toward the restratification of the ML, as noted in Figure 15.c. Over the frequency range where the VHF is positive, no significant differences in the VHFs are observed. In both the simulations with and without KPP, the maximum VHF lies between f and (2 day)$^{-1}$. Over the frequency range where the VHFs are negative, the VHFs are similar. The frequency of (10 h)$^{-1}$, where the sign of the VHF changes, delimits the reach toward the high frequency of the upward heat flux (Figure 18.b). The high similarity between wavelengths less

than L_s and frequencies greater than (10 h)$^{-1}$ is due to the reduced activity of overturning instabilities in the ML, as shown in Figure 10.a.

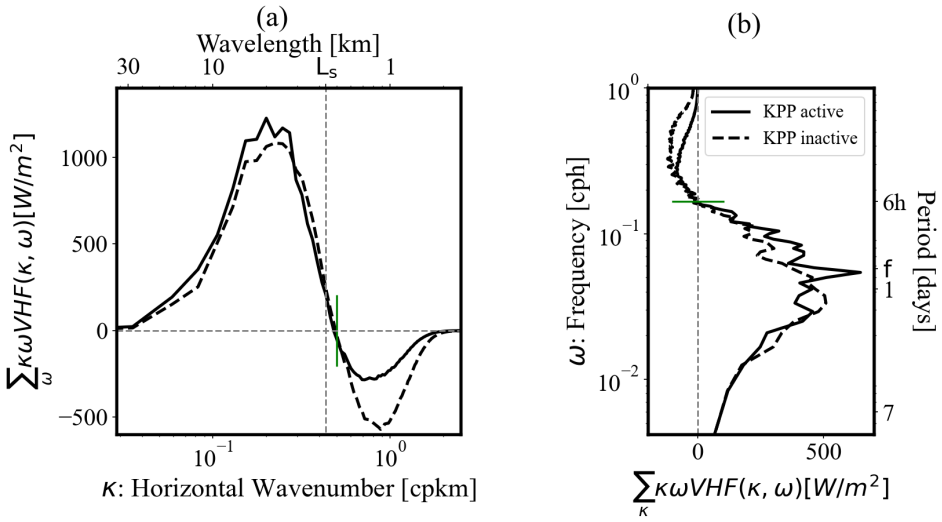

Figure 19. Same as Figure 18 but for the forced case. The green lines in panels (a) and (b) indicate a wavelength of 2 km and a frequency of (6 h)$^{-1}$, respectively.

In the forced case, where surface cooling enhances the dynamics over all wavelengths and frequencies (Figure 13), significant differences are observed in the VHFs between experiments with and without KPP, when compared to the unforced case. For wavelengths where the VHFs are positive, the VHF amplitude is enhanced when KPP is active, where the VHFs are negative, the amplitude of the VHF is reduced by a factor of two when KPP is active (Figure 19.a). This reduction is consistent with the relatively low KEs obtained in the experiment with KPP compared to those obtained in the experiment without KPP (Figure 13.a). The wavelength at which the VHF sign changes from positive to negative values is 2 km; this wavelength is shorter than L_s. This critical wavelength decrease is consistent with the mixing of the ML trend noted in Figure 15.c. The maximum positive VHFs obtained in the simulations both with and without KPP occur at 5 km, indicating a translation toward small positive flux scales when the forcing is active.

The distribution of VHFs in frequency between experiments with and without KPP shows significant differences (Figure 19.b). The maximum of positive VHF is located between f and 2 day^{-1} when KPP is inactive, while it is located at the inertial frequency when KPP is active. The VHF peak at the inertial frequency suggests that KPP activation promotes the generation of inertial waves driven indirectly by surface cooling, which have a constructive interaction with submesoscale vertical motion with a similar frequency. In both with and without KPP, the maximum of positive VHF spreads across HF and LF

parts, where the amplitude is greater when KPP is active, mainly for frequencies greater than 1 day^{-1}.

The frequency distributions of VHFs show significant differences between the experiments with and without KPP (Figure 19.b). The maximum positive VHF is located between f and (2 day)$^{-1}$ when the KPP is inactive, while it is located at the inertial frequency when the KPP is active. The VHF peak at the inertial frequency suggests that KPP activation promotes the generation of inertial waves driven indirectly by surface cooling; these waves undergo constructive interactions with submesoscale vertical motions with similar frequencies. In both the simulations with and without KPP, the maximum positive VHF spreads across the HF and LF parts; the amplitude is greatest when KPP is active at frequencies greater than 1 day^{-1}. For frequencies where the VHF is negative, the VHF is reduced when KPP is active. As mentioned, the positive VHFs reach higher frequencies under these conditions than in the unforced case and are closed by the frequency of (6 h)$^{-1}$, where the VHF sign changes from positive to negative.

The activation of KPP, as a vertical mixing scheme, mitigates the production of small-scale features driven by GI and SI that set the ageostrophic regime and trigger negative VHFs but, at the same time, enhance positive VHFs either by direct contributions or by indirect effects associated with inverse kinetic energy cascades.

4.4.4.2 Vertical heat flux in the California Current System from submesoscale-permitting, tidal-resolving simulation

The mechanism behind VHFs from idealized experiments has been demonstrated. However, state-of-the-art ocean numerical simulations consider not only high-frequency atmospheric forcing but also internal gravity waves (IGWs). Su et al. (2020) identified a potential explanation for the interaction between IGWs and submesoscale motions. In our idealized simulations presented in this manuscript, we focus our attention on daily surface cooling. Figure 16 shows that the maximum VHF amplitude occurs at the diurnal frequency. This highlights the importance of daily surface cooling. However, discrepancies and similarities can be seen between the co-spectrum in Figure 16 and the co-spectrum in the realistic simulation.

A submesoscale-permitting, tidal-resolving simulation is used in this work to compute the co-spectrum of VHFs for further comparison with the idealized experiments. The horizontal spacing grid of the realistic

simulation is 500 m, twice as large as that in the idealized simulations but sufficient to resolve mixed-layer instabilities. The simulation encompasses the California Current System. The regional domain is nested within the global ocean numerical simulation known as LLC4320, with a nominal grid spacing of $1/48^{\circ}$. The forcing at the lateral boundaries includes external and internal tides, near-inertial waves, and high-frequency IGWs. High-frequency (1 h^{-1}) surface atmospheric forcing data from ERA5 are used in the regional domain, allowing a realistic diurnal cycle to be simulated.

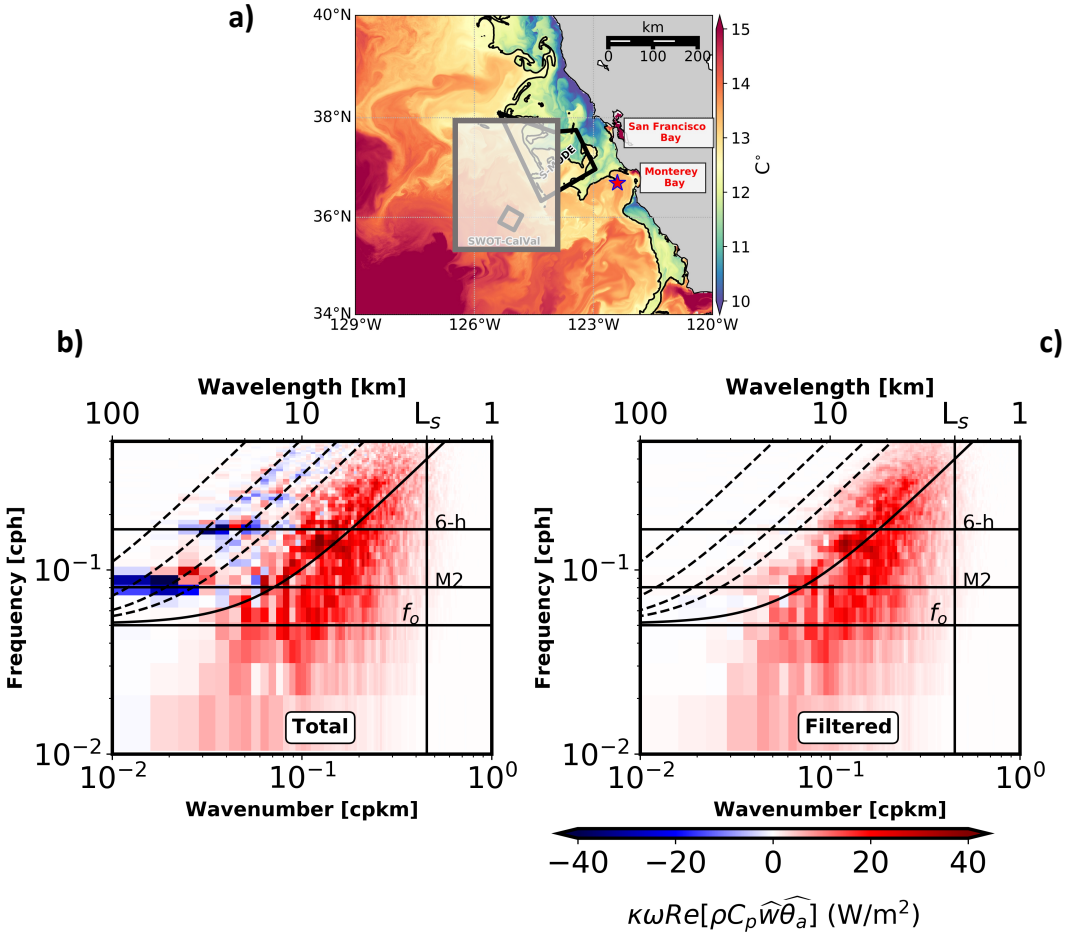

Figure 20. (a) Sea surface temperature from high-resolution (dx = 500 m) and tidal-resolving simulations. (b-c) Vertical heat flux co-spectrum from total fields, including internal gravity waves and submesoscale motions (b) and after removing internal gravity waves dynamically following the method outlined by Torres et al. (2022). The horizontal black lines indicate the inertial frequency (f_o), the M2 internal gravity waves (M2), and the tidal harmonic with a frequency of (6 h)$^{-1}$. The vertical black line indicates Stone's fastest-growing length scale (L_s = 2.3 km) related to the background buoyancy gradients. The co-spectra density (Re[$\rho C_p \widehat{w}\widehat{\theta_a}$], unit: Wm^{-2}cph^{-1}cpkm^{-1}) is shown in a variance-preserving form; that is, the density is multiplied by the wavenumber (κ) and frequency (ω) to compensate for logarithmic shrinking on both axes. The calculations are made at a depth of 50 m. The gray-shaded square marks the domain used to compute the co-spectrum. The two black polygons mark the domains of two ongoing oceanographic experiments: the Surface Water and Ocean Topography(SWOT)-Cal/Val and Sub-Mesoscale Ocean Dynamics Experiment (S-MODE). The in-situ observations from these two experiments would confirm or infirm the findings of this numerical study.

Similarities and discrepancies arise between the idealized and realistic VHF co-spectra. First, the positive

VHF component in the realistic simulation is continuously distributed across the LF and HF components. The maximum positive VHF values are in the 10 km - L_s wavelength range, as in the idealized experiments. Second, the VHF distribution along wavelengths is limited by the L_s scale, which was computed using model outputs obtained in the realistic simulation. Since the KPP vertical mixing scheme was used in the realistic simulation, ageostrophic nonwave motions with wavelengths smaller than Ls were damped, as demonstrated in Figure 13.a and 19. However, a striking discrepancy occurs in the position of the maximum positive VHFs in the realistic simulation; this position is located at higher frequencies than in the idealized experiment with KPP. In the realistic simulation, the maximum value is between M2 (12.42 h) and 6 hours (Figure 20.b). The IGW field is dynamically removed following Torres et al. (2022) (Figure 20.c). The dynamical filter described by Torres et al. (2022) is suitable for removing low-mode baroclinic IGWs; however, it fails to disentangle high-frequency and small-scale IGWs that are trapped within submesoscale fronts, which in turn creates a constructive interference pattern with the potential to enhance VHFs, as suggested by Thomas (2017) and Su et al. (2020). Therefore, this discrepancy leads us to keep the hypothesis of VHFs being induced by the interactions between small-scale and high-frequency IGWs with submesoscale fronts.

4.5 Conclusions

In this study, we examined the submesoscale VHF variability in the ML under diurnal surface cooling conditions. We evaluated the capacity of atmospheric forcing data to modulate high-frequency ($\omega > 1$ day^{-1}) and small-scale ($\kappa^{-1} < 10$ km) VHFs.

This study provides insight into the different mechanisms and dynamics of baroclinic instabilities in the presence and absence of external forcing. The PDF analysis of baroclinic instabilities in the ML reveals distinct behavior between the forced and unforced experiments. In the unforced experiment, the SI dominates with a negative tendency, indicating a reduction in KE transfer toward smaller scales and a restratification of the ML when the BI takes over. On the other hand, in the forced experiment, all instabilities increase immediately after surface cooling is applied, with the GI dominating, suggesting enhanced mixing in the ML through convection; in addition, the SI promotes the proliferation of ageostrophic high-frequency and small structures mediating the KE flux toward small scales while simultaneously reinforcing scales with frequencies smaller than 1 day^{-1} via the inverse KE cascade.

The VHF co-spectrum provides insight into the impact of surface cooling on high-frequency VHFs. Pos-

itive values in both forced and unforced experiments indicate upward heat transport, with this transport continuously distributed across both the low- and high-frequency ranges. The unforced experiment with KPP reveals that strain-induced frontogenesis and SI are not sufficient to generate VHFs with frequencies higher than (10 h)-1. Diurnal surface cooling provides the additional mechanisms by which VHFs are enhanced directly through SI and GI instabilities and indirectly through an inverse cascade that reinforces the strain-induced frontogenesis at frequencies smaller than 1 day^{-1}.

Our comparison of the VHF co-spectrum between idealized and realistic simulations displays similarities and discrepancies. The co-spectrum from the idealized simulation resembles the continuous distribution of VHFs across the LF and HF components. Additionally, L_s limits the distribution of VHFs down to small scales. However, one striking discrepancy is the position of the maximum positive VHFs in the frequency-wavenumber space. In the realistic simulation, the maximum value occurs at higher frequencies, between (12.42 h)$^{-1}$ and (6 h)$^{-1}$, than in the idealized case, when it occurs at the diurnal frequency. Since the realistic simulation does consider small-scale and high-frequency IGWs, the hypothesis proposed by Su et al. (2020) about the potential interaction between IGWs and submesoscale fronts that could give rise to large HF values still holds.

Finally, the findings in the study could be useful for further interpretations of observations from the ongoing S-MODE mission (Farrar et al., 2020) (see Figure 20.a). One of the particularities of S-MODE is its multiscale observation platform; this characteristic allows data to be obtained at resolutions from mesoscales down to fine-scale motions subject to diurnal surface cooling/heating. On the other hand, the findings reported here can also be confirmed by S-MODE observations.

Chapter 5. Enhancement of submesoscale vertical heat flux by wind stress

5.1 Introduction

In the last decade, numerical and observational studies have demonstrated that the submesoscale regime plays a role in transporting heat, nutrients, and momentum between the air-sea interface and the ocean interior, thus playing a key role in regulating Earth's climate and biological productivity (Klein et al., 2019; Taylor & Thompson, 2022).

Novel global numerical simulations with sufficient spatial resolution to capture submesoscale motions (Menemenlis et al., 2021) have highlighted the global significance of the submesoscale VHF within the mixed layer, particularly during winter, where it can be up to 10 times greater than the mesoscale VHF (Su et al., 2018). On average, the submesoscale flux is directed upward, heating the upper part of the mixed layer, similar to the mesoscale VHF, but contrary to the downward diffusion of heat (Klein et al., 2019). In terms of scale, the submesoscale VHF spans dimensions from $\sim$1 km to $\sim$30 km and timescales from $\sim$1 h to $\sim$7 days. Su et al. (2020) noted that the VHF signals on timescales of O(days) are driven by secondary circulations associated with submesoscale fronts. In contrast, the signals on timescales of O(hr) are likely driven by atmospheric forcing and the nonlinear interactions between submesoscale fronts and other structures within the mixed layer Su et al. (2020). The coexistence of these forcings and their interactions complicates the problem.

Using numerical experiments that reproduce submesoscale dynamics in the mixed layer, Fox-Kemper et al. (2008) reported that surface cooling reinforces the submesoscale dynamics. Additionally, (Aparco-Lara et al., 2023) reported that this process reinforces the triggering of the high-frequency VHF signals, i.e., signals of O(hr), with the maximum high frequency achieved by surface cooling ($\sim 1/6$ h^{-1}) being lower than that reported by Su et al. (2020) ($\sim 1/1$ h^{-1}). Thomas et al. (2008); McWilliams et al. (2015); Barkan et al. (2017) reported that wind stress in a down-front arrangement also reinforces the submesoscale dynamics, while Thomas (2017) showed that internal waves can interact with these dynamics to further enhance them. This source of submesoscale dynamics reinforcement has the potential to trigger high-frequency VHF.

This study investigates the high-frequency submesoscale VHF induced by wind stress in a down-front configuration. Using numerical simulations, we simulate an idealized submesoscale front under two

scenarios: an unforced case, in which the front evolves freely, and a forced case, in which the front is subjected to wind stress. This approach allows us to isolate and analyze how the orientation and magnitude of wind stress influence submesoscale dynamics, particularly in generating high-frequency VHF. We aim to reproduce frequencies that exceed those achieved by surface cooling, which reached values of up to $1/6$ h^{-1} according to Aparco-Lara et al. (2023). Understanding these dynamics is crucial for advancing our knowledge of the mechanisms that intensify submesoscale activity in the mixed layer, especially when the wind stress is aligned in a down-front direction and has the potential to trigger even higher frequencies.

5.2 Numerical model

We use the nonhydrostatic version of the MITgcm (Alistair et al., 2018; Marshall et al., 1997)) to simulate a baroclinic unstable jet that generates submesoscale structures within a re-entrant channel. The along-channel dimension (x-axis, 60 km) is designed to accommodate the wavelength of $\sim$60 km associated with the horizontal baroclinic deformation radius of $\sim$9.7 km, which corresponds to a mixed layer depth of $\sim$100 m and a density contrast of $\sim$1 kg/m^3 between the mixed layer and the interior, i.e., below 100 m. The cross-channel dimension (y-axis) is 420 km, centered where the jet velocity reaches its maximum value (Figure 21.b). The y-axis is larger than the submesoscale front width (10 km) to minimize noise from the lateral boundaries, in particular when wind stress is applied. The vertical dimension (z-axis) extends to 300 m.

We use a regular horizontal grid of 200 m to resolve structures of $O(1\text{ km})$, which is sufficient to capture the fastest-growing length scale (L_s) of instabilities in the mixed layer. For the numerical experiment with weak stratification (i.e., a Richardson number, R_i, of 1 and an average jet velocity of 0.04 m/s), the L_s is estimated to be 2.3 km, with the critical L_s (when R_i approaches zero) being 1.5 km, as predicted by the linear theory described in Eady (1949) and Stone (1970). We use a vertical irregular grid to reduce the computational time, with the grid spacing increasing from $\sim$3 m in the mixed layer to $\sim$15 m below the mixed layer.

The numerical experiments use a nonhydrostatic approach because the wind stress can produce significant vertical acceleration (Barkan et al., 2017). For the vertical mixing, we use the non-local KPP turbulent mixing closure scheme (Large et al., 1997).Additionally, a constant Coriolis parameter is applied, set to $f = 10^{-4}\,\text{s}^{-1}$.

5.2.1 Initial conditions

Following the method described in Fox-Kemper et al. (2008), we construct an idealized submesoscale thermal front as the initial condition, similar to that used by Aparco-Lara et al. (2023). Figure 21.a shows the potential temperature where the horizontal contrast along the y-axis into the mixed layer is the submesoscale thermal front (the isolines of density also note the front). The zonal velocity due to the Rossby adjustment conditions is indicated by the white lines contours, where the velocities in the mixed layer are greater than the velocities below the mixed layer. The vertical profile of the density field (Figure 21.c) and the vertical stratification (Figure 21.d) show a low density and a weak stratification from the surface to 100 m deep, both of which are consistent with the vertical extension of the mixed layer.

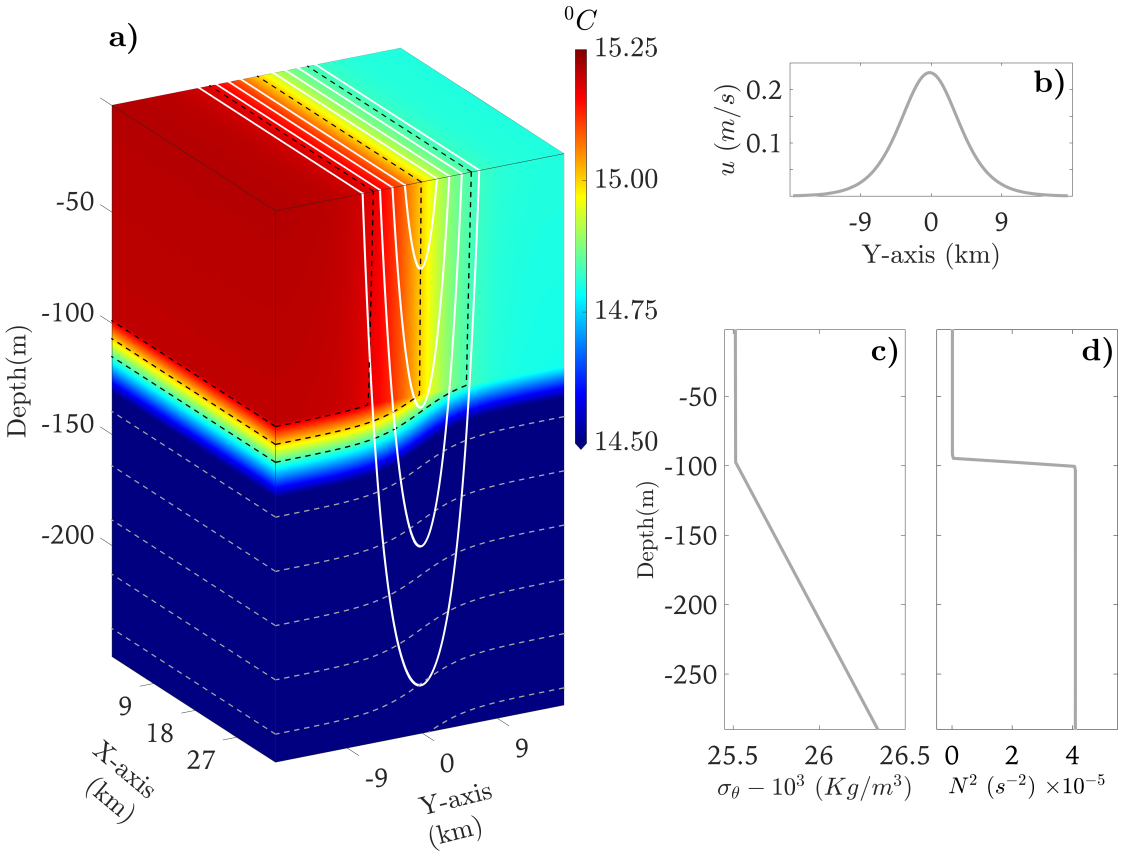

Figure 21. Initial conditions of the submesoscale thermal front in thermal wind balance. (a) The white contours indicate the along-channel velocity, and the dashed contours indicate the buoyancy. The white contour interval is 0.05 ms^{-1}, the dashed contour interval within the mixed layer (ML) is 0.003 ms^{-2}, and the dashed contour interval below the ML is 0.01 ms^{-2}. (b) Initial surface horizontal velocity. (c) Initial vertical profile of density. (d) Buoyancy frequency squared. Figure from Aparco-Lara et al. (2023).

5.2.2 Experiments

Initially, a numerical simulation of a submesoscale front with free evolution is conducted until day 20, by which time the baroclinic instability has generated eddy structures and the frontal meander has reached its most unstable wavelength (approximately 60 km). The 20th day of the simulation is used as the initial condition for the subsequent experiments. Two experiments are conducted: one with free evolution and the other forced by wind stress in a downfront arrangement. The simulation time for both experiments is 10 days. During this period, the noise generated by the lateral boundaries, which occurs when the wind stress force is activated, does not influence the evolution of the submesoscale system because of the large y-axis dimensions of the reentrant channel.

5.2.2.1 Downfront wind forcing

The surface wind stress in a downfront arrangement is the most efficient setup for increasing submesoscale front activity by promoting instabilities in the mixed layer that drive turbulence (Thomas et al., 2008; Thomas, 2012; Gula et al., 2014, 2022).

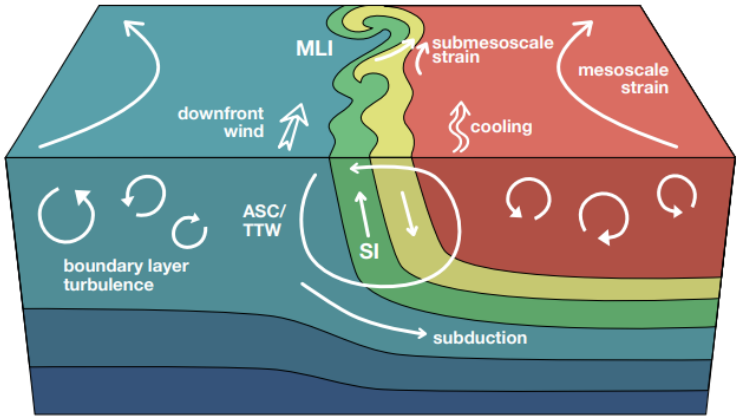

Figure 22. Idealized depiction of various submesoscale processes. Convergent mesoscale strain drives frontogenesis. Surface cooling or a downfront wind can make the front unstable due to symmetric instability (SI). The frontogenetic strain and vertical mixing drive an ageostrophic secondary circulation (ASC). Submesoscale eddies develop through mixed layer instability (MLI), which drives further frontogenesis and localizes boundary layer turbulence and subduction of water into the thermocline. Modified from Gula et al. (2022).

The downfront arrangement is illustrated in the diagram of idealized submesoscale processes in Figure

22, where the vector of the wind stress is parallel to the x-axis and points in the same direction as the positive x-axis, which is aligned with the direction of the mean jet associated with the submesoscale front.

To generate a downfront wind arrangement in the numerical experiment, we use the following mathematical expression for the wind stress forcing:

$$\vec{\tau}(x,y) = \tau_0\left(\frac{1}{2}\right)\left(\tanh\left(\frac{y+140-\frac{L_y}{2}}{25}\right) - \tanh\left(\frac{y-140-\frac{L_y}{2}}{25}\right)\right)\hat{\mathbf{i}},$$

where L_y is the channel width. The cross-channel profile of the zonal wind stress, with a channel width of $L_y = 420$ km and a magnitude of $\tau_0 = 0.02, \mathrm{N/m}^2$, is illustrated in Figure 23.a. In the central section of the channel, where the wind stress remains constant (approximately between -50 and 50 km), submesoscale activity develops. Toward the extremes of the channel, the wind stress gradually decreases to zero. This gradual decay along the y-axis results in relatively low vertical motions due to the Ekman pumping effect, with the maximum downward and upward motions of approximately 0.4m/day (Figure 23.b). These slow vertical motions at the channel extremes ensure that any motion noise generated near the y-axis boundaries does not intrude into the submesoscale activity region for up to 10 days.

5.2.2.2 Buoyancy flux due to the Ekman flow

The wind-driven buoyancy flux due to Ekman flow can destabilize the flow, leading to convection and turbulent mixing of buoyancy at the front; this destabilization is maximized in the downfront wind conditions (Thomas et al., 2008; Barkan et al., 2017). The buoyancy flux can be estimated via the following expression:

$$B_{wind} = \mathbf{U_E} \cdot \boldsymbol{\nabla_h} \mathbf{b}|_{\mathbf{z=0}}, \tag{51}$$

where $\mathbf{U}_E$ represents the Ekman transport is defined as:

$$\mathbf{U_E} = -\frac{1}{\rho_0(f+\zeta)}(\hat{\mathbf{k}} \times \vec{\boldsymbol{\tau}}). \tag{52}$$

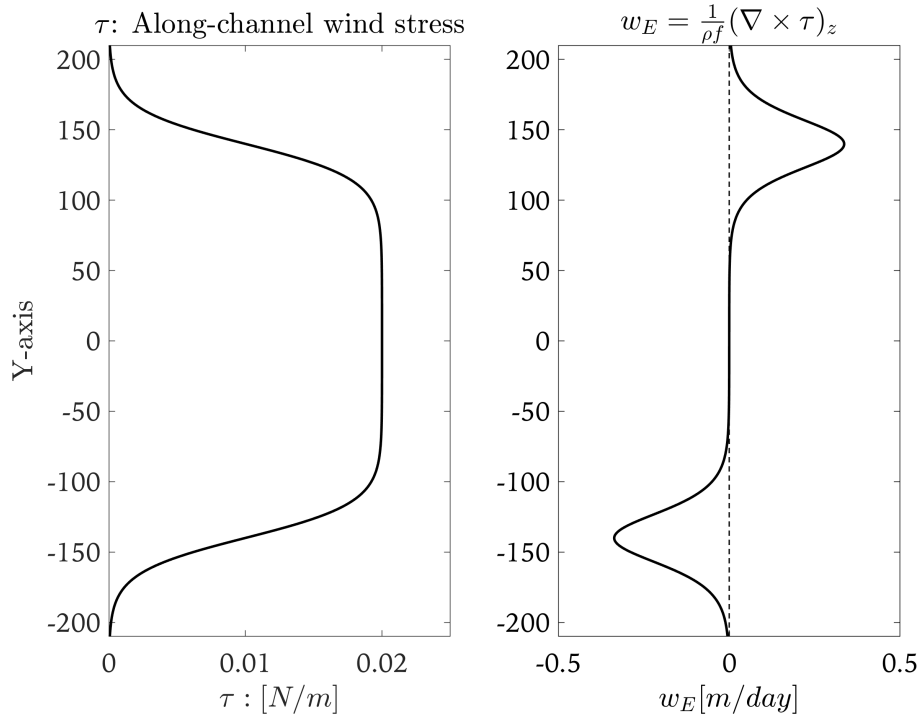

Figure 23. y-axis profile of the wind stress (a) and Ekman pumping (b).

5.3 Results

5.3.1 System state on day 20

In this section, we present the dynamic conditions on the 20^{th}day of the simulation, which serves as the initial state for both the free-evolving and the wind-forced experiments. Our aim is to demonstrate that the system operates within a submesoscale regime characterized by active frontogenesis and pronounced instabilities within the mixed layer. Frontogenesis activity highlights the presence of intense horizontal gradients, whereas the analysis of q reveals that the mixed layer is an inherently unstable environment. This provides a crucial foundation for understanding the evolution of vertical motions and heat fluxes in subsequent stages of the experiments.

5.3.1.1 Rossby number

Figure 24.b shows the Rossby number (R_o) map at the surface. It shows various submesoscale structures, including cyclonic (positive R_o) and anticyclonic (negative R_o) eddies, as well as filaments with R_o near 1. The R_o values indicate that the flows within the reentrant channel are dominated by submesoscale motions (Thomas et al., 2008; McWilliams, 2017; Klein et al., 2019). The three-dimensional view in Figure 24.a further demonstrates that these submesoscale structures are mostly confined to the mixed layer. However, certain features, such as the anticyclonic eddies, can penetrate below the mixed layer, as suggested by the horizontal contours at a depth of 150 meters.

The development of submesoscale structures is driven by baroclinic instability, which is linked to the horizontal meandering of the front and the formation of filaments and eddies (Wang, 1993). The wavelength of the most unstable mode (∼60 km) is highlighted by the buoyancy isolines (green contours in Figure 24).

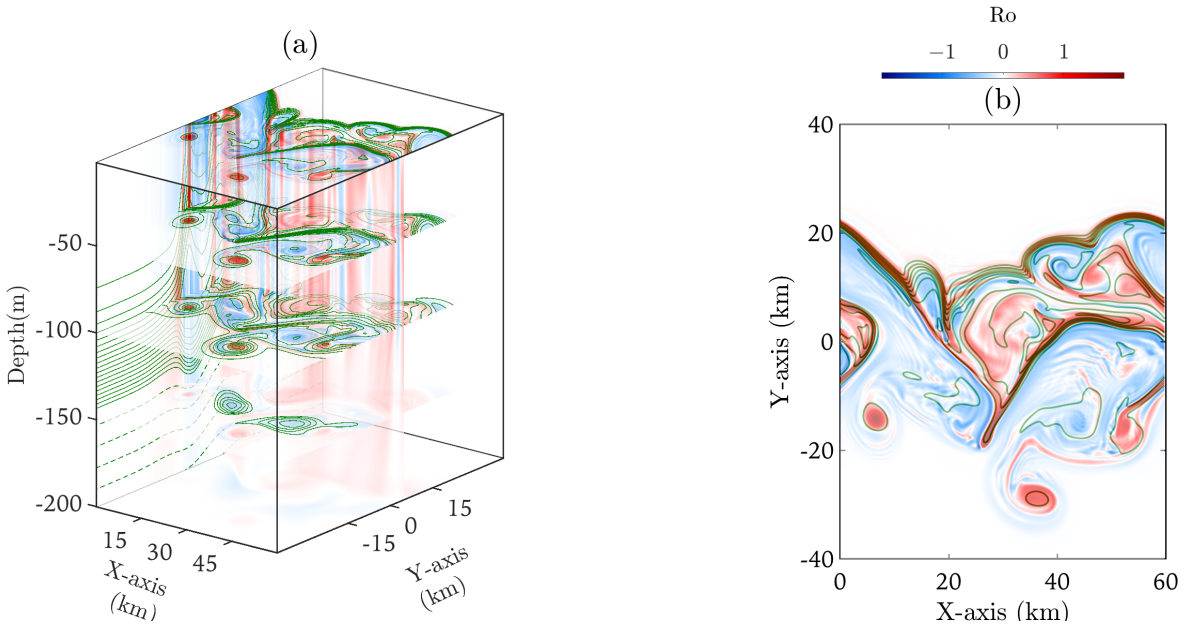

Figure 24. Snapshot of the Rossby number in a the three-dimensional view (a) and a surface map (b) on the 20^{th} day of the simulation. The green contours in panels (a) and (b) represent buoyancy isolines, with contour intervals of 1×10^{-4} ms^{-2} for the horizontal map and 5×10^{-4} ms^{-2} for the vertical sections.

Figure 25 presents the distribution of the normalized probability density of the R_o across different depths. Vertically, three distinct ranges are identified, corresponding to three different regimes of frontogenesis activity (Thomas et al., 2008).

From the surface to approximately 70 m (mixed layer), the distribution of the R_o shows positive asymmetry, with a maximum R_o value of approximately 2 at the surface and decreasing values to 1 at 70 approximately 70 m. The maximum negative R_o value at the surface is close to -1.5, and the values decrease to approximately -1 at 70 m. This positive asymmetry at the surface is consistent with previous submesoscale observations (Buckingham et al., 2016; Shcherbina et al., 2013).

The positive asymmetry observed in R_o can be attributed to the top part ageostrophic secondary circulation induced by frontal activity (Thomas et al., 2008; McWilliams, 2017). As illustrated in the schematic of the ageostrophic secondary circulation (Figure 26), the convergence of buoyancy isolines is asymmetric, leading to an asymmetric gradient in the cross-front zonal velocity, with cyclonic values being more intense than anticyclonic values.

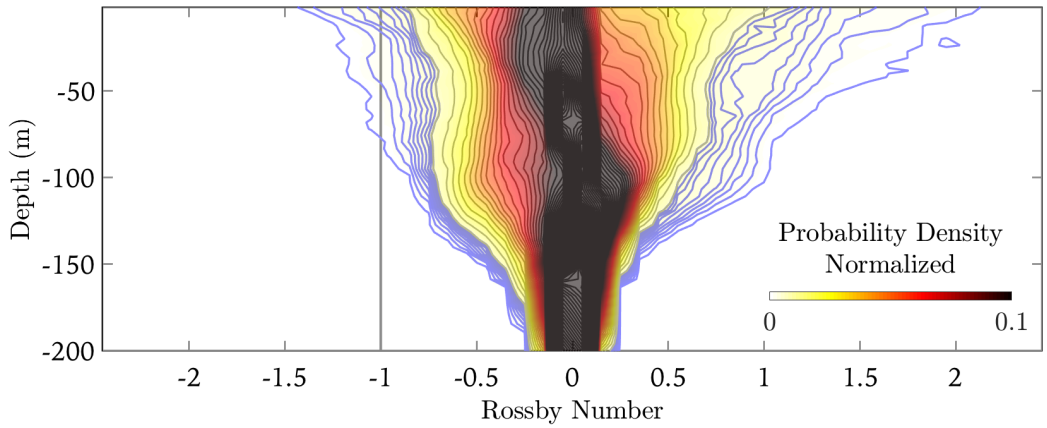

Figure 25. Vertical profile of the normalized probability density function of the Rossby number. Different contour colors indicate distinct intervals; gray contours represent values greater than those in blue by a factor of five.

Between 70 and 120 m (Figure 25), the distribution of R_o exhibits a negative asymmetry. This can be attributed to the lower portion of the ageostrophic secondary circulation (see Figure 26). In contrast to the upper part, the asymmetry in the convergence of buoyancy isolines leads to an asymmetric gradient in the cross-front zonal velocity, with anticyclonic values being more intense than cyclonic ones.

Below 120 m, symmetry between positive and negative values is observed, suggesting that the influence of secondary circulation from submesoscale frontogenesis decreases with depth. This pattern aligns with the experimental setup, where submesoscale motions are primarily confined to the mixed layer.

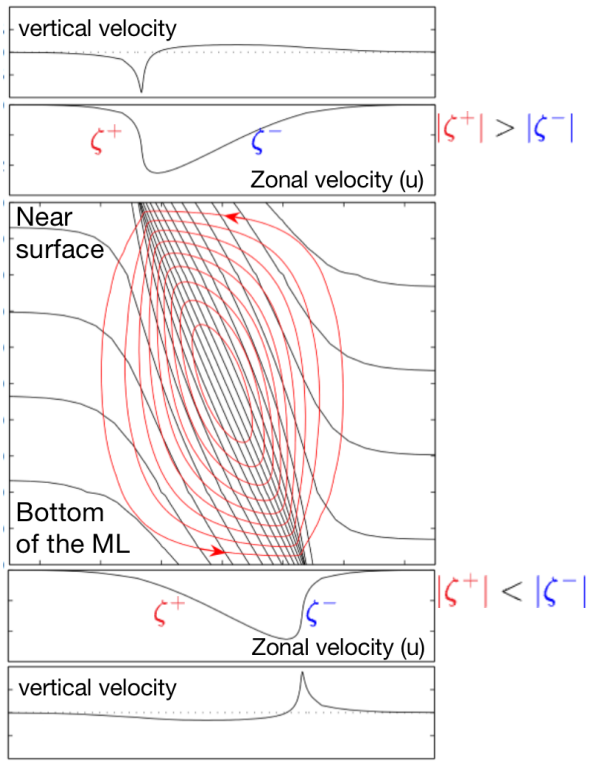

Figure 26. Schematic of secondary circulation (overturning circulation shown by red contours) during frontogenesis, with buoyancy contours in black, adapted from Thomas et al. (2008). Near the surface, cross-front variations in zonal velocity indicate that cyclonic relative vorticity is more intense than anticyclonic vorticity. Conversely, at the base of the mixed layer (ML), cyclonic vorticity is weaker than anticyclonic vorticity. Vertical velocity is strongest in regions of high isoline concentration, displaying downward motion near the surface and upward motion at the base of the mixed layer.

On the other hand, the histogram of the R_o reveals the presence of inertial instabilities in the mixed layer. A value of R_o less than -1 indicates inertial instabilities, which occur when $\frac{f+\zeta}{f} = 1 + R_o$ is negative (Thomas, 2012). These instabilities are confined to the mixed layer, with a greater occurrence near the surface and gradually diminishing toward the base of the mixed layer.

5.3.1.2 Frontogenetical tendency

The frontogenetical tendency, F_s, is presented in the same arrangement as the Rossby number, where positive values indicate regions of frontogenesis (strengthening of fronts) and negative values represent frontolysis (weakening of fronts). F_s maps in plan-view at the surface and in three-dimensional view are provided in Figure 27. In the surface map, F_s is particularly intense (corresponding to areas with tightly spaced buoyancy isolines) in regions where the Rossby number is high (near 1, Figure 24). The

three-dimensional plot shows that F_s extends throughout the mixed layer but is confined to this layer. Within the mixed layer, there is a notable competition between frontogenesis and frontolysis, which is visible by the vertical extension filaments with positive and negative values in the mixed layer.

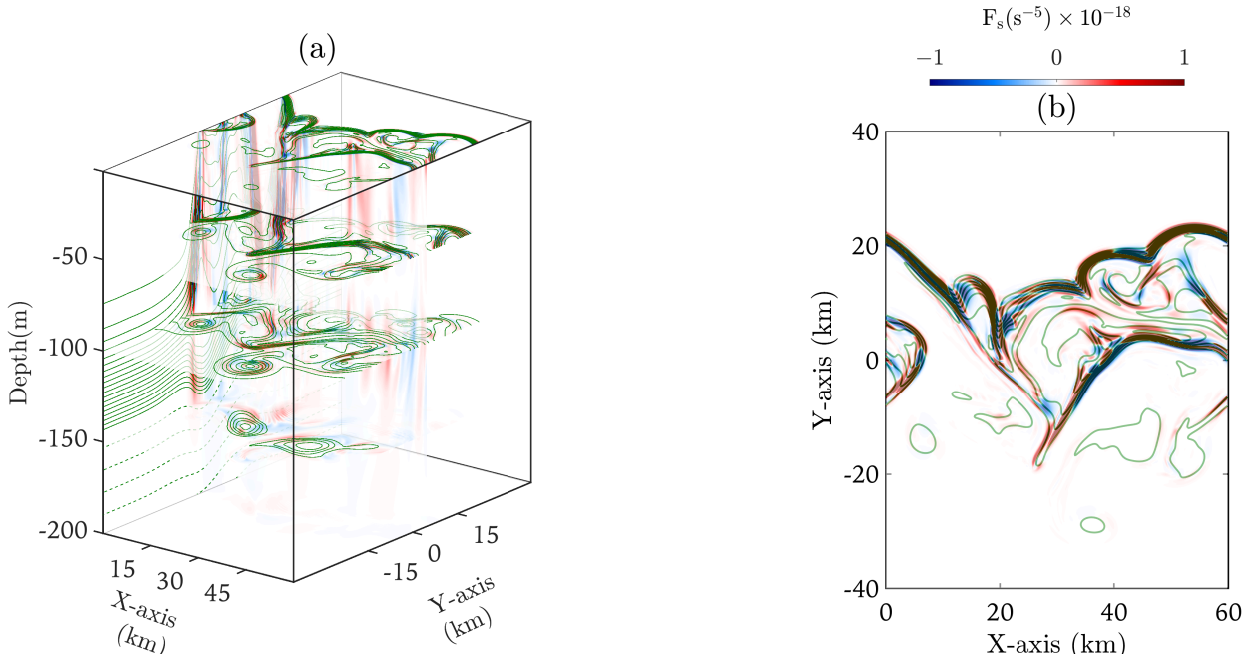

Figure 27. Snapshot of the frontogenesis tendency pattern in a three-dimensional view (a) and at the surface map (b) on the 20th day of the simulation. The green contours in panels (a) and (b) represent buoyancy isolines, with contour intervals of 1×10^{-4} ms^{-2} for the horizontal map and 5×10^{-4} ms^{-2} for the vertical sections.

5.3.1.3 Potential vorticity

The frontogenetical tendency within the mixed layer enhances stratification through the ageostrophic secondary circulation (Fox-Kemper et al., 2008). An indirect way to observe this effect is by analyzing the q. Figure 28.c shows a plan-view map of q, where high positive values are concentrated with regions of strong frontogenesis and high Rossby numbers. These high q values extend from the interior to the surface (Figure 28.a), highlighting the relationship between frontogenesis and stratification.

The vertical profile of the horizontally averaged q (Figure 28.b) is consistent with the stratification observed in the simulation: weak within the mixed layer, where the q is close to zero, and strong below the mixed layer, where the q exhibits high positive values. The vertical profile of the normalized sum of negative q values indicates that instability conditions are concentrated within the mixed layer, with a maximum near the surface and a gradual decrease with depth (blue line in Figure 28.b). This pattern

underscores that overturning instabilities are most active near the surface, whereas stability strengthens below the mixed layer.

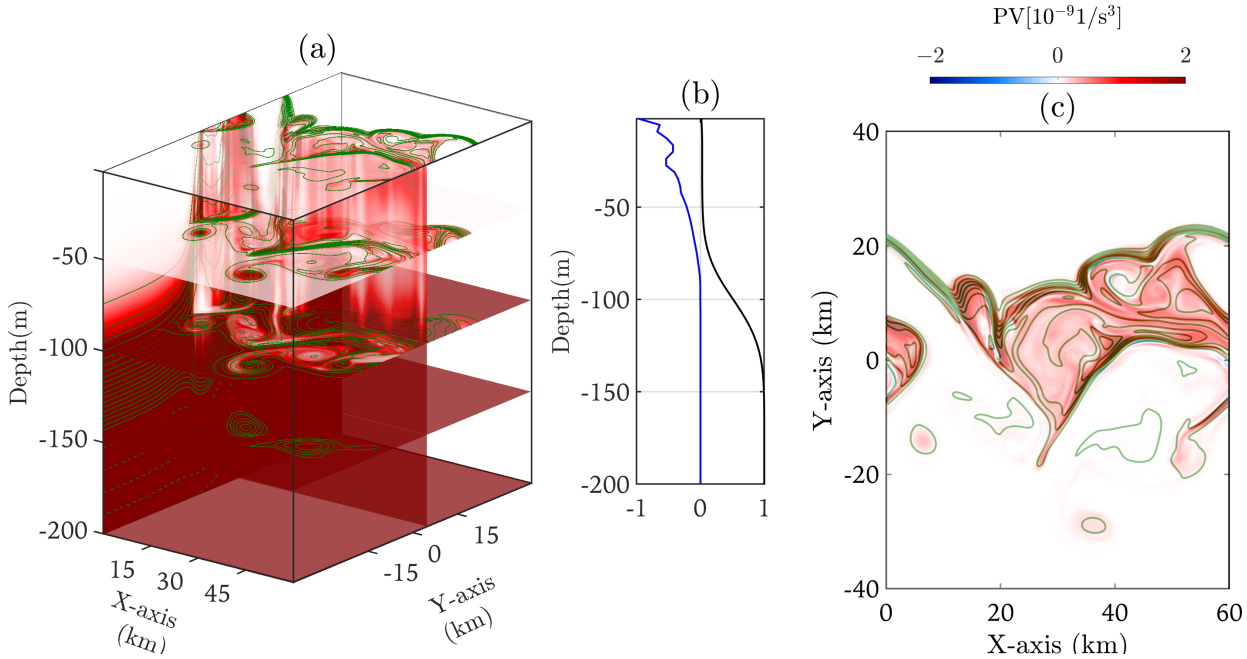

Figure 28. Snapshot of potential vorticity in a three-dimensional view (a) and a plan-view map at the surface (c) on the 20th day of the simulation. The green contours in panels (a) and (c) represent buoyancy isolines, with contour intervals of 1×10^{-4} ms^{-2} for the horizontal maps and 5×10^{-4} ms^{-2} for the vertical sections. Panel (b) shows the vertical profile of the normalized sum of potential vorticity (black line) and the negative values of potential vorticity (blue line).

5.3.2 Temporal evolution of the simulation

This section focuses on the temporal evolution of the submesoscale front simulations between days 20 and 30 under two experimental conditions: one featuring free evolution (unforced) and the other one subjected to wind forcing (forced). By comparing these two scenarios, we examine how external wind forcing impacts the frontogenesis, q, and VHF over time.

Figures 29, 30, 31 and 32 display time axes ranging from 0 to 10 days; however, the data correspond to the period from the 20th to the 30th day of the simulation.

Frontogenesis in the mixed layer is linked to ageostrophic secondary circulation, which promotes restratification. On the other hand, in regions of weak stratification (where the vertical buoyancy gradient is near zero), overturning instabilities can arise when the q becomes negative, leading to enhanced vertical mixing (Thomas et al., 2008). To capture these interactions, we examine the temporal evolution of the

F_s, the occurrence of negative q values, and the vertical buoyancy gradient (b_z), in both the unforced and the wind-forced simulations.

5.3.2.1 Frontogenesis and vertical motion

In the unforced case, the evolution of F_s over time features positive values, indicating active frontogenesis throughout the 10 days of simulation. This activity is mainly confined to the upper ~ 10 m (purple contour in Figure 29.a). Over time, both the intensity and the depth of the high positive F_s values decrease. As frontogenesis is closely tied to vertical motion, a reduction in frontogenesis leads to a decrease in vertical motion (Figure 30.a).

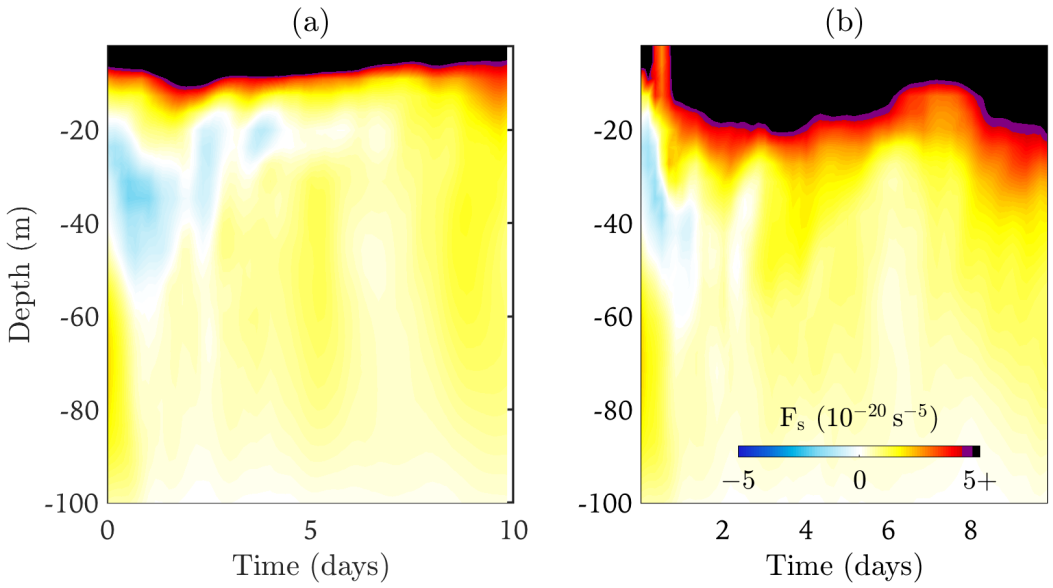

Figure 29. Temporal evolution of the vertical profile of the horizontally averaged frontogenesis tendency (F_s) in the unforced (a) and wind-forced (b) simulations. Averaging is performed across the entire x-axis and within the y-axis range from -60 km to 60 km at each depth.

In contrast, the forced experiment exhibits enhanced frontogenesis, with its effects extending to greater depths than in the unforced case up to approximately 20 meters, occasionally reaching around 30 meters (see the purple contour in Figure 29.b). This intensification is reflected in the vertical motions, which attain magnitudes twice those observed in the unforced scenario. The periods of peak frontogenesis, with effects reaching depths of approximately 30 meters, coincide with the strongest vertical motions (Figure 30.b). From days 6 to 8, frontogenesis decreases in both intensity and depth, leading to a

reduction in vertical motion during these days (Figure 30). These results highlight the direct relationship between frontogenesis and vertical motion within the mixed layer and illustrate how down-front wind forcing modulates this relationship.

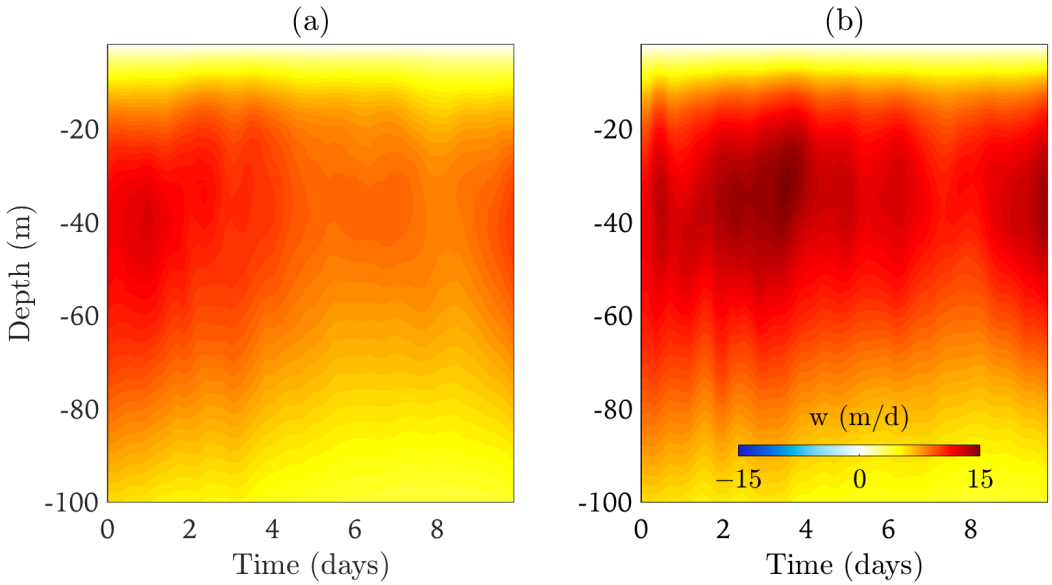

Figure 30. Temporal evolution of the vertical profile of the horizontal standard deviation of the vertical velocity in the unforced (a) and wind-forced (b) simulations. Averaging is performed across the entire x-axis and within the y-axis range from -60 km to 60 km at each depth.

5.3.2.2 Potential vorticity

As discussed earlier, the weak stratification within the mixed layer results in an average q close to zero. During submesoscale activity, the mixed layer becomes a conducive environment for the development of negative q values, which are necessary (but not sufficient) indicators of overturning instabilities that enhance mixing (Thomas et al., 2008; Thomas, 2012).

In the unforced case, the temporal evolution of accumulated negative q values shows that conditions favorable for mixing persist throughout most of the 10 simulation days (Figure 31.a). The negative q values remains confined to the mixed layer, reaching a depth of approximately 40 m by the initial day, but gradually shoals over time, eventually remaining close to the surface. Between days 4 and 6, there is a temporary resurgence of negative q values near the surface; however, this resurgence dissipates in the final two days. Overall, the reduction in negative q values is linked to the restratification driven by ageostrophic secondary circulation, which introduces positive q into the mixed layer.

In the forced case, the presence of a surface-driven source of unstable flow, induced by wind stress (Thomas et al., 2008; Barkan et al., 2017), enhances the occurrence of negative q values in the mixed layer. Initially confined to the surface, negative q values tend to penetrate to greater depths, reaching approximately 30 m by the 2^{nd}day of the simulation (purple contour in Figure 31.b). Afterward, the depth of penetration stabilizes, and this depth is maintained for the remainder of the simulation. This relationship between the surface-injected negative q and deeper positive q, advected upward from below the mixed layer, leads to restratification. As a result, the positive q from below counteracts some of the mixing effects associated with the negative q, regulating the vertical structure of stratification in the wind-forced case.

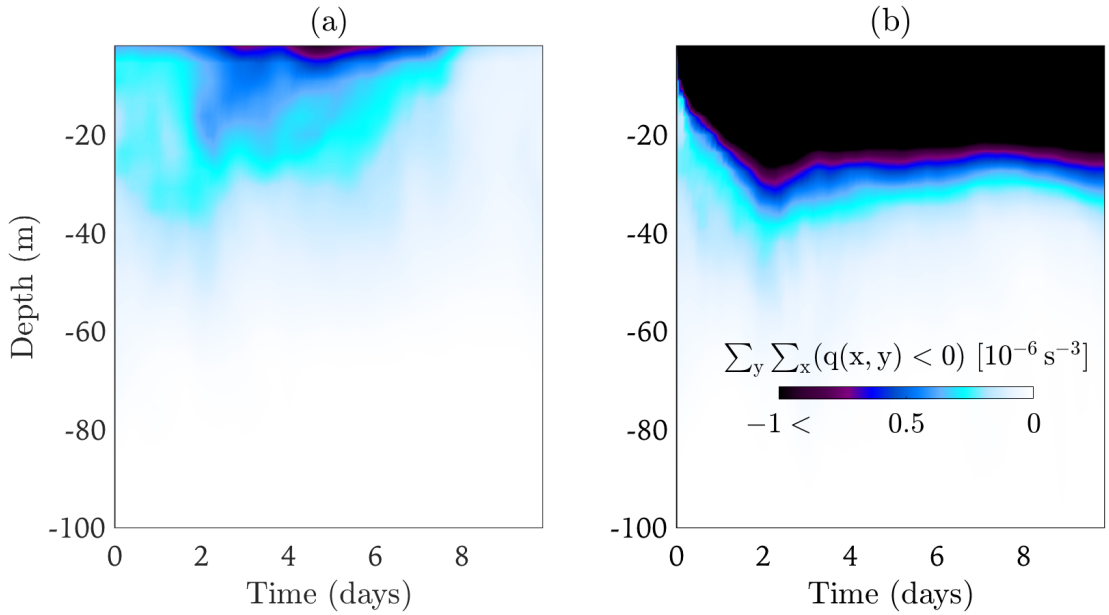

Figure 31. Similar to Figure 32, but depicting the temporal evolution of the accumulated negative potential vorticity in the mixed layer in the unforced (a) and wind-forced (b) simulations.

5.3.2.3 Restratification and mixing

Submesoscale front activity in the mixed layer is a process that promotes both restratification through the ageostrophic secondary circulation and mixing due to instabilities in the mixed layer, which can occur simultaneously (Fox-Kemper et al., 2008). Figure 32 shows the temporal evolution of restratification, represented by the b_z, for both the unforced and forced experiments. High positive values indicate strong stratification, low positive values indicate weak stratification, and negative values, including values near zero, indicate unstable flow.

In the unforced case, the purple contour in Figure 32.a delineates the boundary between strong and weak stratification, which coincides with the bottom of the mixed layer. This boundary decreases in depth from approximately 60 m at the beginning to approximately 45 m after 10 days. The white contour, which gradually decreases in depth over time, suggests that restratification becomes more dominant as the mixed layer shoals, which is consistent with previous research (Aparco-Lara et al., 2023; Fox-Kemper et al., 2008).

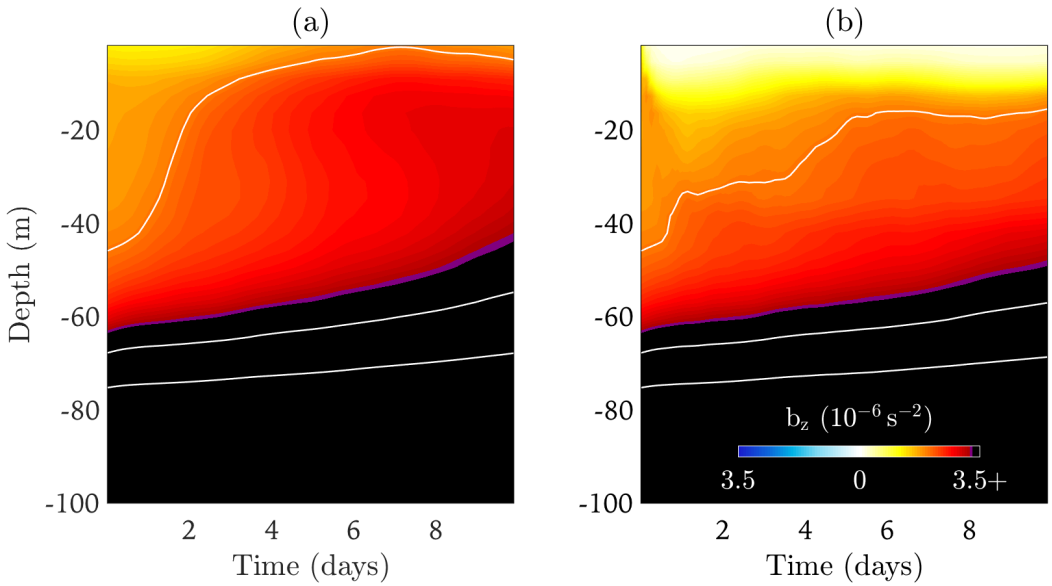

Figure 32. Temporal evolution of the horizontally averaged vertical buoyancy gradient (b_z) within the mixed layer in the unforced (a) and wind-forced (b) simulations. Horizontal averaging was performed over the y-axis range from -60 km to 60 km and across the entire x-axis.

In the forced case, the bottom of the mixed layer shoals slower, stabilizing at a depth of approximately 55 m after 10 simulation days (Figure 32.b). This deeper mixed layer in the forced scenario results from wind-driven mixing, which enhanced by overturning instabilities (Thomas, 2012). Two distinct layers are observed: a surface layer extending to 15 m with weak or near-zero stratification due to the dominant of mixing, and a deeper layer in which stratification increases over time. The white contour shows a gradual shoaling trend, indicating that the deeper stratification becomes more prominent over time. While restratification dominates the mixed layer, wind-induced mixing moderates the shoaling effect. These findings align with those of Barkan et al. (2017) and Thomas et al. (2008), who also noted the effects of wind on upper ocean dynamics.

5.3.3 Vertical heat flux

The advective component of the VHF can be derived from the heat equation and is influenced by w and θ_a (see section 3.5). In submesoscale fronts, vertical motions are largely driven by ageostrophic secondary circulations in the mixed layer. These circulations occur in regions with strong thermal gradients (i.e., fronts), where the covariance between the vertical velocity and horizontal temperature anomalies tends to be positive, enhancing the upward VHF into the mixed layer.

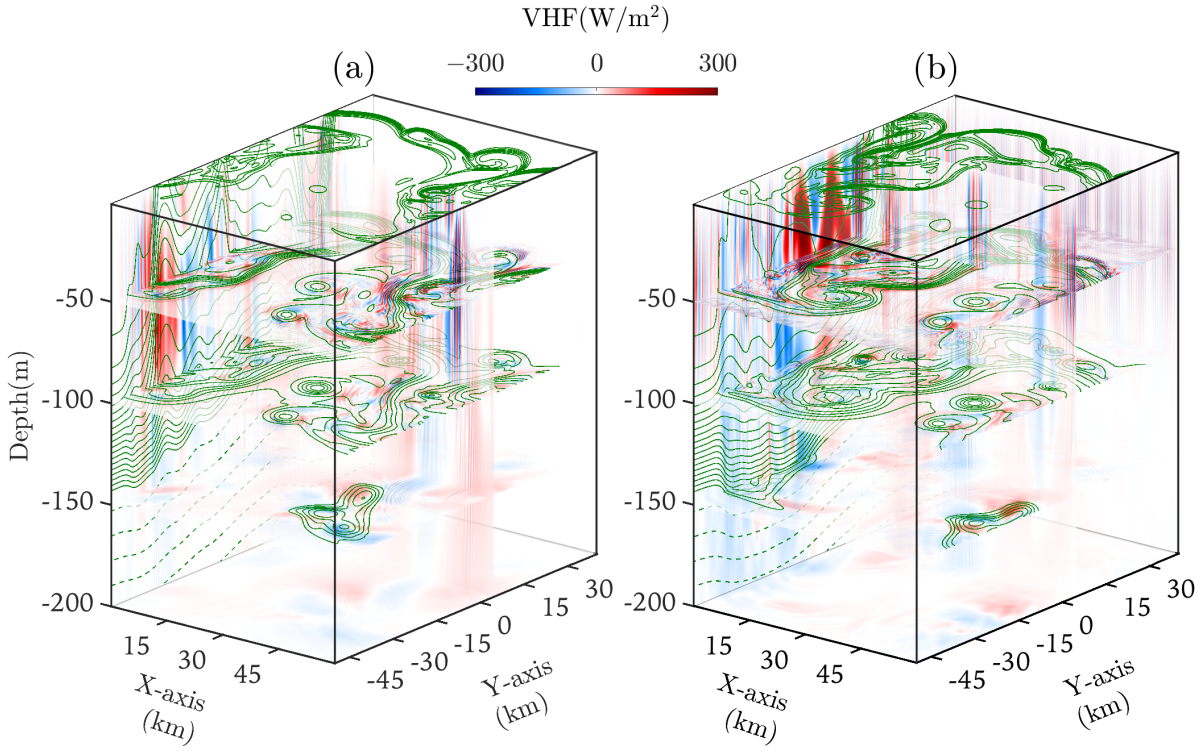

Figure 33. Temporal evolution of the horizontally averaged vertical buoyancy gradient (b_z) in the mixed layer in the unforced (a) and wind-forced (b) simulations. The horizontal averaging is performed over the y-axis range from -60 km to 60 km and across the entire x-axis.

Figure 33 shows the three-dimensional VHF distribution within the mixed layer, presenting a snapshot after 10 simulation days. The surface velocity is near zero, leading to near-zero VHF at the surface. Red colors indicate upward VHF, whereas blue colors represents downward VHF. The VHF is strongest in regions where the buoyancy isolines (green contours) are stacked, corresponding to the locations of fronts.

A comparison between the unforced and forced cases reveals that the forced case exhibits more small-scale structures and higher horizontal VHF intensities. In the forced case, wind stress induces weak

vertical fluxes outside the submesoscale structures, occurring in both negative and positive temperature anomalies, with an average of zero. The vertical cross-sections in the figure highlight the impact on the mixed layer depth: the forced case features greater depths than the unforced case, as noted by the change from solid to dashed contour lines.

5.3.4 Vertical heat flux co-spectrum

We follow the methodology outlined by Su et al. (2020) to compute the VHF co-spectrum. This co-spectrum captures the relationship between the w and θ_a, which is essential for understanding the VHF. The analysis is conducted using the last 10 simulation days, with the horizontal domain extending 60 km along the x-axis and from -60 km to 60 km along the y-axis. Horizontal slices at 38 m depth are used, as the variability in vertical motions is the most intense at this depth (Figure 30). By examining the VHF in the spectral domain, we can evaluate how wind stress influences the VHF across both high-frequency (HF) and small-scale ranges.

Figure 34 shows the co-spectrum for both the unforced and forced experiments at a depth of 38 m, where the strongest vertical motions occur. The critical length scale, L_s, and the 1 day^{-1} frequency, which divides the HF and LF regimes, are also highlighted. Positive values in both experiments indicate upward heat transport. The VHF values span a continuous range of frequencies, encompassing both the LF and HF domains. In the unforced case, the upward flux reaches a frequency of approximately $1/15$ h^{-1}, whereas in the forced case, it reaches $1/10$ h^{-1}. In both cases, the low-frequency limit of the VHF is on the order of days. The upward flux is stronger in the forced experiment than in the unforced experiment.

In terms of scale in both the unforced and forced cases, the VHF exhibits a sign change near L_s, transitioning from positive to negative values. Positive VHF values occur at wavelengths larger than L_s, whereas negative VHF values are observed at wavelengths smaller than L_s. The contours of the vertical velocity spectrum indicate that negative VHF values are associated with regions of intense vertical motion, particularly in a spectral range dominated by convective motions. In the forced experiment, these convective motions are enhanced, explaining why the increase in the vertical velocity spectrum is more pronounced than in the unforced case.

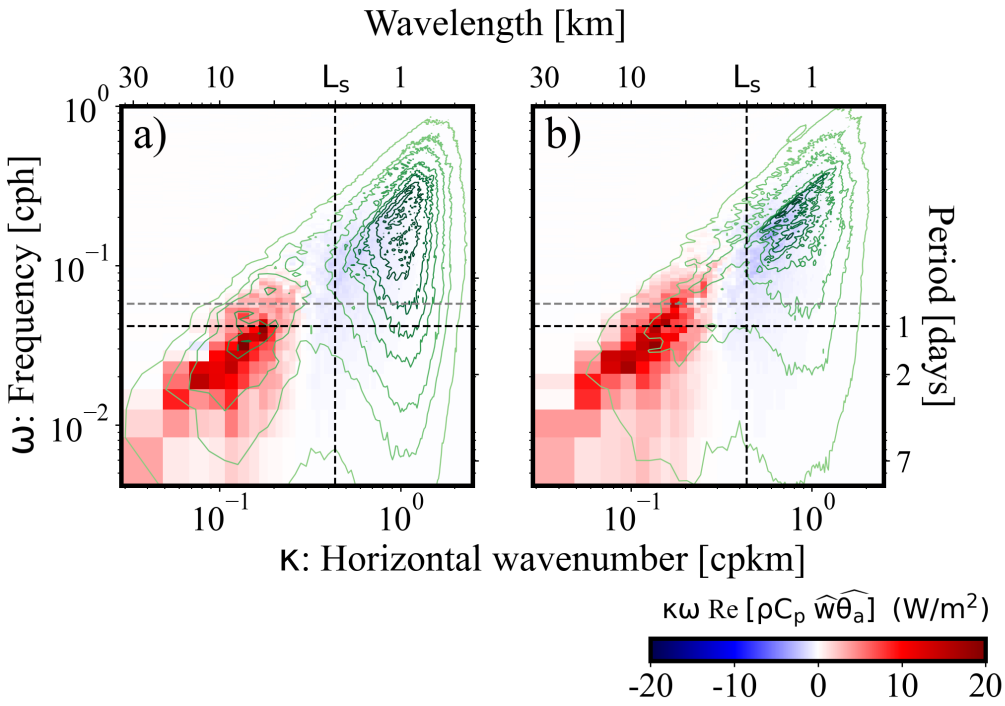

Figure 34. co-spectra of the vertical heat flux for the unforced (a) and forced (b) experiments. The horizontal black dashed lines indicate the low-frequency boundary (> 1 day^{-1}) and high-frequency boundary (< 1 day^{-1}), while the horizontal gray dashed line represents the inertial frequency (f). On the basis of the initial conditions, the vertical black dashed line represents Stone's fastest-growing length scale ($L_s = 2.3$ km). Contours display the vertical velocity spectrum, where dark colors correspond to high variability and light colors correspond to low variability. The co-spectra density (Re[$\rho C_p \widehat{w}\widehat{\theta_a}$], units: Wm^{-2} cph^{-1} cpkm^{-1}) is presented in a variance-preserving format. The co-spectra are multiplied by the wavenumber (κ) and frequency (ω) to account for the logarithmic scaling on both axes. All calculations were performed at a depth of 38 m.

To identify more features between both the unforced and forced experiments, we integrated the corresponding VHF co-spectra in terms of frequency (Figure 35.a) and wavenumber (Figure 35.b).

Over the wavenumber range where the VHF is positive (Figure 35.a), both the unforced and forced experiments yield peak values near a wavelength of 8 km, with values of approximately $120\,W/m^2$ in the forced case and $100\,W/m^2$ in the unforced case.

The VHF in the forced case exceeds that in the unforced case across the entire wavenumber range, indicating an enhanced secondary circulation driving the upward heat flux.

In contrast, in the wavenumber range where the VHF is negative, the forced case results in more negative values than the unforced case. This result aligns with the generation of unstable conditions that drive overturning instabilities, as previously observed. The wavelength at which the transition from positive to negative VHF occurs suggests that the mixed layer at 38 m is more homogeneous in the forced case

than in the unforced case (see the large green line to the forced case and the small green line in the unforced case in Figure 35.a). However, these wavelengths are greater than L_s in both cases, indicating that restratification remains dominant.

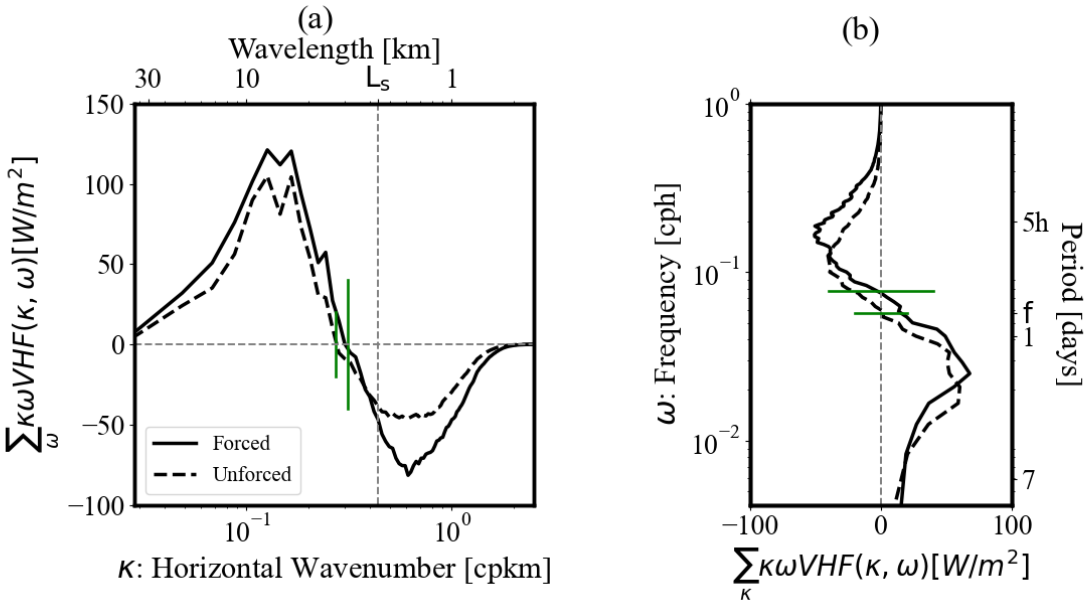

Figure 35. Wavenumber spectrum of the frequency-integrated vertical heat flux co-spectrum (a) and the frequency spectrum of the wavenumber-integrated vertical heat flux co-spectrum (b) in both the forced and unforced cases, obtained from Figure 34. The vertical dashed line in panel (a) represents Stone's fastest-growing length scale ($L_s = 2.3$ km) on the basis initial conditions. The large and small vertical green lines indicate wavelengths of 2.7 km and 3 km, respectively. In panel (b), the large and small horizontal green lines represent frequencies of $(10\ \text{h})^{-1}$ and the Coriolis frequency (f), respectively. In both panels, the solid black line corresponds to the forced case, and the dashed black line corresponds to the unforced case.

In terms of frequency (Figure 35.b), the positive VHF in the wind-forced case reaches higher frequencies that in the unforced case with values near f in the unforced scenario and approximately $1/10\ \text{h}^{-1}$ in the forced case. As shown in Figure 34, the positive VHF within this frequency range in both cases is associated with ageostrophic secondary circulation driven by submesoscale frontal activity, with a clear tendency toward higher frequencies in the forced case. Furthermore, the VHF values are more negative at higher frequencies in the forced case than in the unforced case, and this pattern is linked to more favorable conditions for the development of overturning instabilities.

5.3.5 Strong wind forcing

An additional experiment is conducted to analyze the VHF under a wind stress of 0.1 N/m^2, which is five times greater than that in the previous wind-forced experiment. The results, presented in terms of wavenumber and frequency, are shown in Figure 36, where both the unforced case and the stronger wind-forced case are compared. This comparison provides insights into how intensified wind forcing modulates the VHF across different wavenumber and frequency ranges.

Compared with the previous wind-forced case, the positive and negative VHF values are amplified. This amplification in the positive VHF indicates a strengthening of the ageostrophic secondary circulation, and these positive values extend to smaller scales and higher frequencies. This intensification is consistent with the enhancement of the vertical motion spectrum (green contours, where darker green indicates more intense vertical motions). Moreover, the increase in the negative VHF aligns with the intensification of conditions favorable to convective motion related to overturning instabilities.

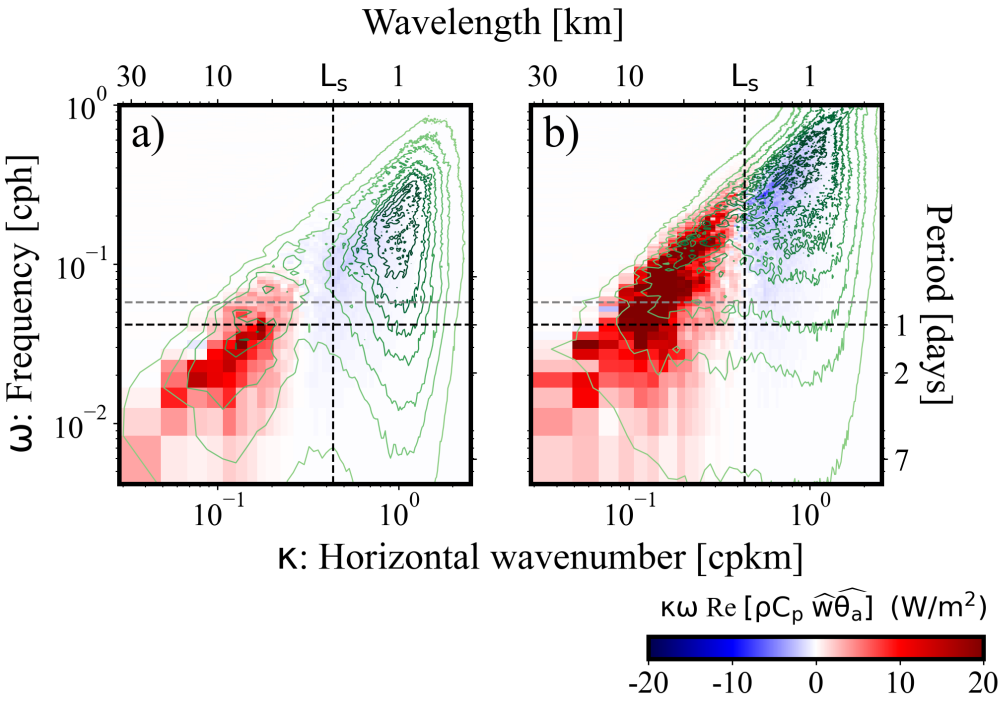

Figure 36. co-spectra for the unforced and wind-forced experiments, similar to that shown in Figure 34, but with a wind stress of 0.1 N/m^2.

The frequency-integrated co-spectrum of the VHF shows a significant intensification (Figure 37.a), with an approximate increase of a factor of 7, and the maximum occurs at a smaller wavelength (7 km).

Moreover, the maximum of the negative VHF values increases by a factor of approximately 4. The transition wavelength from positive to negative values shifts toward smaller scales (green line in Figure 37.a).

The wavenumber-integrated co-spectrum of the VHF also shows a significant intensification at high frequencies (Figure 37.b), reaching frequencies close to $1/5\ h^{-1}$ (indicated by the green line).

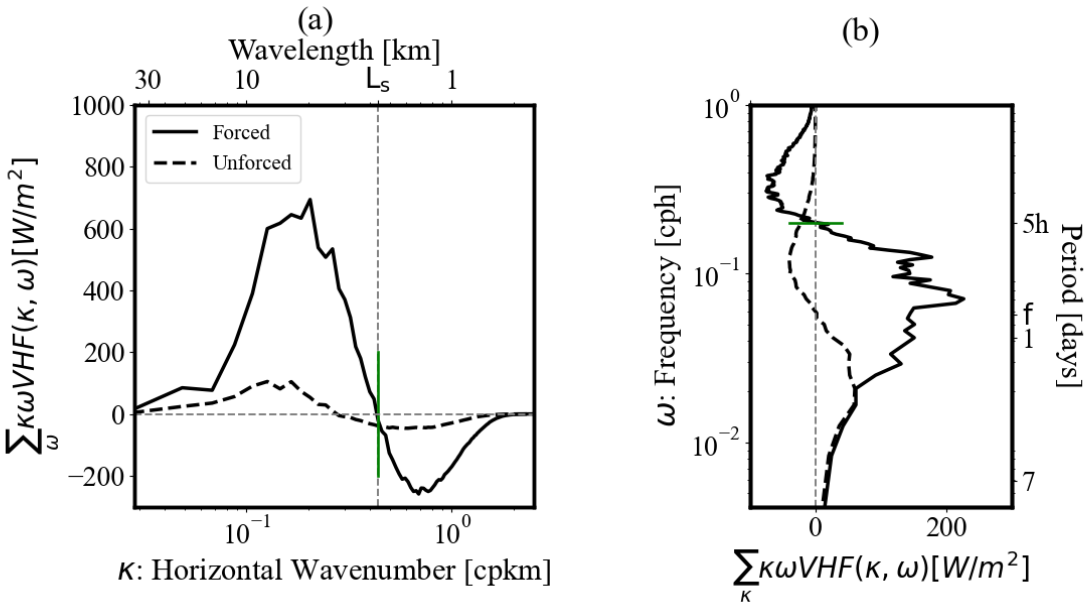

Figure 37. Wavenumber spectrum of the frequency-integrated vertical heat flux co-spectrum (a) and the frequency spectrum of the wavenumber-integrated vertical heat flux co-spectrum (b) in both the forced and unforced cases, obtained from Figure 36. The vertical dashed line in panel (a) represents Stone's fastest-growing length scale ($L_s = 2.3$ km) on the basis initial conditions. The vertical green line indicate wavelengths of 2.3 km, respectively. In panel (b), the horizontal green line represent frequencies of $(5\ \text{h})^{-1}$. In both panels, the solid black line corresponds to the forced case, and the dashed black line corresponds to the unforced case.

5.3.6 Conclusions

The variability of submesoscale VHF in the mixed layer under the influence of downfront wind stress using idealized numerical simulations of the submesoscale front is examined.

The comparison between unforced and wind-forced simulations demonstrates that wind forcing markedly amplifies frontogenesis and vertical motions within the mixed layer, thereby underscoring its critical role in driving submesoscale dynamics. Wind forcing sustains deeper mixing and enhances overturning instabilities through an increased prevalence of negative q, emphasizing the importance of atmospheric

forcing in modulating submesoscale processes. The simulations reveal that wind forcing significantly amplifies the VHF, particularly in regions characterized by strong thermal gradients, leading to elevated VHF values and deeper penetration of fluxes in the wind-forced scenario than in the unforced scenario. The complex interaction between wind forcing and submesoscale dynamics underscores the critical role of wind-induced processes in regulating heat exchange within the upper ocean, with significant implications for ocean-atmosphere interactions and the overall global heat balance.

The co-spectrum results reveal a significant influence of wind stress on VHF across both the HF and LF domains. The upward heat transport in the wind-forced scenario is notably greater than that in the unforced case, indicating that stronger wind forcing leads to more pronounced vertical motions associated with ageostrophic secondary circulation, thereby increasing restratification and enhancing mixing through overturning instabilities. The analysis conducted at a depth of 38 m illustrates the transition of VHFs from positive to negative values near the L_s, underscoring the complex dynamics at play. Furthermore, the examination of integrated VHF values across both wavenumber and frequency highlights the substantial impact of wind forcing, with the positive VHF in the wind-forced scenario reaching higher frequencies, approaching $(1/10)\,h^{-1}$, that in the unforced case. The additional experiment with intensified wind stress ($0.1\,\mathrm{N/m^2}$, which is five greater than the previous forced case) demonstrates significant amplification of VHF, extending the positive VHF to the HF range, with values approaching $(1/5)\,h^{-1}$. These findings underscore the critical influence of wind-induced processes in modulating heat exchange within the upper ocean and their implications for understanding ocean-atmosphere interactions.

Chapter 6. General conclusions

6.1 Summary of the numerical experiments employed, advantages, and limitations

In this thesis, the mechanisms driving VHFs in the submesoscale regime of the oceanic mixed layer were studied, focusing specifically on the impact of atmospheric forcings such as diurnal surface cooling and wind stress through high-resolution numerical simulations. These simulations captured the meandering evolution of baroclinic instability in the mixed layer, enabling the formation of submesoscale structures such as fronts, filaments, and eddies.

The model used consisted of a periodic channel aligned with the direction of baroclinic instability evolution, with rigid walls at the boundaries and a flat bottom. The fluid dynamics were solved using the primitive equations of Geophysical Fluid Dynamics under an Eulerian reference framework. Atmospheric forcings were incorporated as boundary conditions using a one-way coupling scheme, where the atmosphere influences the ocean without receiving feedback.

In the experiments related to diurnal surface cooling, two configurations were explored: one in free evolution and another with forcing. The surface cooling was defined with a maximum magnitude of -300 W/m^2 at midnight, decreasing linearly to zero at noon. On the other hand, the effect of "down-front" wind stress was investigated through two additional configurations, also in free evolution and with forcing, initially using a uniform intensity of 0.02 N/m^2. Additionally, an experiment with a stronger wind stress of 0.1 N/m^2 was included to evaluate high-frequency VHFs under more intense conditions.

This design excludes other physical phenomena present in the ocean, such as mesoscale structures, internal waves, tides, surface waves, and bottom currents, ensuring the predominance of the submesoscale regime in the simulated fluid. The absence of these processes creates a controlled environment that facilitates a more precise interpretation of the results by directly relating the impact of atmospheric forcings to submesoscale dynamics. However, the lack of feedback between the ocean and the atmosphere may lead to an overestimation of the results, as the exchange of kinetic and thermal energy at the air-sea interface is not considered. This omission can induce either damping or intensification of currents and fronts in the ocean.

6.2 Findings from the diurnal surface cooling forced experiments

The numerical experiment focused on the free evolution of baroclinic instability was physically consistent with other reported experiments, highlighting the tendency for an increase in kinetic energy as a result of the transformation of potential energy into kinetic energy. This process energizes the meandering behavior of the fluid and leads to the formation of structures characterized by relative vorticity and deformation of the fluid with values on the order of f. This justifies the tendency towards the loss of geostrophic balance in the system, manifested by the divergent activity of the velocity field. Furthermore, the divergence and deformation of the fluid drove, on average, a positive frontogenetic tendency (frontogenesis), promoting the ageostrophic secondary circulation associated with frontogenesis. This resulted in an increase in the restratification of the mixed layer and predominantly upward vertical heat fluxes, consistent with the frontal activity in the mixed layer.

The distribution of kinetic energy in the spectral domain (wave number and frequency) showed that the turbulent activity in the free evolution of baroclinic instability approximates quasi-geostrophic turbulence. This explains the formation of coherent structures, such as well-defined vortices, which tend to increase in size as the simulation progresses. In other words, an inverse energy cascade was observed, where kinetic energy flows toward larger scales. This property of quasi-geostrophic turbulence favors horizontal motions due to the influence of Earth's rotation and the stratification of the mixed layer; consequently, the vertical velocity component is weak. Temporally, quasi-geostrophy suggests a slow evolution of these structures, consistent with the concentration of kinetic energy in low frequencies observed in this experiment, approximately one cycle per day.

The VHFs in the spectral domain revealed that upward fluxes reached a maximum at a wavelength of 8 km and a frequency of one cycle per day (values associated with the most unstable mode of baroclinic instability). These fluxes decreased toward smaller wavelengths (down to 3 km) and higher frequencies (up to $1/10$ h^{-1}), highlighting that upward VHFs are more significant at larger scales. This behavior reflects the nature of energy transfer in the submesoscale regime, where the dynamics of structures around 8 km dominate over smaller ones. These results are indicative of the turbulence developed in the free-evolution experiment.

The results of the evolution of baroclinic instability forced by diurnal surface cooling showed marked differences compared to the unforced case. Surface cooling intensified thermal and baroclinic gradients, strengthened instabilities, and promoted a significant increase in kinetic energy.

As a result, more defined coherent structures with higher kinetic energy were observed, accompanied by a proliferation of smaller structures, according to spectral and statistical analysis, compared to the unforced case. This forcing amplifies all dynamic parameters, intensifying the meandering behavior of the fluid and accentuating flow deformation and curvature (with values up to $3f$), suggesting increased ageostrophic activity.

The distribution of kinetic energy in the spectral domain (wave number and frequency) revealed a shift in the dynamic regime, associated with the surface quasi-geostrophic theory. This regime shift has significant implications, such as the presence of a direct energy cascade, where kinetic energy flows toward smaller scales instead of larger ones, contrasting with the inverse cascade observed in the free-evolution case. This type of turbulence, characteristic of surface quasi-geostrophy, favors vertical motions due to a reduced influence of restoring forces (Earth's rotation and stratification), intensifying vertical movements through energy transfer to smaller scales.

The spectral distribution of upward VHFs showed an amplification with maximum values at wave numbers and frequencies similar to the unforced case (8 km and one cycle per day, associated with the most unstable mode of baroclinic instability). However, it extended toward smaller scales, reaching 2 km (smaller than the convective instability scale, $L_s = 2.3$ km), and higher frequencies, up to $1/6$ h^{-1}. This reflects how surface cooling can induce a shift in the dynamics, transitioning from quasi-geostrophic to surface quasi-geostrophic regimes, which amplifies vertical heat fluxes and shifts them toward smaller scales and higher frequencies.

Additional experiments evaluating the impact of mixing (applying K-profile parameterization) on vertical motions, and consequently on VHFs, during the evolution of baroclinic instability showed that mixing tends to damp vertical motions at frequencies and wave numbers where convective instabilities dominate. This reduces the intensity of VHFs at these scales and frequencies dominated by convection, specifically at scales smaller than L_s and their corresponding frequencies.

6.3 Findings from the wind stress forced experiments

The preliminary results of the numerical experiment with wind stress in a down-front arrangement showed that the interaction between wind stress and thermal fronts reinforces baroclinic instability through two main mechanisms. First, Ekman transport shifts denser water toward the warmer side

of the front, generating vertical destabilization in the mixed layer that creates favorable conditions for convective instabilities. Second, this displacement intensifies density gradients by converging density isolines, promoting a more vigorous frontogenesis process compared to the free-evolution experiment. This, in turn, enhances the secondary circulation of the front, amplifying vertical motions. As a result of this reinforcement of baroclinic instability, a proliferation of smaller submesoscale structures compared to the free-evolution experiment was observed.

Regarding the VHFs, the intensification of thermal gradients, as well as vertical motions in the mixed layer, led to an increase in upward fluxes. Their distribution in the spectral space showed a trend toward higher frequencies and smaller scales. From a frequency of f (wavelength of 3 km) in the unforced case, to a frequency of $1/10$ hr^{-1} (wavelength of 2.7 km) in the forced case. Meanwhile, in the experiment with more intense wind stress (0.1 N/m^2), the average magnitude increased by up to 700%, reaching higher frequencies ($1/5$ hr^{-1}) and smaller scales (2.3 km).

6.4 Similarities and differences between the two forced experiments

Both atmospheric forcings, surface cooling and wind stress, tend to reinforce baroclinic instability activity by energizing submesoscale structures. Both intensify frontogenesis (tend to restratify the mixed layer) and create conditions for the development of convective instabilities (tend to mix), significantly impacting upward vertical heat fluxes and shifting them towards higher frequencies, close to 6 cycles per hour. Although these forcings are of different nature, one thermal and the other mechanical, both contribute to increased variability in vertical heat fluxes with high frequencies. However, they differ in the mechanisms through which they modulate frontogenesis.

Surface cooling reinforces frontogenesis through changes in buoyancy gradients induced by mixing generated by convective instabilities. On the other hand, wind stress intensifies frontogenesis by advection of denser water towards the anomalously warm side of the front, creating favorable conditions for the formation of convective instabilities (a mechanism similar to surface cooling, but with significantly lower values, approximately 100 times less than the 300 W/m^2). Simultaneously, this wind stress causes the stacking of density isolines, intensifying both thermal and dynamic gradients.

The magnitudes of the forcings employed in this study are significantly intense and sustained over several days (on average, 150 W/m^2 for 18 days and 0.1 N/m^2 for 10 days), exceeding both in intensity and

duration the values reported in observational studies. This suggests that the high-frequency variability of VHFs in this study likely represents the maximum impact these forcings can have on the ocean. However, even under these extreme conditions, the forcings only partially replicate the high frequency of VHFs (1 cycle per hour) reported in simulations with more realistic conditions at a resolution of $\sim$2 km.

This suggests the existence of other mechanisms or forcings that could generate these frequencies not reproduced in the numerical experiments conducted. A plausible hypothesis is the interaction between submesoscale frontal systems and the higher modes (between mode 5 and 10) of internal waves, which could contribute to these high frequencies. Furthermore, it is recommended to investigate the effect of the constructive combination of the atmospheric forcings used in this study to assess whether their joint interaction could reproduce this high frequency, which was not observed when applied independently.

6.5 Context of findings with realistic simulations: focused on spatial resolution

The spatial resolution used in the numerical simulations in this study allows for the direct capture of submesoscale processes, in addition to convective instabilities that vertically distribute heat in the ocean's mixed layer. This contrasts with the resolution of more common realistic simulations, where the spatial resolution is typically around 10 km, and for the specific case of the MITgcm with a resolution of approximately 2 km, which partially represents the submesoscale but does not explicitly resolve smaller convective instabilities or the associated VHFs.

In coarse-resolution models ($>$10 km), the effects of the submesoscale are parameterized, which may limit the accurate representation of vertical heat redistribution, especially in terms of the high frequency and small scales observed in our simulations. The results obtained show that vertical upward heat fluxes in the mixed layer not only reach high frequencies (up to $1/5$ h^{-1} under forced conditions) and small scales (down to 2.3 km), but also have a significant magnitude (up to 50 W/m^2 at wavelengths of 8 km, and with a frequency of 1 cycle per day). This behavior suggests that submesoscale processes are crucial in the redistribution of heat, especially in areas of high dynamic activity, such as thermal fronts.

Since convective instabilities directly contribute to vertical mixing, they play a key role in thermal distribution and the formation of density gradients that enhance frontogenesis. This mechanism is poorly represented in coarse-resolution models ($\sim$ 10 km) and partially captured in intermediate-resolution models ($\sim$ 2 km). Therefore, high-resolution simulations, such as ours, are essential not only to study

these processes directly but also to validate and improve the parameterizations used in lower-resolution models.

In a global context, the findings highlight the importance of more accurately including high-frequency and small-scale effects in regional and global simulations, given their impact on submesoscale dynamics and the oceanic energy balance. Integrating this knowledge can improve the representation of the mixed layer in climate models and ocean prediction systems, addressing biases associated with unresolved processes in current realistic models.

6.6 Perspectives of the thesis

This work represents a significant advance in the understanding of submesoscale dynamics by demonstrating how atmospheric forcings, particularly surface cooling and wind stress, notably affect vertical heat fluxes in the oceanic mixed layer. These forcings not only increase variability towards higher frequencies but also intensify the magnitude of the fluxes. This positions high-frequency vertical fluxes as a critical component in the oceanic energy balance and heat redistribution, with important implications for air-sea interaction processes and potential impacts on ocean circulation and global climate patterns.

However, the approach of this study, based on idealized simulations, has inherent limitations by excluding realistic conditions such as the presence of mesoscale structures, tides, surface waves and internal waves. These simplifications may limit the representativeness of the results in more complex natural scenarios. Therefore, a logical extension of this work includes conducting field studies that directly measure VHFs in the mixed layer, especially in regions with strong thermal gradients and under sustained wind stress conditions. These measurements would provide key empirical data to validate and contextualize the findings.

Additionally, the results of this study have a direct connection with the Sub-Mesoscale Ocean Dynamics Experiment (S-MODE), which is currently under development. S-MODE is particularly relevant due to its ability to observe dynamics across multiple scales, from mesoscale phenomena to submesoscale processes influenced by surface forcings such as diurnal heating and cooling. Its ability to capture prolonged events of sustained winds also provides a valuable perspective for investigating the interaction of these conditions with submesoscale dynamics.

The observations provided by S-MODE could corroborate the mechanisms identified in this work, offering

crucial empirical validation and helping to integrate submesoscale effects into broader climate and ocean models. This synergy between idealized simulations, field studies, and missions such as S-MODE is essential for a more comprehensive understanding of how submesoscale processes impact the thermal and energy structure of the ocean, reinforcing their relevance within the framework of global climate systems.

Bibliography

Alistair, A., Jean-Michel, C., Stephanie, D., Constantinos, E., David, F., Gael, F., Baylor, F.-K., Patrick, H., Chris, H., Helen, H., Oliver, J., Martin, L., John, M., Guillaume, M., Dimitris, M., & Andrea, M. (2018). Mitgcm user manual. (online: https://dspace.mit.edu/bitstream/handle/1721.1/117188/mitgcm-manual-r2.pdf?sequence=1).

Aparco-Lara, J., Torres, H. S., & Gomez-Valdes, J. (2023). Impact of atmospheric cooling on the high-frequency submesoscale vertical heat flux. *Journal of Geophysical Research: Oceans*, *128*(9), e2023JC020029. https://doi.org/10.1029/2023JC020029.

Barkan, R., Molemaker, M. J., Srinivasan, K., McWilliams, J. C., & D'Asaro, E. A. (2019). The role of horizontal divergence in submesoscale frontogenesis. *Journal of Physical Oceanography*, *49*(6), 1593–1618. https://doi.org/10.1175/JPO-D-18-0162.1.

Barkan, R., Winters, K. B., & McWilliams, J. C. (2017). Stimulated imbalance and the enhancement of eddy kinetic energy dissipation by internal waves. *Journal of Physical Oceanography*, *47*(1), 181–198. https://doi.org/10.1175/JPO-D-16-0117.1.

Boccaletti, G., Ferrari, R., & Fox-Kemper, B. (2007). Mixed layer instabilities and restratification. *Journal of Physical Oceanography*, *37*(9), 2228–2250. https://doi.org/10.1175/JPO3101.1.

Buckingham, C. E., Naveira Garabato, A. C., Thompson, A. F., Brannigan, L., Lazar, A., Marshall, D. P., George Nurser, A., Damerell, G., Heywood, K. J., & Belcher, S. E. (2016). Seasonality of submesoscale flows in the ocean surface boundary layer. *Geophysical Research Letters*, *43*(5), 2118–2126. https://doi.org/10.1002/2016GL068009.

Callies, J. & Ferrari, R. (2018). Note on the rate of restratification in the baroclinic spindown of fronts. *Journal of Physical Oceanography*, *48*(7), 1543–1553. https://doi.org/10.1175/JPO-D-17-0175.1.

Capet, X., Klein, P., Hua, B., Lapeyre, G., & McWilliams, J. (2008). Surface kinetic and potential energy transfer in sqg dynamics. *J. Fluid Mech*, *604*, 165–174. https://doi.org/10.1017/S0022112008001110.

Cushman-Roisin, B. & Beckers, J.-M. (2011). *Introduction to geophysical fluid dynamics: physical and numerical aspects*. Academic press. (online: https://www.sciencedirect.com/bookseries/international-geophysics/vol/101/suppl/C).

Eady, E. T. (1949). Long waves and cyclone waves. *Tellus*, *1*(3), 33–52. https://doi.org/10.3402/tellusa.v1i3.8507.

Farrar, J. T., D'Asaro, E., Rodriguez, E., Shcherbina, A., Czech, E., Matthias, P., Nicholas, S., Bingham, F., Mahedevan, A., Omand, M., et al. (2020). S-mode: The sub-mesoscale ocean dynamics experiment. In *IGARSS 2020-2020 IEEE international geoscience and remote sensing symposium*, 3533–3536. IEEE. 10.1109/IGARSS39084.2020.9323112.

Fox-Kemper, B., Ferrari, R., & Hallberg, R. (2008). Parameterization of mixed layer eddies. part i: Theory and diagnosis. *Journal of Physical Oceanography*, *38*(6), 1145–1165. https://doi.org/10.1175/2007JPO3792.1.

Gill, A. E. (2016). *Atmosphere-ocean dynamics*, (1era ed.). Elsevier. (online: https://www1.muk.uni-hannover.de/hp-design2020/pdf/L%20I%2046%20Atmosphere-Ocean%20Dynamics,%20Gill.pdf.

Gula, J., Molemaker, M. J., & McWilliams, J. C. (2014). Submesoscale cold filaments in the gulf stream. *Journal of Physical Oceanography*, *44*(10), 2617–2643. https://doi.org/10.1175/JPO-D-14-0029.1.

Gula, J., Taylor, J., Shcherbina, A., & Mahadevan, A. (2022). Chapter 8 - submesoscale processes and mixing. In Meredith, M. & Naveira Garabato, A., editors, *Ocean Mixing*, (pp. 181–214). Elsevier. https://doi.org/10.1016/B978-0-12-821512-8.00015-3.

Haine, T. W. & Marshall, J. (1998). Gravitational, symmetric, and baroclinic instability of the ocean mixed layer. *Journal of Physical Oceanography*, *28*(4), 634–658. https://doi.org/10.1175/1520-0485(1998)028<0634:GSABIO>2.0.CO;2.

Hoskins, B. J. (1982). The mathematical theory of frontogenesis. *Annual review of fluid mechanics*, *14*(1), 131–151. https://www.annualreviews.org/doi/pdf/10.1146/annurev.fl.14.010182.001023.

Klein, P. & Lapeyre, G. (2009). The oceanic vertical pump induced by mesoscale and submesoscale turbulence. *Annual review of marine science*, *1*, 351–375. https://doi.org/10.1146/annurev.marine.010908.163704.

Klein, P., Lapeyre, G., Roullet, G., Le Gentil, S., & Sasaki, H. (2011). Ocean turbulence at meso and submesoscales: connection between surface and interior dynamics. *Geophysical & Astrophysical Fluid Dynamics*, *105*(4-5), 421–437. https://doi.org/10.1080/03091929.2010.532498.

Klein, P., Lapeyre, G., Siegelman, L., Qiu, B., Fu, L.-L., Torres, H., Su, Z., Menemenlis, D., & Le Gentil, S. (2019). Ocean-scale interactions from space. *Earth and Space Science*, *6*(5), 795–817. https://doi.org/10.1029/2018EA000492.

Large, W. G., Danabasoglu, G., Doney, S. C., & McWilliams, J. C. (1997). Sensitivity to surface forcing and boundary layer mixing in a global ocean model: Annual-mean climatology. *Journal of Physical Oceanography*, *27*(11), 2418–2447. https://doi.org/10.1175/1520-0485(1997)027<2418:STSFAB>2.0.CO;2.

Mahadevan, A. & Tandon, A. (2006). An analysis of mechanisms for submesoscale vertical motion at ocean fronts. *Ocean Modelling*, *14*(3-4), 241–256. https://doi.org/10.1016/j.ocemod.2006.05.006.

Mahadevan, A., Tandon, A., & Ferrari, R. (2010). Rapid changes in mixed layer stratification driven by submesoscale instabilities and winds. *Journal of Geophysical Research: Oceans*, *115*(C3). https://doi.org/10.1029/2008JC005203.

Marshall, J., Adcroft, A., Hill, C., Perelman, L., & Heisey, C. (1997). A finite-volume, incompressible navier stokes model for studies of the ocean on parallel computers. *Journal of Geophysical Research: Oceans*, *102*(C3), 5753–5766. https://doi.org/10.1029/96JC02775.

McWilliams, J. C. (2016). Submesoscale currents in the ocean. *Proceedings of the Royal Society A: Mathematical, Physical and Engineering Sciences*, *472*(2189), 20160117. https://doi.org/10.1098/rspa.2016.0117.

McWilliams, J. C. (2017). Submesoscale surface fronts and filaments: secondary circulation, buoyancy flux, and frontogenesis. *Journal of Fluid Mechanics*, *823*, 391–432. https://doi.org/10.1017/jfm.2017.294.

McWilliams, J. C., Gula, J., Molemaker, M. J., Renault, L., & Shchepetkin, A. F. (2015). Filament frontogenesis by boundary layer turbulence. *Journal of Physical Oceanography*, *45*(8), 1988–2005. https://doi.org/10.1175/JPO-D-14-0211.1.

Menemenlis, D., Campin, J.-M., Heimbach, P., Hill, C., Lee, T., Nguyen, A., Schodlok, M., & Zhang, H. (2008). Ecco2: High resolution global ocean and sea ice data synthesis. *Mercator Ocean Quarterly Newsletter*, *31*(October), 13–21. (online: https://www.mercator-ocean.eu/wp-content/uploads/2015/06/lettre_31_en.pdf#page=13.

Menemenlis, D., Hill, C., Henze, C. E., Wang, J., & Fenty, I. (2021). Boknis pre-swot level-4 hourly mitgcm llc4320 native grid 2km oceanographic dataset version 1.0. Dataset. Dataset accessed [2023-10-10] at https://doi.org/10.5067/PRESW-BOJ10.

Savage, A. C., Arbic, B. K., Alford, M. H., Ansong, J. K., Farrar, J. T., Menemenlis, D., O'Rourke, A. K., Richman, J. G., Shriver, J. F., Voet, G., et al. (2017). Spectral decomposition of internal gravity wave sea surface height in global models. *Journal of Geophysical Research: Oceans*, *122*(10), 7803–7821. https://doi.org/10.1002/2017JC013009.

Shcherbina, A. Y., D'Asaro, E. A., Lee, C. M., Klymak, J. M., Molemaker, M. J., & McWilliams, J. C. (2013). Statistics of vertical vorticity, divergence, and strain in a developed submesoscale turbulence field. *Geophysical Research Letters*, *40*(17), 4706–4711. https://doi.org/10.1002/grl.50919.

Siegelman, L. (2020). Energetic submesoscale dynamics in the ocean interior. *Journal of Physical Oceanography*, *50*(3), 727–749. https://doi.org/10.1175/JPO-D-19-0253.1.

Siegelman, L., Klein, P., Rivière, P., Thompson, A. F., Torres, H. S., Flexas, M., & Menemenlis, D. (2020). Enhanced upward heat transport at deep submesoscale ocean fronts. *Nature Geoscience*, *13*(1), 50–55. https://doi.org/10.1038/s41561-019-0489-1.

Siegelman, L., O'Toole, M., Flexas, M., Rivière, P., & Klein, P. (2019). Submesoscale ocean fronts act as biological hotspot for southern elephant seal. *Scientific reports*, *9*(1), 1–13. https://doi.org/10.1038/s41598-019-42117-w.

Stone, P. H. (1970). On non-geostrophic baroclinic stability: Part ii. *Journal of Atmospheric Sciences*, *27*(5), 721–726. https://doi.org/10.1175/1520-0469(1970)027<0721:ONGBSP>2.0.CO;2.

Su, Z., Torres, H., Klein, P., Thompson, A. F., Siegelman, L., Wang, J., Menemenlis, D., & Hill, C. (2020). High-frequency submesoscale motions enhance the upward vertical heat transport in the global ocean. *Journal of Geophysical Research: Oceans*, *125*(9), e2020JC016544. https://doi.org/10.1029/2020JC016544.

Su, Z., Wang, J., Klein, P., Thompson, A. F., & Menemenlis, D. (2018). Ocean submesoscales as a key component of the global heat budget. *Nature communications*, *9*(1), 1–8. https://doi.org/10.1038/s41467-018-02983-w.

Sullivan, P. P. & McWilliams, J. C. (2018). Frontogenesis and frontal arrest of a dense filament in the oceanic surface boundary layer. *Journal of Fluid Mechanics*, *837*, 341–380. https://doi.org/10.1017/jfm.2017.833.

Taylor, J. R. & Thompson, A. F. (2022). Submesoscale dynamics in the upper ocean. *Annual Review of Fluid Mechanics*, *55*. https://doi.org/10.1146/annurev-fluid-031422-095147.

Thomas, L. N. (2012). On the effects of frontogenetic strain on symmetric instability and inertia–gravity waves. *Journal of Fluid Mechanics*, *711*, 620–640. https://doi.org/10.1017/jfm.2012.416.

Thomas, L. N. (2017). On the modifications of near-inertial waves at fronts: implications for energy transfer across scales. *Ocean Dynamics*, *67*(10), 1335–1350. https://doi.org/10.1007/s10236-017-1088-6.

Thomas, L. N. & Lee, C. M. (2005). Intensification of ocean fronts by down-front winds. *Journal of Physical Oceanography*, *35*(6), 1086–1102. https://doi.org/10.1175/JPO2737.1.

Thomas, L. N., Tandon, A., & Mahadevan, A. (2008). Submesoscale processes and dynamics. *Ocean Modeling in an Eddying Regime*, *177*, 17–38. https://doi.org/10.1029/177GM04.

Thomas, L. N., Taylor, J. R., D'Asaro, E. A., Lee, C. M., Klymak, J. M., & Shcherbina, A. (2016). Symmetric instability, inertial oscillations, and turbulence at the gulf stream front. *Journal of Physical Oceanography*, *46*(1), 197–217. https://doi.org/10.1175/JPO-D-15-0008.1.

Thompson, A. F., Lazar, A., Buckingham, C., Garabato, A. C. N., Damerell, G. M., & Heywood, K. J. (2016). Open-ocean submesoscale motions: A full seasonal cycle of mixed layer instabilities from gliders. *Journal of Physical Oceanography*, *46*(4), 1285–1307. https://doi.org/10.1175/JPO-D-15-0170.1.

Torres, H. S., Klein, P., D'Asaro, E., Wang, J., Thompson, A. F., Siegelman, L., Menemenlis, D., Rodriguez, E., Wineteer, A., & Perkovic-Martin, D. (2022). Separating energetic internal gravity waves and small-scale frontal dynamics. *Geophysical Research Letters*, *49*(6), e2021GL096249. e2021GL096249 2021GL096249, https://doi.org/10.1029/2021GL096249.

Torres, H. S., Klein, P., Menemenlis, D., Qiu, B., Su, Z., Wang, J., Chen, S., & Fu, L.-L. (2018). Partitioning ocean motions into balanced motions and internal gravity waves: A modeling study in anticipation of future space missions. *Journal of Geophysical Research: Oceans*, *123*(11), 8084–8105. https://doi.org/10.1029/2018JC014438.

Vallis, G. K. (2017). *Atmospheric and oceanic fluid dynamics*, (2a ed.). Cambridge University Press. (online: https://doi.org/10.1017/9781107588417).

Wang, D.-P. (1993). Model of frontogenesis: Subduction and upwelling. *Journal of Marine Research*, *51*(3), 497–513. (online: https://elischolar.library.yale.edu/cgi/viewcontent.cgi?article=3069&context=journal_of_marine_research).

Yu, X., Naveira Garabato, A. C., Martin, A. P., Buckingham, C. E., Brannigan, L., & Su, Z. (2019). An annual cycle of submesoscale vertical flow and restratification in the upper ocean. *Journal of Physical Oceanography*, *49*(6), 1439–1461. https://doi.org/10.1175/JPO-D-18-0253.1.